IS-T 1677

Dynamical X-ray Diffraction from an Icosahedral Al-Pd-Mn Quasicrystal

by

Kycia, Stefan

PHD Thesis submitted to Iowa State University

Ames Laboratory, U.S. DOE

Iowa State University

Ames, Iowa 50011

Date Transmitted: April 23, 1996

PREPARED FOR THE U.S. DEPARTMENT OF ENERGY

UNDER CONTRACT NO. W-7405-Eng-82.

TABLE OF CONTENTS

ACKNOWLEDGEMENTS

I am indebted to many people for their aid, comfort and assistance during the course of my graduate studies at Iowa State University. First and foremost is my advisor, Alan Goldman who, in addition to teaching me how to be a scientist was a role model and a friend. I am thankful to him for giving me the opportunity to be his student and to enjoy many fine experiences at Iowa State University and abroad. I would like to thank Tom Lograsso and Drew Delaney, for without the high quality samples, the experimental work presented in this thesis would have been impossible. My education in electropolishing was a result of many hours spent under the guidance of Hal Salisbury. The inspiration for the correct means of electropolishing the Al-Pd-Mn surfaces came from Tim Ellis. Indeed, a great deal of my time was spent with the first rate metallurgy group of the Ames Laboratory, particularly with John Verhoeven, Bill McCallum, Matt Kramer, Kevin Dennis and Jeff Shield.

I would like to thank the people with who I had the great fortune to collaborate. Mark Sutton, Marc de Boissieu and Michel Boudard (I'm still keeping an eye out for those lost samples), David Black who taught me about x-ray topography, Ken Finkelstein who's immense creativity and knowledge made the Pendellösung measurements possible, Roberto Colella for his hospitality during my enlightening visit to Purdue University, Sam Werner for introducing me to the powerful technique of neutron diffraction and giving me the opportunity to make visits to the Missouri University Research Reactor with a moments notice.

I have also had the privilege of working (and playing) with fellow travelers in the Physics Department. For several years I shared quarters with Jonathan Lang,

Lun Xiong He, Carsten Detlefs, Simon Xiong, Sara Gunderson and, for all intents and purposes, Tea Cerkvenik, Gora Mohanty and Dimitris Kouzoudis.

This work was performed at Ames Laboratory under contract No. W-7405-ENG-82 with the Department of Energy. The United States government has assigned DOE report number IS-T-1677 to this thesis. The Cornell High Energy Synchrotron Source is supported by the National Science Foundation under grant No. DMR-87-19764. The National Synchrotron Light Source, Brookhaven National Laboratory, is supported by the USDOE under Contract No. DE-AC02-76CH00016. Beamline X23A3 is operated by the Ceramics Division, Materials Science and Engineering Laboratory, NIST.

I. INTRODUCTION TO QUASICRYSTALS

Introduction

In 1984 D. Shechtman and coworkers published electron diffraction patterns (Fig. 1.1) from rapidly quenched, metastable samples of Al_6Mn that exhibited relatively sharp diffraction peaks arranged in a pattern with icosahedral point group symmetry.[1] This marked the beginning of a new class of structures called "quasicrystals".

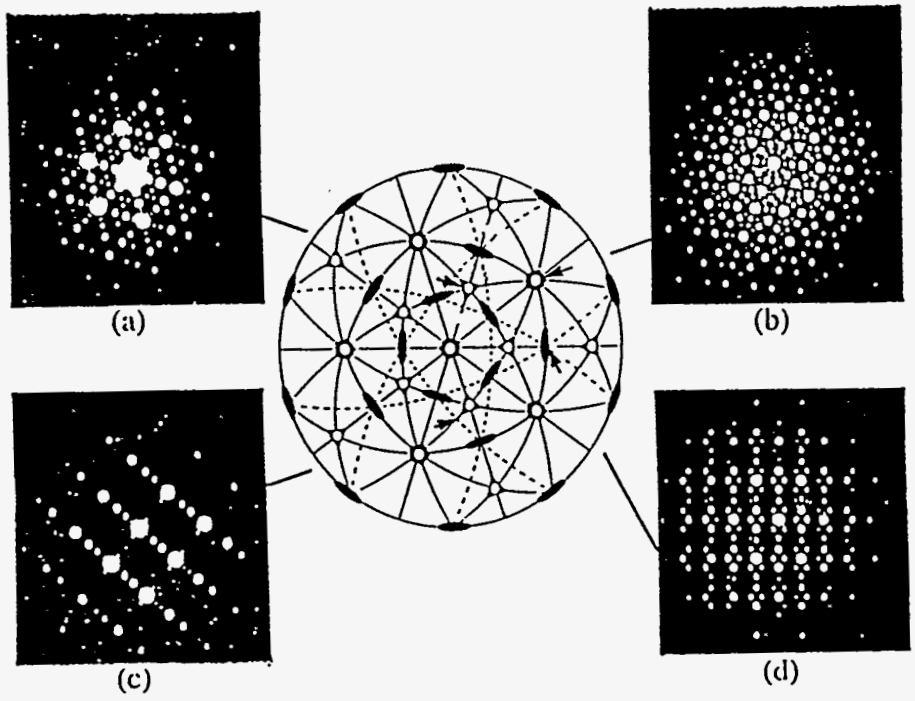

Fig. 1.1. TEM diffraction patterns from rapidly quenched Al-Mn taken perpendicular to (a) a 3-fold axis, (b) a 5-fold, (c) a pseudo-2-fold axis, and a 2-fold axis. The diffaction peaks are not arranged periodically. Arrows point to the corresponding poles of the stereographic projection for the icosahedral space group $m\bar{3}\bar{5}$, which is incompatible with periodic order.[2]

These structures presented a dilemma that caught the attention of researchers from a wide range of fields including physics, chemistry, metallurgy, and mathematics. The fundamental issue at hand, at least during the early investigations, was that diffraction patterns from quasicrystals defied a century old belief that sharp diffraction peaks signify the presence of long-range periodic order while it is well known that periodic structures cannot exhibit crystallographically forbidden rotational symmetries (e.g., fivefold, eightfold, tenfold and twelvefold rotation axes).[3] It was soon realized that our notion of the equality of order and periodicity was a rather restrictive view of the full range of possibilities for ordered structures. While sharp diffraction spots are, indeed, the signature of long-range positional order, the positional order in the icosahedral phase alloys is *aperiodic* rather than periodic. Soon after the discovery of the original Al-Mn quasicrystals, other Al-based alloys such as Al-Li-Cu and Al-TM-Si (TM=Transition Metal), as well as Ga-Mg-Zn and Ti-Mn-Si were discovered to exhibit stable or metastable icosahedral phases.[4-6] The Al-Mn quasicrystal, then, was not an isolated curiousity, but represented the first example of a new class of "ordered" structures.

The emergence of any new field of study is generally accompanied by a new body of terms unique to that field. In the sections that follow, my principal aim is to introduce and explain the phenomenon of diffraction from icosahedral quasicrystals along with the nomenclature used to describe the possible structures that the diffraction patterns reveal.

Quasicrystallography

The first problem with which we are faced is a proper description of the diffraction pattern of icosahedral alloys and their structures. Inasmuch as the

diffraction pattern is a representation of the reciprocal space of the system, the direct space, or real space, structure of these alloys follows from how we describe the reciprocal "lattice." Quasicrystals are fundamentally incommensurate systems which, for some purposes, are best described in terms of a reciprocal lattice in an N-dimensional space, where N > 3. This abstraction is not unique to quasicrystals themselves. Indeed, the use of higher dimensional spaces for the description of incommensurate systems had proved useful long before the discovery of quasicrystals. Higher dimensional spaces were used for descriptions of incommensurate crystals by DeWolf in 1972[7] and Janner and Janssen in 1977.[8] Studies of short range icosahedral order in metallic glasses and supercooled liquids led Sadoc and Mosseri in 1982,[9] and Nelson in 1983,[10] to use a four dimensional space for their description of atomic correlations. For quasicrystals, the development of a six-dimensional description of the diffaction pattern and real space structure follows from the indexing system used to characterize the diffraction pattern as described below. It also provides us with a relatively straightforward manner of describing various structural models for the icosahedral phase, the relationship between the models, as well as the types of structural disorder characteristic of quasicrystalline alloys.[11-17]

Periodic Crystallography

The diffraction pattern from three-dimensional periodic crystals can be indexed in terms of a set of three integer indices (h,k,l) and three corresponding basis vectors $\{a^*\hat{x}, b^*\hat{y}, c^*\hat{z}\}$ where a*, b* and c* are reciprocal to the lattice constants of the periodic structure. This implies that a periodic reciprocal space lattice can be constructed so that the reciprocal lattice points are defined by, $\vec{Q} = (a^*h\hat{x} + b^*k\hat{y} + c^*l\hat{z})$.

For the case of x-ray diffraction, the scattering crystal can be represented as a charge distribution $\rho(\vec{r})$ that can be written as a Fourier series related to the reciprocal lattice so that

$$\rho(\vec{r}) = \sum_{\vec{Q}} \rho_{\vec{Q}} \exp\left(i\vec{Q}\cdot\vec{r}\right), \tag{1-1}$$

where the $\rho_{\vec{Q}}$ are complex coefficients associated with each reciprocal lattice point. In a scattering measurement, the structure factors, F_{HKL}, which largely determine the intensity of the diffracted beam, are given by $\rho_{\vec{Q}} V_c$ (V_c = Volume of the unit cell). Unfortunately, the reflections give no information about the phase of the coefficients. The fundamental process for solving crystal structures involves determining the coefficients $\rho_{\vec{Q}}$ and, in light of the "phase problem," comparing the observed $\rho_{\vec{Q}}$ with those calculated from some model structures. Various techniques have been developed, such as the Patterson and Direct methods, for partial phase analysis and experimental techniques for measuring the phase relation between pairs of Fourier coefficients have been developed based on multiple scattering techniques.[18a]

Quasicrystallography

In the case of icosahedral quasicrystals, (for example the electron diffraction patterns of Fig. 1.1 and the powder x-ray diffraction pattern of Fig. 1.2) it is not possible to index the set of reflections using three integer indices. Rather, one finds that the reflections must be indexed using six integer indices for basis vectors along three orthogonal axes:

$$\vec{Q} = C^*\left[(h+\tau h')\hat{x} + (k+\tau k')\hat{y} + (l+\tau l')\hat{z}\right], \tag{1-2}$$

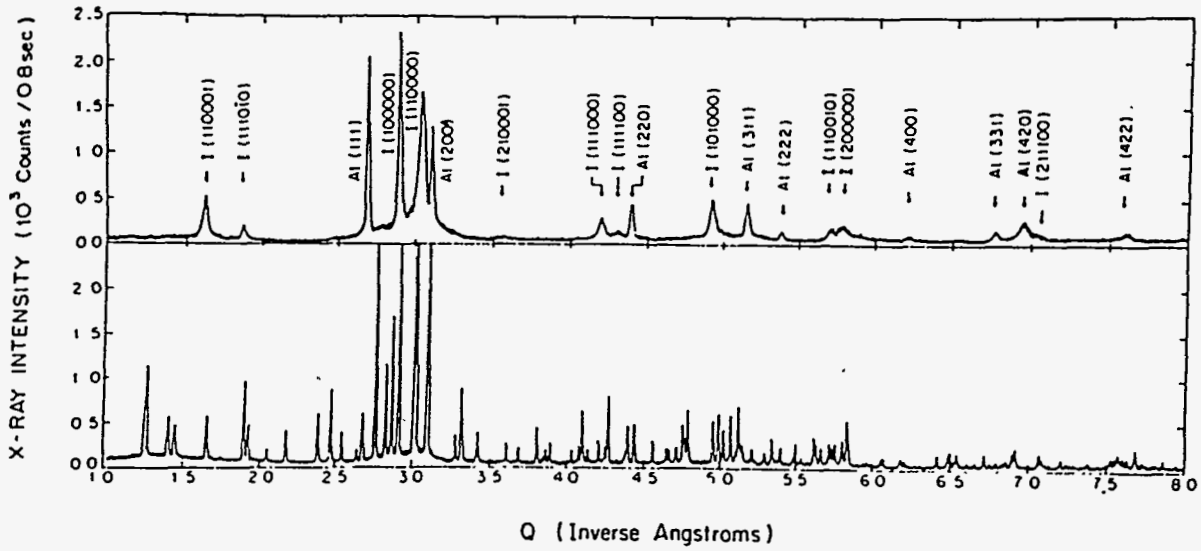

Fig. 1.2. Top: High-resolution x-ray diffraction pattern of quenched Al-Mn powder. The sample consisted of FCC Al and icosahedral Al-Mn. Peaks are labeled Al or I respectively and indexed appropriately. Broad diffraction peaks are evidence of disorder in the icosahedral phase. Below: Diffraction pattern of annealed Al-Mn powder reveals orthorhombic Al_6Mn.[18b]

Here, τ is the golden mean $\left(\tau=\left(\sqrt{5}+1\right)/2\right)$ which arises from the geometry of icosahedra and pentagons and $\{h,h',k,k',l,l'\}$ is the set of six integer indices. Since τ is an irrational number, the set of lattice points in reciprocal space do not form a periodic sequence. While equation 1-2 provides a means of indexing the lattice that is useful for scattering work, it does not exploit or elucidate the symmetry of the reciprocal lattice. For quasicrystals with icosahedral point symmetry one can choose the basis vectors as the set of six independent vectors drawn from the center to the vertices of an icosahedron (Fig 1.3). The basis vectors can then be written:

$$
\left.
\begin{aligned}
\vec{e}^{\,*}_{1\parallel} &= \left(\frac{a_0^*}{\sqrt{1+\tau^2}}\right)(1,\tau,0) \\
\vec{e}^{\,*}_{2\parallel} &= \left(\frac{a_0^*}{\sqrt{1+\tau^2}}\right)(-1,\tau,0) \\
\vec{e}^{\,*}_{3\parallel} &= \left(\frac{a_0^*}{\sqrt{1+\tau^2}}\right)(0,1,\tau) \\
\vec{e}^{\,*}_{4\parallel} &= \left(\frac{a_0^*}{\sqrt{1+\tau^2}}\right)(\tau,0,1) \\
\vec{e}^{\,*}_{5\parallel} &= \left(\frac{a_0^*}{\sqrt{1+\tau^2}}\right)(\tau,0,-1) \\
\vec{e}^{\,*}_{6\parallel} &= \left(\frac{a_0^*}{\sqrt{1+\tau^2}}\right)(0,1,-\tau)
\end{aligned}
\right\} \qquad (1\text{-}3)
$$

and the reciprocal lattice vector can be defined as

$$\vec{Q} = n_1\vec{e}^{\,*}_{1\parallel} + n_2\vec{e}^{\,*}_{2\parallel} + n_3\vec{e}^{\,*}_{3\parallel} + n_4\vec{e}^{\,*}_{4\parallel} + n_5\vec{e}^{\,*}_{5\parallel} + n_6\vec{e}^{\,*}_{6\parallel} \qquad (1\text{-}4)$$

where $\{n_1, n_2, n_3, n_4, n_5, n_6\}$ is the set of integer indices and the reason for the notation, $\vec{e}^{\,*}_{1\parallel}$, will soon be made apparent. Defining the basis vectors in this manner, the connection between measurements made in three dimensions and the higher dimensional description of the reciprocal lattice becomes apparent since equation 1-4 also describes a periodic function of *six* variables.

The six dimensional reciprocal space can be described by assuming a set of six-orthogonal basis vectors $\vec{e}_i^{\,*}$ to form a hypercubic lattice defined by

$$\vec{Q}^{(6)} = n_1\vec{e}_1^{\,*} + n_2\vec{e}_2^{\,*} + n_3\vec{e}_3^{\,*} + n_4\vec{e}_4^{\,*} + n_5\vec{e}_5^{\,*} + n_6\vec{e}_6^{\,*}. \qquad (1\text{-}5)$$

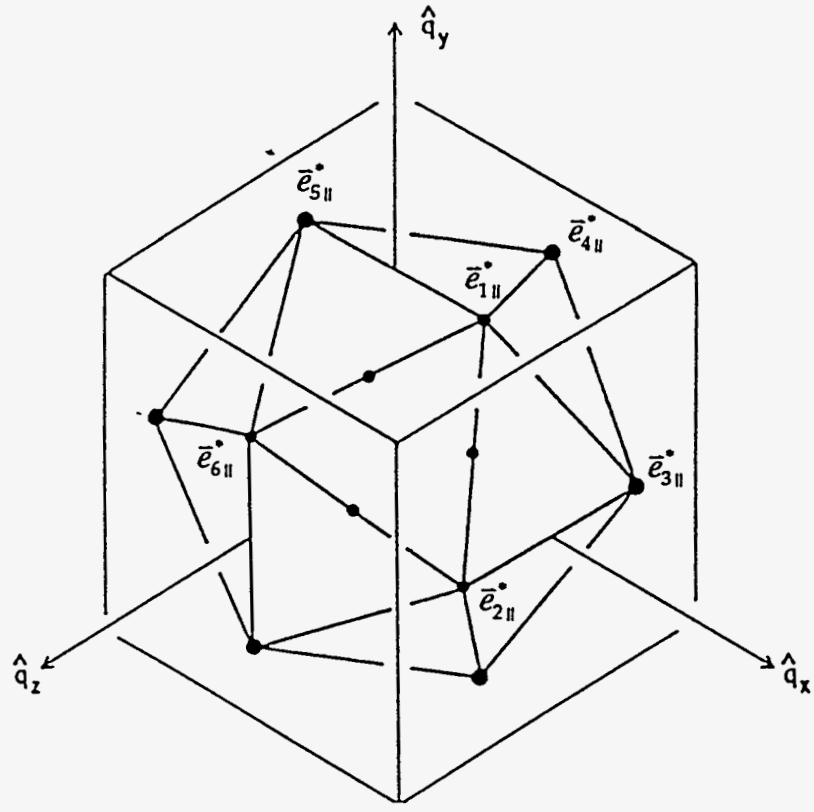

Fig. 1.3. Reciprocal lattice vectors are drawn from the center to the vertices of an icosahedron and are defined as in equation 1-3.

The advantage of this construction is that we are now dealing with a *periodic* lattice, albeit in six dimensions. Icosahedral quasicrystals, then, are incommensurate structures in three dimensions, but periodic in six-dimensions. An important point here, which has relevence to later discussions of dynamical scattering in quasicrystals, is that the the charge density can still be written as a Fourier series

$$\rho(\vec{r}) = \sum_{\vec{Q}} \rho_{\vec{Q}} \exp\left(i\vec{Q}\cdot\vec{r}\right). \tag{1-6}$$

where $\rho_{\vec{Q}}$ are complex coefficients.

The problem of solving the structure of a quasicrystal involves relating this charge distribution to the reciprocal lattice points and producing the appropriate complex coefficients $\rho_{\vec{Q}}$ from the data. Just as in the case for periodic crystals, the absence of phase information for the coefficients is the problem. An additional, fundamental difficulty in solving the structure is that the absence of periodicity also implies the absence of any fundamental structural building block, or unit cell in three dimensions. This means that, in principle, the full description of the structure of a quasicrystal in three dimensions requires the specification of an infinite set of atomic positions.

As was true for the reciprocal space construction above, the direct space structure of icosahedral quasicrystals may be described, abstractly, in terms of a six-dimensional hypercubic lattice. Since periodicity is recovered in this higher dimensional space, it is only necessary to solve the atomic decoration of a single 6-D unit cell as opposed to the entire 3-D quasicrystal. However, one consequence of this construction is that now, rather than having a unit cell decorated withpoint particles, the particles are represented by three dimensional atomic surfaces. The solution of the structure in six-dimensions requires only the specification of a finite set of atomic surfaces. In order to illustrate this idea and demonstrate the connection between the higher dimensional description and the lower dimensional physical manifestation of the structure I consider, below, a set of simplified one dimensional examples of the "cut and projection" technique.

2-D to 1-D Projection

It is possible to produce one-dimensional periodic and aperiodic structures by means of what is called a "2-D to 1-D cut and projection technique."

One first constructs a two-dimensional square lattice of points with basis vectors $\hat{e}_1 = \hat{x}$ and $\hat{e}_2 = \hat{y}$. A line $R_{\parallel}$ is drawn through the origin in space making an angle θ with the x axis as shown in Fig. 1.4. This line defines two orthogonal unit vectors, $\hat{r}_{\parallel}$ is parallel to the line and $\hat{r}_{\perp}$ is perpendicular to the line. The position of any point in space can be described by the vectors $\vec{r} = r_{\parallel}\hat{r}_{\parallel} + r_{\perp}\hat{r}_{\perp}$, where $r_{\parallel}$ is called the parallel or physical space component and $r_{\perp}$ is the perpendicular space component. At each lattice point of the 2-D space, we place an *atomic surface*.. For the atomic surfaces to represent point like atoms in the 1-D physical space, it is possible to represent the atomic surfaces as lines segments (perpendicular to $\hat{r}_{\parallel}$) as shown in Fig. 1.4a. The intersection of an atomic surface with the $R_{\parallel}$ axis determines the position of that atom in the physical space. The physical space, in this case, is a one dimension cut through a two dimensional periodic lattice.

It is useful here to illustrate the process with two examples: the Fibonacci sequence of atomic displacements that results from a specific irrational cut through the 2-D lattice, and a periodic approximant to the Fibonacci sequence which results from a rational cut through the 2-D lattice. The significance of these structures will be discussed in the next section.

It is observed that the line segment $R_{\parallel}$ contains points separated by two lengths of increments, long and short. The slope of the line $R_{\parallel}$ in the two dimensional space determines the lengths of the segments L and S as well as

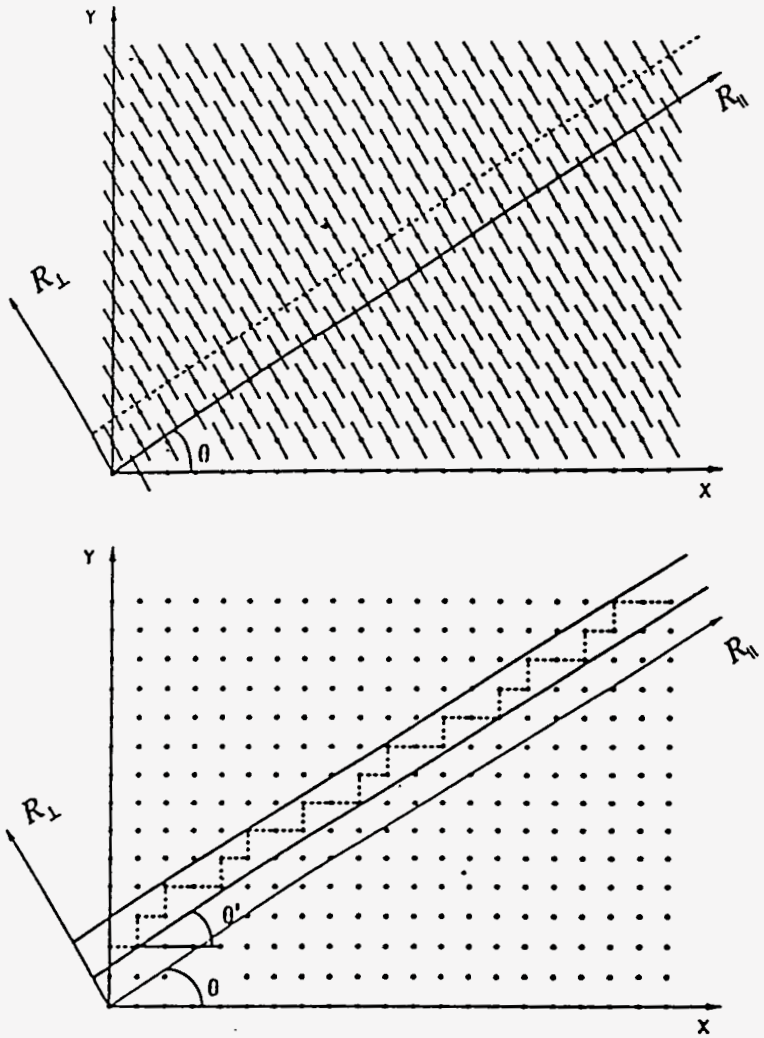

Fig. 1.4. Contruction of a Fibonacci sequence by the cut and projection method. (a) The line segments represent atomic surfaces at sites of a two dimensional square lattice. The intersections of the atomic surfaces with the one dimensional physical space $R_{\parallel}$ place atoms in a Fibonacci sequence. (b) An alternative scheme constructs a Fibonacci sequence of atoms in one dimension. The heavy lines represent the boundaries of an acceptance domain. All sites in the 2-D lattice within the acceptance domain are projected onto $R_{\parallel}$. The horizontal and vertical dashed lines projected onto L and S segments along the $R_{\parallel}$ axis form a Fibonacci sequence.

whether if the sequence is periodic or quasiperiodic. If $\cot(\theta)$ is the irrational number τ, then the sequence will be defined by a Fibonacci sequence of long (L) and short (S) interatomic spacings. If $\cot(\theta)$ is a rational number so that $\cot(\theta) = p/q$ where p and q are integers, then the sequence of points will be periodic. For example, if $\cot(\theta) = 1/1$ the sequence of interatomic separations will be long L segments followed by short S segments. This is the 1/1 (or τ_2) approximant of the Fibonacci sequence. An entire series of periodic approximant structures to the Fibonacci sequence can be produced for angles $\theta = \cot^{-1}(p/q)$ where p and q are succesive integers in the Fibonacci sequence (e.g. 3/2, 5/3, 8/5 etc..). As the slope $\cot(\theta)$ approaches τ, the unit cell becomes larger and the structure better approximates the Fibonacci sequence.

Diffraction from the 1-D Aperiodic Sequence

The diffraction pattern from the resulting structure in our physical space can again be determined by projection from a 2-D reciprocal space. A 2-D periodic structure factor can be calculated as the Fourier Transform of the 2-D periodic square lattice with an atomic surface at each site. This produces a periodic square lattice as shown in Fig. 1.5. The 2-D reciprocal lattice axes are Q_x and Q_y, the physical reciprocal space axis $Q^{\parallel}$, and the perpendicular reciprocal space axis $Q^{\perp}$ are defined in Fig. 1.5. The structure factor along the physical reciprocal axis $Q^{\parallel}$ corresponds to the structure factor that would be calculated for the 1-D sequence of atoms in $R_{\parallel}$.

An interesting point to note in the Fourier transform of Fig. 1.5 is that the intensity of diffraction depends upon the the perpendicular distance of the reciprocal lattice point from the $Q^{\parallel}$ axis or, equivalently, the value of $Q^{\perp}$ for the

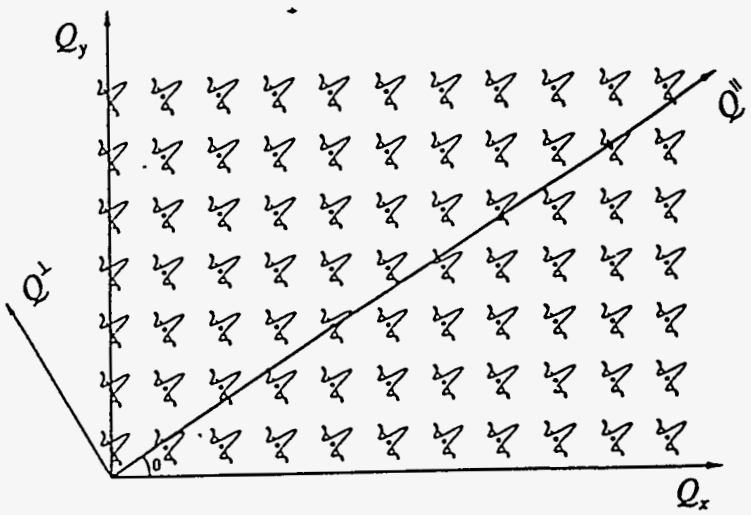

Fig. 1.5. An expanded view of the Fourier transform of the Fibonacci sequence is obtained by placing the Fourier transform of the atomic surfaces in Fig. 1.4a or the acceptance domain of Fig. 1.4b at the sites of a two-dimensional lattice reciprocal to those of Fig. 1.4a and Fig. 1.4b. The intensity of a diffraction peak is proportional to the square of the amplitudes of the transforms where they intersects the $Q^{\parallel}$ axis.

reciprocal lattice point. This is one aspect of diffraction from quasicrystals which does not have an analog in diffraction from three-dimensional periodic structures. It is for this reason that while the reciprocal space of a quasicrystal is densely filled with reciprocal lattice points, only a few contribute significantly to the scattering. In general, two reciprocal lattice points along the same direction that have similar values of $Q^{\parallel}$, have very different values of $Q^{\perp}$.

Two types of icosahedral quasilattices have been observed. For simple icosahedral (SI) structures, such as found in Al-Mn[19] and Al-Li-Cu,[20] the indices are unrestricted (each n_i may take on any integer value), in analogy with simple cubic crystals. For face-centered icosahedral (FCI) structures, such as Al-Cu-Fe, AlCu-Ru,[21] and Al-Pd-Mn,[22] the indices must have the same parity (n_i all even or all odd), in analogy with the face-centered-cubic crystals. Interestingly, there are striking differences in the stability and degree of disorder between these two classes of alloys that appear to be related to an enhanced degree of chemical order in the FCI alloys. Structural differences between FCI and SI alloys have been the subject of intense scrutiny over the past five years.

One-Dimensional Structural Models

It is instructive to examine the calculated diffraction patterns for a variety of one dimensional collections of identical scatterers in order to appreciate how different classes of structural models for quasicrystals produce diffraction patterns and are related to each other. In this section I will focus on three one-dimensional models that have proved to be relevent for the present understanding of quasicrystalline order.

Fibonacci Chain

It is possible to construct a one dimensional aperiodic yet positionally ordered sequence of points by following a Fibonacci sequence. The chain is composed of a series of two building blocks of different length (a long L, and a short S). The ratio of lengths L/S is equal to an irrational number $\tau = (1+\sqrt{5})/2$. The structure can be produced by the "cut and projection" technique described in the previous section or, alternatively, by adhering to the following set of the growth rules:

1: Start with any given segment, L or S , in the first generation

2: In the next generation, all long segments are replaced by a long and short $L \rightarrow LS$, and all short segments are replaced by long segments $S \rightarrow L$.

Several iterations of the inflation process are demonstrate in Fig. 1.6. The calculated diffraction pattern for a Fibonacci Chain is shown in Fig. 1.7, and consists of a set of sharp peaks with a width limited only by the finite size of the sample. Interestingly, examples of 1-D Fibonacci ordered structures have been discovered in rapidly quenched alloys of Al-Ni-Si, Al-Cu-Mn, and Al-Cu-Co.[23] These structures display periodic order in two directions and aperiodic order in a third orthogonal direction.

Periodic Fibonacci Approximant

As described in the previous section, it is also possible to construct a periodic chain of scatterers that produces a calculated diffraction pattern approximating that for the Fibonacci chain. This *periodic Fibonacci approximant*, grows like a Fibonacci chain for a finite number of iterations and then repeats. The length of the repeat

Iteration	Fibonacci Chain
1	LS
2	LSL
3	LSLLS
4	LSLLSLSL
5	LSLLSLSLLSLLS
6	LSLLSLSLLSLLSLSLLS
7	LSLLSLSLLSLLSLSLLSLSLLSLSLLSLLS

Fig.1.6 Generation of a Fibonacci sequence by the rules L → LS and S → L is an example of long range aperiodic order in one dimension.

sequence determines how closely the diffraction pattern from the periodic chain approximates that of the Fibonacci Chain. The repeat sequence will consist of p long segments, q short segments, and a total of $n = p + q$ segments (Fig. 1.8), so it is possible to label the chain by p/q or equivalently τ_n. As the repeat sequence becomes infinitely long the ratio p/q approaches τ. Examples of calculated diffraction patterns for several periodic approximants are also presented in Fig. 1.7. What seems clear from these diffraction patterns is that as p/q approaches τ, it becomes progressively more difficult to distinguish between a high-order periodic approximant and the aperiodic sequence itself. A series of alloys of Al-Ni-Cu (which are layered structures) have been discovered to approximate the Fibonacci sequence and to correspond to the approximants labeled as τ_2, τ_3, τ_5, τ_8, τ_{13}, τ_{21}, and τ_{34}.[24]

Hendricks-Teller Model

The two models described above are ordered structures. Disorder can be introduced into either model by a process analagous to stacking faults in crystals.

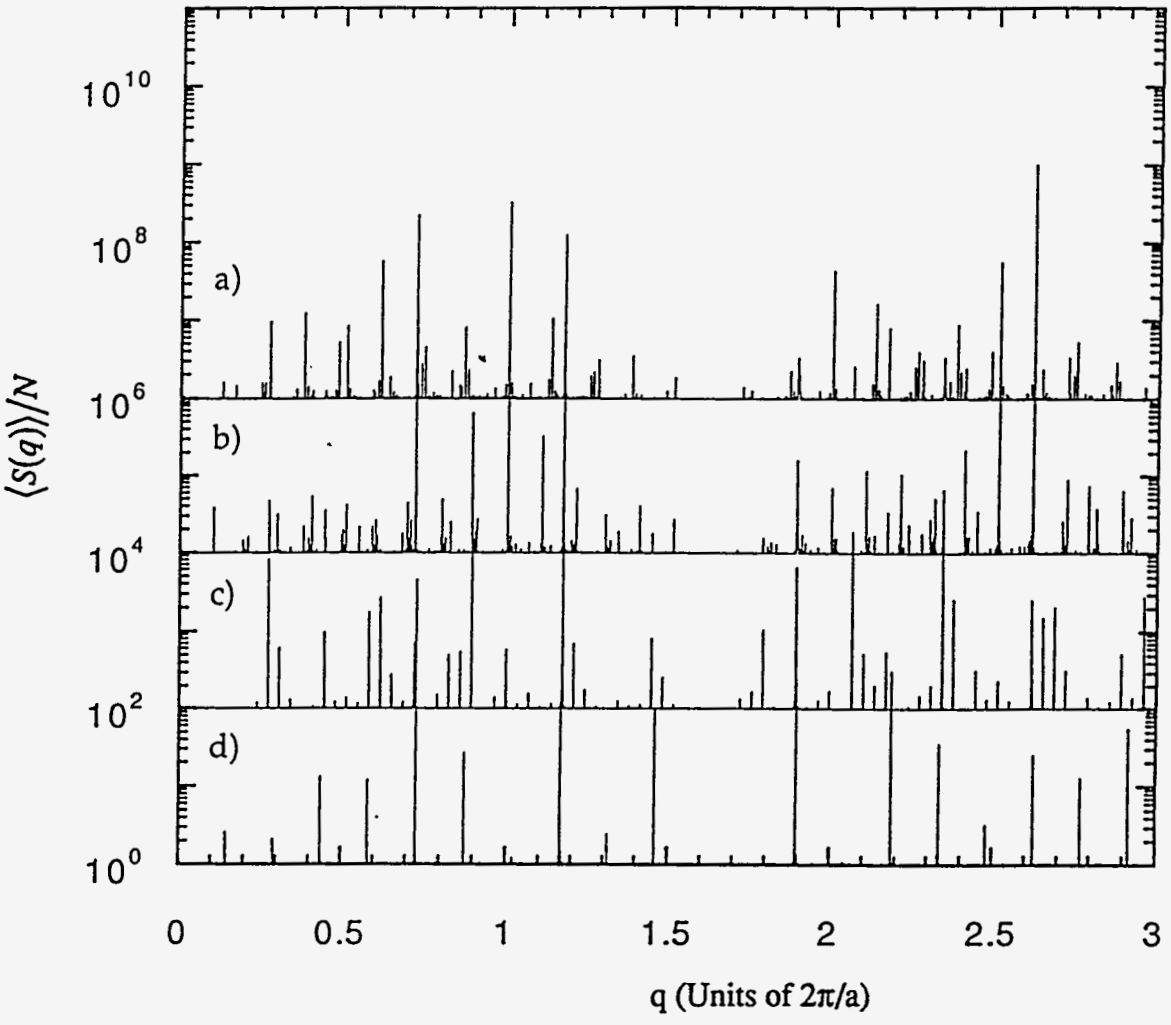

Fig. 1.7. Calculated structure factors of computer generated one dimensional sequences of intervals of length a and τa. Shown is: a) the Fibonacci sequence, b) the τ_{89} approximant, c) the τ_{21} approximant, and d) the τ_5 approximant. It can be seen that as the unit cell of the approximant increases, not only does the reciprocal space become more densely filled with peaks, but the diffraction pattern of the approximant better resembles the pattern of the Fibonacci sequence. The infinitely long Fibonacci sequence produces a reciprocal space that is filled with an infinite number of sharp peaks, although the number of strong reflections remains limited.

τ_n	repeat unit sequence
2	LS
3	LSL
5	LSLLS
8	LSLLSLSL
13	LSLLSLSLLSLLS
21	LSLLSLSLLSLLSLSLLSLSL
34	LSLLSLSLLSLLSLSLLSLSLLSLLSLSLLSLLS

Fig. 1.8. Repeat sequences (composed of long and short segments) for periodic structures that approximate the Fibonacci sequence.

That is, one can imagine the random substitution of L for S and S for L in the Fibonacci sequence. The extreme limit of this case has come to be termed the Hendricks-Teller model[25] and has proved to be useful for the description of disordered layered structures.[26,27] In the present context, the 1-D chain consists of a random sequence of long, L, and short, S, segments An example of a calculated diffraction pattern from a HT chain is presented in Fig. 1.9. Perhaps the most interesting feature of the diffraction pattern is that it consists of both broad and sharp diffraction peaks. Furthermore, the weaker peaks are also the broader peaks. We will come back to this point below in the context of disorder in quasicrystals.

Since the relationship between the ideal 1-D Fibonacci sequence and its periodic approximants has been illustrated using the "cut and projection" procedure, it is useful to briefly describe the higher dimensional analog of the HT model. Referring back to Figure 1.4, all that is really necessary to generate a disordered sequence of L and S segments along the physical space axis is to assume a random set of shifts of the atomic surfaces along the direction perpendicular to the physical

space axis. Alternatively, in the bottom part of Fig. 1.4, one can allow the acceptance strip to meander. Both have the net effect of exchanging L(S) segments for S(L) segments in a random fashion leading to the HT chain.

Three-Dimensional Structural Models

The Periodic Models

One proposed set of structural models for describing the observed electron diffraction patterns is actually based on periodic structures.[28-31] These models

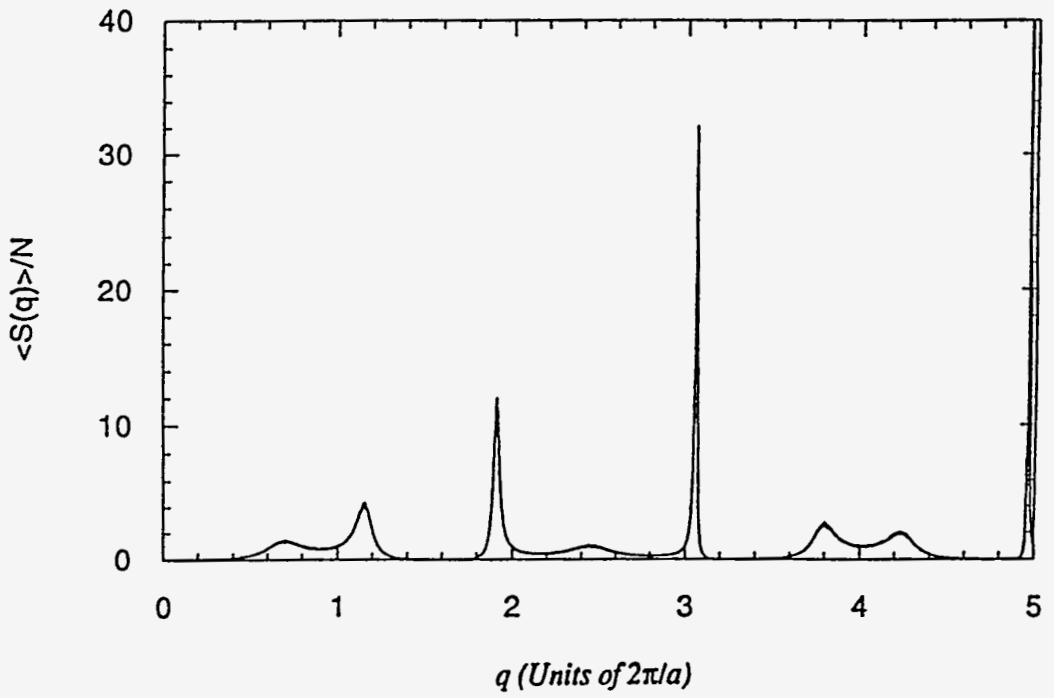

Fig. 1.9. Calculated ensemble average structure factor of a computer generated random sequence of intervals (a Hendricks-Teller Model) of length a and τa reveals both sharp and broad peak widths.

consist of periodic crystals with large unit cells that are decorated with atoms in such a way as to produce diffraction patterns that approximate icosahedral symmetry (the diffraction peaks are shifted slightly from those of an icosahedral structure). If the unit cell is large enough, these small shifts can become unresolvable. As an explanation for the observed diffraction patterns from alloys such as Al-Pd-Mn, these models fail because the unit cell that would be appropriate requires a decoration of more than 100,000 atoms. The decoration of such a large unit cell presents a problem in itself. The question can be asked, "after packing 100,000 atoms together aperiodically, why does the structure repeat as opposed to continuing the aperiodic growth?"

Although the periodic models are not an appropriate description for quasicrystals, alloys of compositions similar to known quasicrystals have been found to grow as periodic approximants of quasicrystals. The structural determination of the unit cell decoration revealed atoms forming icosahedrally symmetric clusters (Fig. 1.10).[32-34] It is believed that these clusters are building blocks of the quasicrystalline phases for alloys of slightly different stochiometry. In addition, the observation of the quasicrystalline phase growing coherently with the crystalline phase in the same sample is frequently observed.[35,36] The study of quasicrystal-related periodic structures has helped in our understanding of local atomic order, stability and physical properties of quasicrystals.[2]

The Quasiperiodic Model

In 1974 R. Penrose discovered an aperiodic, highly ordered, pentagonal tiling of the plane shown in Fig. 1.11.[38,39] This structure was later shown to produce an optical diffraction pattern that revealed sharp peaks.[40] The Penrose tiling structure

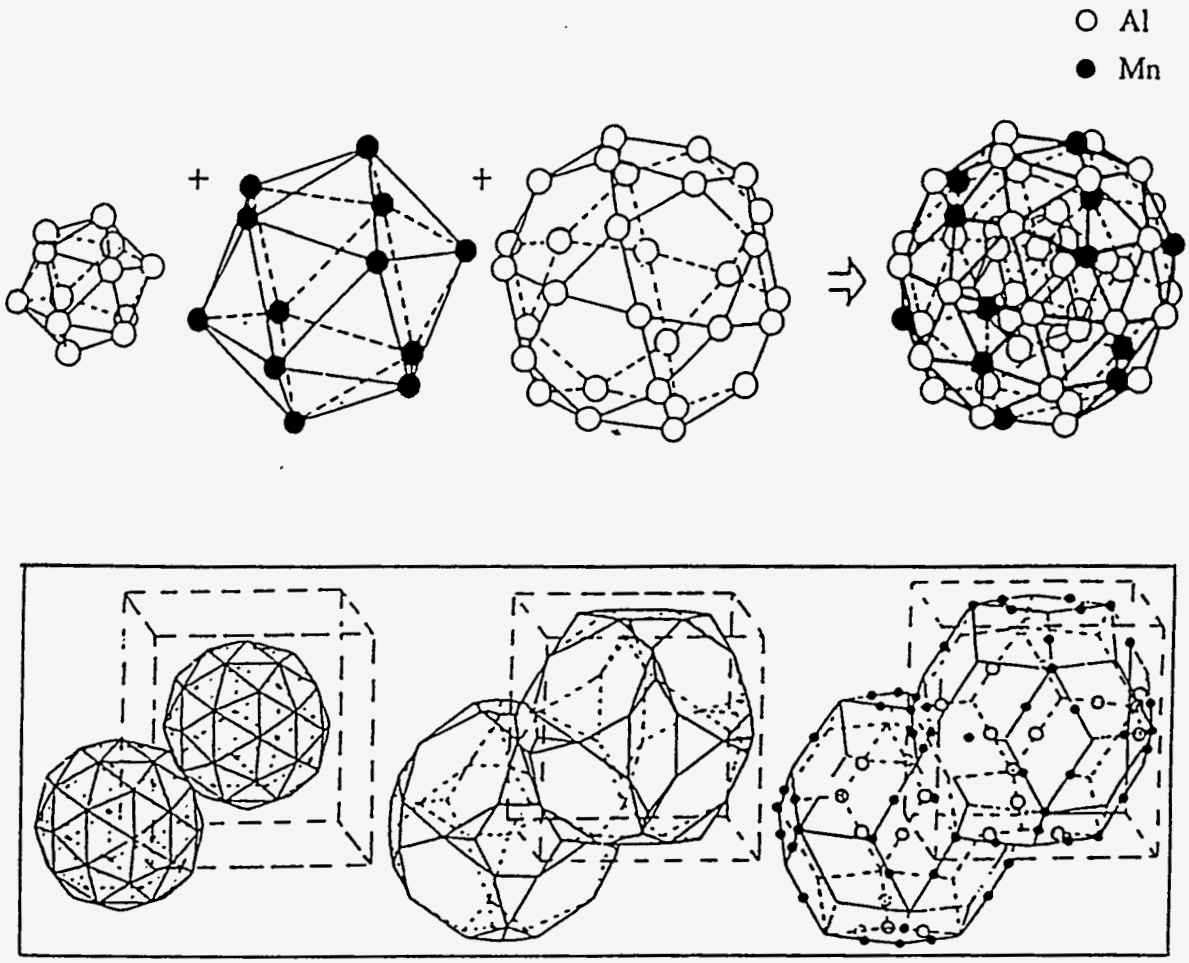

Fig. 1.10. Periodic crystals of α(AlMnSi) have been found to approximate SI Al-Mn quasicrystals. A structure determination of α(AlMnSi) has found that the unit cell is decorated by an icosahedrally symmetric cluster called the Mackay icosahedron which is an aggregate of 54 atoms of Al and Mn. Top: Shown is a depiction of a Mackay icosahedron with the Al atoms as empty circles and Mn atoms as filled circles. Bottom: the icosahedral clusters are positioned at the corners and centers of the unit cell as shown. Additional atoms of Al and Si surround the Mackay icosahedra.[37]

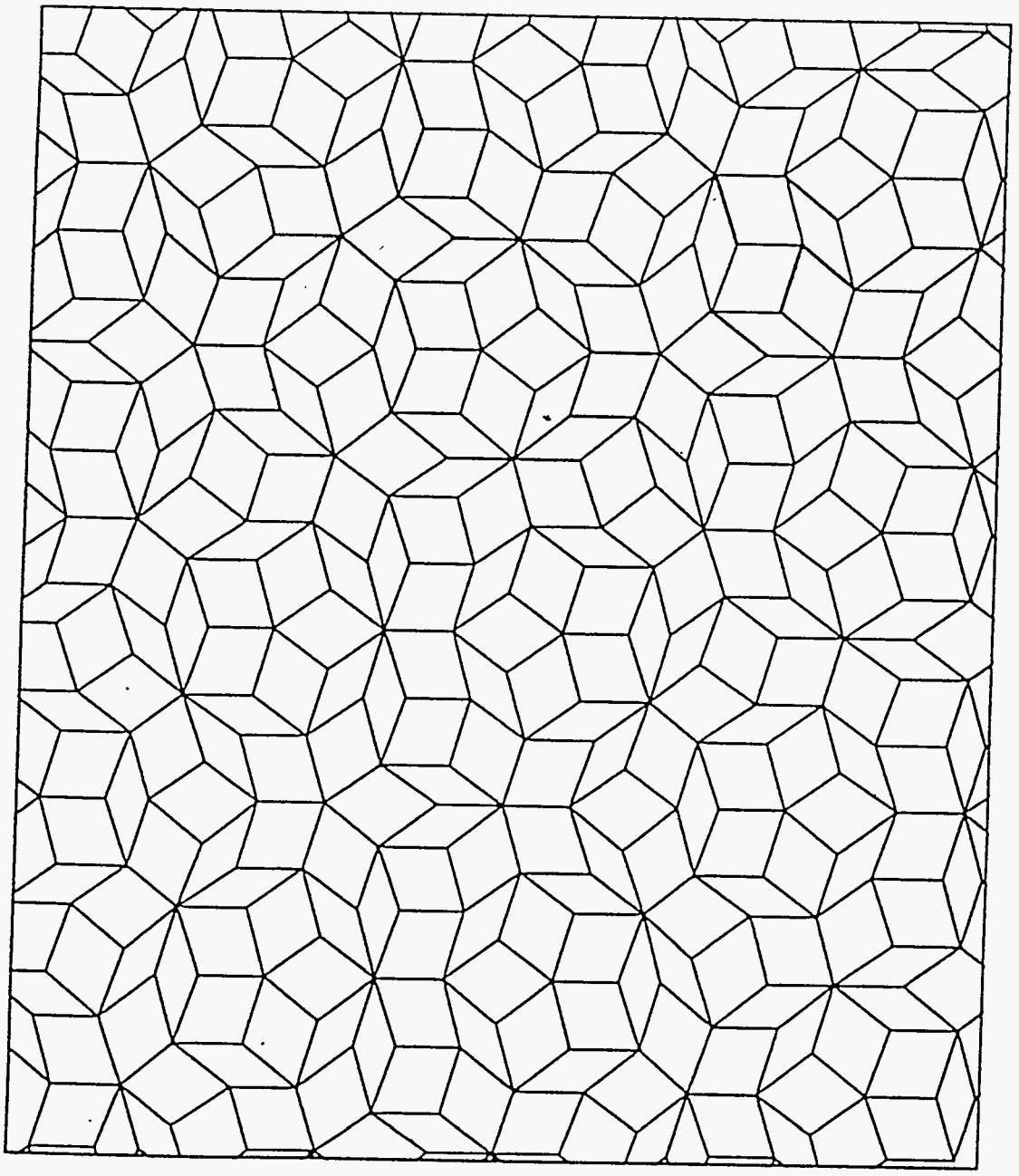

Fig. 1.11. Penrose tiling is an example of a two dimensional quasiperiodic ordering of two types of tiles, (in this case "thin" and "fat" rhombuses).[39] Diffraction patterns from this structure would produce the crystalographically forbidden 10-fold symmetry.

was adapted to an icosahedral aperiodic tiling of space by R. Ammann.[41] These models avoid the restriction imposed on periodic crystals that exclude five fold symmetry by filling space with an arrangement of more than one type of unit cell in a highly ordered aperiodic manner. P. Steinhardt and D. Levine proposed that quasiperiodic structure models may be appropriate for the discription of the Al-Mn alloys, computed the diffraction pattern of an ideal quasicrystal, and showed that the electron diffraction patterns obtained by Shechtman et al. were closely related to that of an icosahedral quasicrystal.[42] The quasicrystal models have been found to be most successful in describing the diffraction patterns of the highly perfect Face Centered Icosahedral quasicrystals (Al-Cu-Fe, Al-Cu-Ru and Al-Pd-Mn). Although the perfect quasicrystal model presents an explanation of aperiodic long range order as a means of producing sharp diffraction peaks and diffraction patterns exhibiting icosahedral symmetry, it does not explain how the restrictions on the arrangement of the unit cells relate to the growth process involved in the actual quasicrystal formation.

The Icosahedral Glass Model

Determined to produce a model that explains the experimentally observed icosahedral symmetry and the broadened diffraction peaks, P. Stephens and A. Goldman (1986) proposed the "Icosahedral Glass" model.[43-44] The model is in a way a three dimensional analog of the Hendricks-Teller model (Fig. 1.12). The model, as defined in Ref. 37, "consists of a system composed of clusters of atoms such that: (1) each individual cluster has icosahedral symmetry, (2) the clusters are joined so that they all have the same orientation, (3) there is some degree of

randomness in the connection of the clusters, and (4) the accretion of the clusters is governed by purely local geometric rules."

Calculated diffraction patterns from computer calculated icosahedral glass models proved to agree well with x-ray diffraction data for Simple Icosahedral alloys. Variations of the original model have included more detailed local growth rules and have produced better reproductions of the diffraction data. The icosahedral glass model's dependence only on short range correlations for the growth process seems to be an intuitively reasonable explanation for the mechanism for SI quasicrystal growth. The model, however, is inappropriate as a description of the structure of FCI alloys such as Al-Cu-Fe, Al-Cu-Ru, and Al-Pd-Mn, since these alloys produce resolution limited diffraction peaks. Therefore, the understanding of how nature grows FCI structures with correlation lengths as large as 1 μm has not yet been realized.

Quasicrystals and Disorder

Although the diffraction peaks from the earliest icosahedral alloys, such as Al-Mn, were reasonably sharp, they were not perfectly sharp. In fact, the widths of the diffraction peaks and the systematics of peak broadening were key issues during the early investigations of these alloys. There were several reasons for this. First, the structures described above, particularly the icosahedral glass model and the ideal quasicrystalline model, are distinguished primarily by the disorder present in the former and absent in the latter. A careful study of disorder in real samples, could be used to validate one structure or the other. Secondly, all of the early icosahedral alloys exhibited diffraction peak broadening that could not be eliminated by traditional strain relief techniques such as annealing. The peak

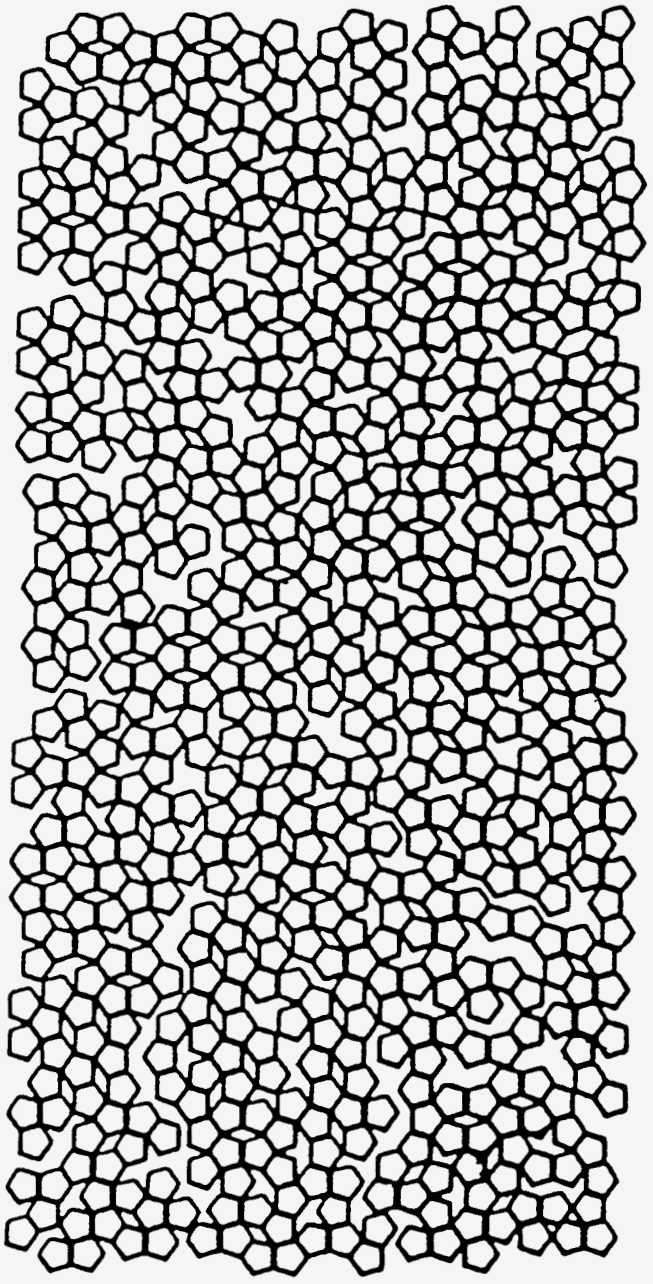

Fig. 1.12. Shown is a random assortment of oriented pentagons which can be viewed as a two dimensional analog of an icosahedral glass.[44]

broadening in all alloys was virtually identical, corresponding to a positional correlation length smaller than about 1000 Angstroms. This led to the conjecture that icosahedral structures were somehow intrinsically defected, akin to the icosahedral glass model. Finally, the mechanism of peak broadening could not be discerned since no apparent systematic trend in the peak widths could be identified.

For periodic three dimensional structures the mechanisms for diffraction peak broadening generally falls within two categories. Small crystallites, for example, will exhibit diffraction peak widths inversely proportional to the size of the grain (finite particle size broadening). In this instance, all diffraction peaks will exhibit approximately the same width. If the crystal is strained, on the other hand, the width of diffraction peaks increases with the scattering angle, 2θ, or the momentum tranfer, Q. A simple way to envision this is that strain introduces an effective range of interatomic (or interplanar) distances which "smears" out the peak with increasing scattering angle. The peak broadening from the icosahedral alloys, however, followed neither of these trends as revealed in diffraction data such as the powder diffraction in Fig. 1.2.[18b] . What is particularly unusual about this disorder is that it produces peak width broadening that varies from peak to peak. In particular, it was found that the strong reflections were relatively sharp while weak reflections showed large amounts of broadening.

The fundamental incommensurability of quasicrystals introduces a new possible mechanism for peak broadening that can be illustrated by the 1-D HT chain described above. One can imagine that nature will make many mistakes (such as stacking faults) in any attempt to grow a quasiperiodic sequence in one-dimension or a quasicrystal in three-dimension. At one extreme, the random

packing of icosahedral units in three-dimensions represents the most disordered structure consistent with the observation of overall icosahedral symmetry in the diffraction pattern. The one-dimensional analog of this structure, the HT chain, produces a diffraction pattern with characteristic peak broadening similar to that which is observed in real alloys. In our "cut and projection" description of the HT structure, this disorder arises from random shifts of the atomic surfaces along the direction perpendicular to the physical space axis, leading to a rearrangement of the L and S segments that destroys the long-range positional order characteristic of the ideal Fibonacci sequence. In a physical picture of the structure, this corresponds to the "hopping," or diffusion of atoms that flip the order of the segments in 1-D, or a rearrangement of the tiles in the 3-D quasicrystalline model. This peculiar type of disorder, unique to quasicrystals, has been termed "phason strain" if the motion of these "defects" is pinned, or "phason disorder" if the fluctuations are dynamic.

This mechanism, "phason strain", does indeed have a unique signature in the peak broadening from icosahedral alloys. As mentioned above, physical strain produces diffraction peak broadening that increases with increasing momentum transfer, Q. Phason strain may be viewed as a similar process which occurs, not in the physical space, but in the complementary perpendicular space in the higher dimensional lattice. The diffraction peak broadening from quasicrystals, as illustrated in Fig. 1.2, for Al-Li-Cu, increases with increasing $Q^{\perp}$. This mechanism for peak broadening appeared to be universal for the icosahedral quasicrystals until the discovery of a second class of icosahedral alloys in 1988.

In 1988 a new class of quasicrystals was discovered and was labeled the Face Centered Icosahedral (FCI) alloys. A large number of ternary alloys such as Al-Cu-

Fe, Al-Cu-Ru, Al-Pd-Mn, etc. fall into this category.[21,22] What was most surprising about this new set of alloys was that, when prepared properly, they presented no evidence of the phason strain that plagues the original quasicrystals, now called Simple Icosahedral (SI) alloys.[45-47] The difference between the structure of the original SI alloys and the FCI alloys was attributed to chemical ordering.[48,-49] The chemical ordering is also believed to be responsible for the absence of phason strain. Today, a large number of alloys have been discovered to present simple icosahedral symmetry and Face Centered Icosahedral symmetry. The degree of disorder varies greatly from the Al-Li-Cu alloy with correlation lengths of ~300Å to nearly perfect Al-Cu-Ru and Al-Cu-Fe with correlation lengths greater than 1μm.[45,46]

The discovery of nearly perfect samples of FCI quasicrystals has compelled us to ask "How perfect can a quasicrystal be?" The resolution of this question was the initial goal of this thesis topic. The following chapters of this thesis are organized as follows. First, a description of the growth method and parameters for obtaining high quality single crystals of FCI Al-Pd-Mn for x-ray and neutron diffraction studies is presented. Next, a method for obtaining and using a coherent x-ray beam as a means of studying order and disorder over length scales on the order of 10 microns is discussed and the results of coherent x-ray diffraction measurements from our Al-Pd-Mn samples are presented. These coherent x-ray measurements led us to the study of dynamical x-ray diffraction from quasicrystals. The fourth chapter is an introduction to the dynamical theory and its implications as applied to quasicrystals. Finally, a description of the experimental observation of dynamical diffraction in the form of the Borrmann Effect, Pendellösung Fringes and high resolution x-ray topographs from icosahedral Al-Pd-Mn quasicrystals is presented.

II. SAMPLE PREPARATION

Introduction

Before any of these experiments could be performed it was necessary to obtain a single quasicrystalline sample of sufficiently high quality. The study of coherent x-ray diffraction and dynamical x-ray diffraction requires large grains of highly perfect crystals (or quasicrystals) with flat, strain-free surfaces. Often the samples must be prepared in the form of parallel faced wafers of a specified thicknesses (0.2 mm - 1 mm). The surface normals must be carefully oriented with respect to the high symmetry directions (e.g. fivefold, twofold, threefold) to be studied.

The rapid rate of development of the dynamical theory of x-ray diffraction during the early 1960s was a direct result of the new availability of high quality crystals of silicon. Researchers have, throughout the years, developed and optimized techniques for preparing strain free samples of silicon and germanium. Optimized preparation techniques for the production of strain free quasicrystals, in particular Al-Pd-Mn,[50-54] have not, until now, been developed. In particular, details of the growth parameters had to be optimized, techniques for the preparation of strain free surfaces required development and, although many researchers in the field have attempted to produce a chemical etching technique to reveal grain boundaries in quasicrystalline samples, no succesful solution had been found.

Here, I will describe the procedures that we have developed for the production of highly perfect icosahedral Al-Pd-Mn samples at the Ames Laboratory, as well as techniques for preparing strain free surfaces appropriate for surface studies by means of x-ray and Low Energy Electron Diffraction (LEED) techniques.

Finally, a description of a chemical etching technique that reveals the grain boundaries in an ingot is described.

Crystal Growth

The steps involved in sample production for these studies include crystal growth, followed by grain extraction, surface preparation and grain characterization. The analysis of the final product can then be used to revise the growth parameters as well as the other sample preparation techniques in order to eventually optimize the quality of the sample.

Single crystals were grown from $Al_{70}Pd_{21.5}Mn_{8.5}$ alloys by the standard Bridgman method. Starting elements with purity of 99.99% were arc melted and chill cast into a copper mold. The as cast ingot was placed into an alumina crucible in a Bridgman apparatus. We also performed growths by using various other crucibles (such as graphite and boron nitride) and found that the alumina crucible was least reactive with the sample as well as less likely to promote nucleation sites that minimize grain size. The chamber was evacuated to 1.3×10^{-4} Pa and the sample temperature was raised to 300° C for 30 minutes, in order to extract water and other contaminants. The furnace was then backfilled to 2.06×10^{5} Pa of argon gas. The sample was then heated above its melting point, to 1050° C. The crucible was pulled out of the high temperature region of the furnace at a specified rate.

The quality of the final product proved to be highly sensitive to the growth rate. For example, setting the growth rate to 0.5 mm/hr produced an ingot with large compositional variations from the top to bottom of the ingot. When the growth rate was larger than 2 mm/hr the ingot was composed of a large number of

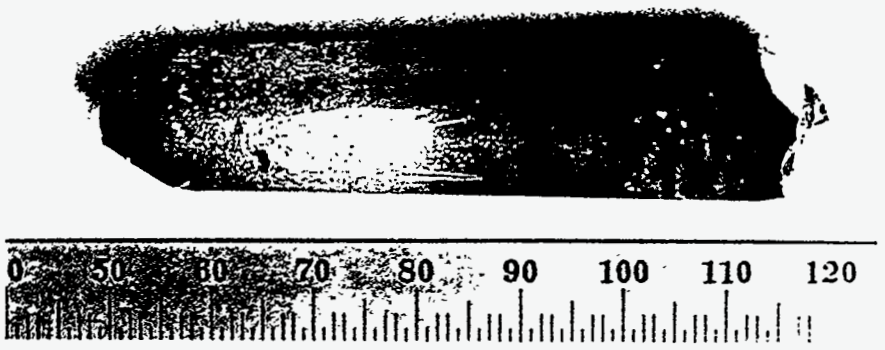

Fig. 2.1 A photograph of an ingot of icosahedral Al-Pd-Mn grown by means of the Bridgman method. The scale is in millimeters.

small grains. The best results were obtained with a growth rate of 1 mm/hr (Fig. 2.1), producing large grains, some extending over the full length of the ingot.

Grain Extraction

Grains were located by means of neutron diffraction techniques performed at the Missouri University Research Reactor and by x-ray Laue photographs performed in our laboratory. The neutron diffraction technique consisted of mounting the ingot on a four circle diffractometer and taking Polaroid photographs of the strongest Bragg reflections in order to obtain projected images of the individual grains. The various projected images were then associated with regions of the sample until most of volume of the ingot was accounted for (Fig. 2.2). The Polaroid film was then replaced by a detector and the mosaic width of each grain was determined.

Alternatively, x-ray Laue photographs, taken at carefully selected points over the surface of the ingot, could be used to determine the approximate location of grains and grain boundaries. The information gained from these two

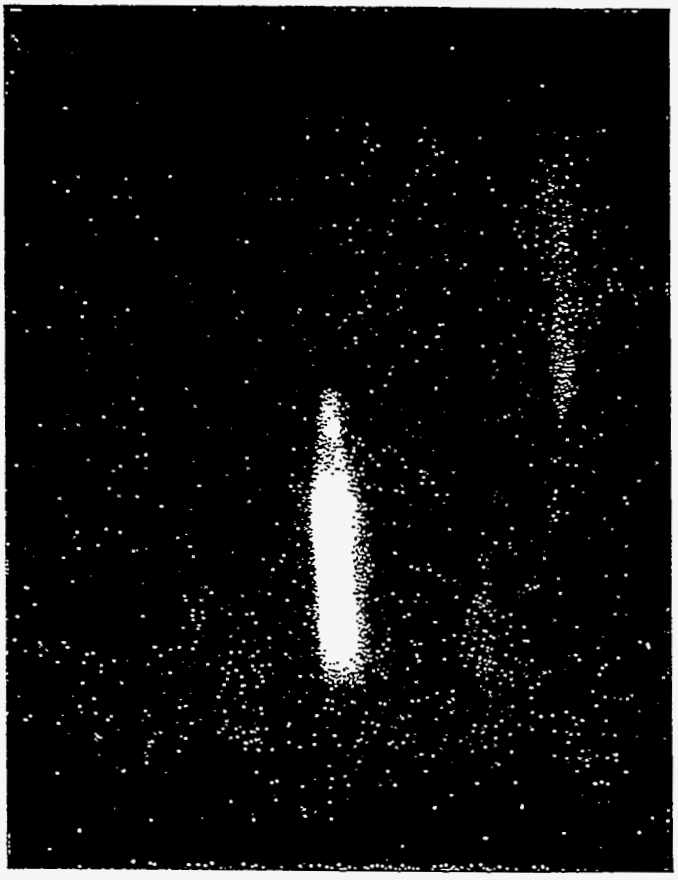

Fig. 2.2. A Polaroid photograph of a strong reflection of neutrons. The Background reveals weak reflections from other portions of the ingot. The image is a 1:1 projection of the scattering grain. The exposure time is 30 seconds.

complementary techniques enabled the identification of individual grains. These grains were then extracted and cut to the desired shape by means of a diamond wafering saw. As each new surface was cut, a series of x-ray Laue photographs were taken, revealing the newly accessible grain boundaries. The process was

continued until Laue photographs taken from any point on the sample proved to be consistent with what was expected from a single grain. Eventually, individual grains as large a 2 cm x 1 cm x 1 cm were extracted. The best grains exhibited resolution limited mosaic widths, ($\Delta\theta<0.02°$), by neutron diffraction measurements.

Surface Preparation

Dynamical x-ray diffraction studies demand samples with strain free surfaces. For many studies performed on silicon and germanium, it is sufficient to first polish the surface with 600 grit paper followed by a fine compound (for example 1-6um diamond compound) and, finally, chemical etching of the sample with an acid solution. Unfortunately, these methods are not applicable to Al-Pd-Mn, an intermetalic alloy with strong corrosive resistant properties. It was found that a relatively strain free surface could be produced in the following manner: The sample was first polished with 2000 grit sandpaper, then with 6, 1, and 0.25 μm diamond compound in that order. Alumina combined with water was found to react with Al-Pd-Mn and therefore could not be used. Surprisingly, no chemical etch, as was necessary for silicon and germanium, was required to obtain Al-Pd-Mn surfaces suitable for dynamical diffraction studies.

While sufficient for bulk dynamical diffraction measurements, the above technique did not produce surfaces of the high quality necessary for surface studies. The additional step of electropolishing the Al-Pd-Mn sample was required. In order to electropolish Al-Pd-Mn a solution of 1.0 vol. % Triflic Acid/Methanol was used.[55] The solution was stirred slowly by a magnetic stirrer while the temperature was held at approximately -70° C. The sample, previously polished with 2000 grit sandpaper, was pressed against a counter-sunk hole in a flat parallel faced stainless

steel electrode. The opposite electrode, a parallel faced plate, was placed approximately 5 mm from the first electrode so as to form a parallel plate capacitor. The two electrodes were connected to the voltage source and submerged in the solution. The advantage of this technique was that although the sample size and shape varied from sample to sample, the configuration of the electrodes and thus the field between the electrodes was equivalent and uniform. The combination of a uniform electric field and a uniform electrolyte rate of flow across the entire face of the sample produced a consistent electropolishing rate over the entire face of the sample that could be controlled by varying the voltage. The current through the electrodes was measured as the voltage across the electrodes was varied. A plot was produced (Fig. 2.3) and we found that the sample polished most uniformly in the voltage range of 52-56 Volts (a region where the current density is least sensitive to the applied voltage).

In order to determine the degree of surface perfection of the samples, LEED studies were performed. For these measurements, a parallel-faced wafer with a fivefold symmetry axis normal to the electropolished surface was mounted in an ultra high vacuum chamber. The surface was cleaned by means of 1000 eV argon-ion bombardment followed by a 600-700° C annealing cycle. After repeated sputtering and annealing cycles, the sample produced LEED patterns (Fig. 2.4) which exhibited five fold symmetry and were consistent with what would be expected from a quasicrystalline surface. The LEED spots were observed for incident electron energies in the range of 5 eV to 240 eV. Within the resolution of the LEED apparatus, no structural phase transition was detected within the temperature range 20 and 700° C.

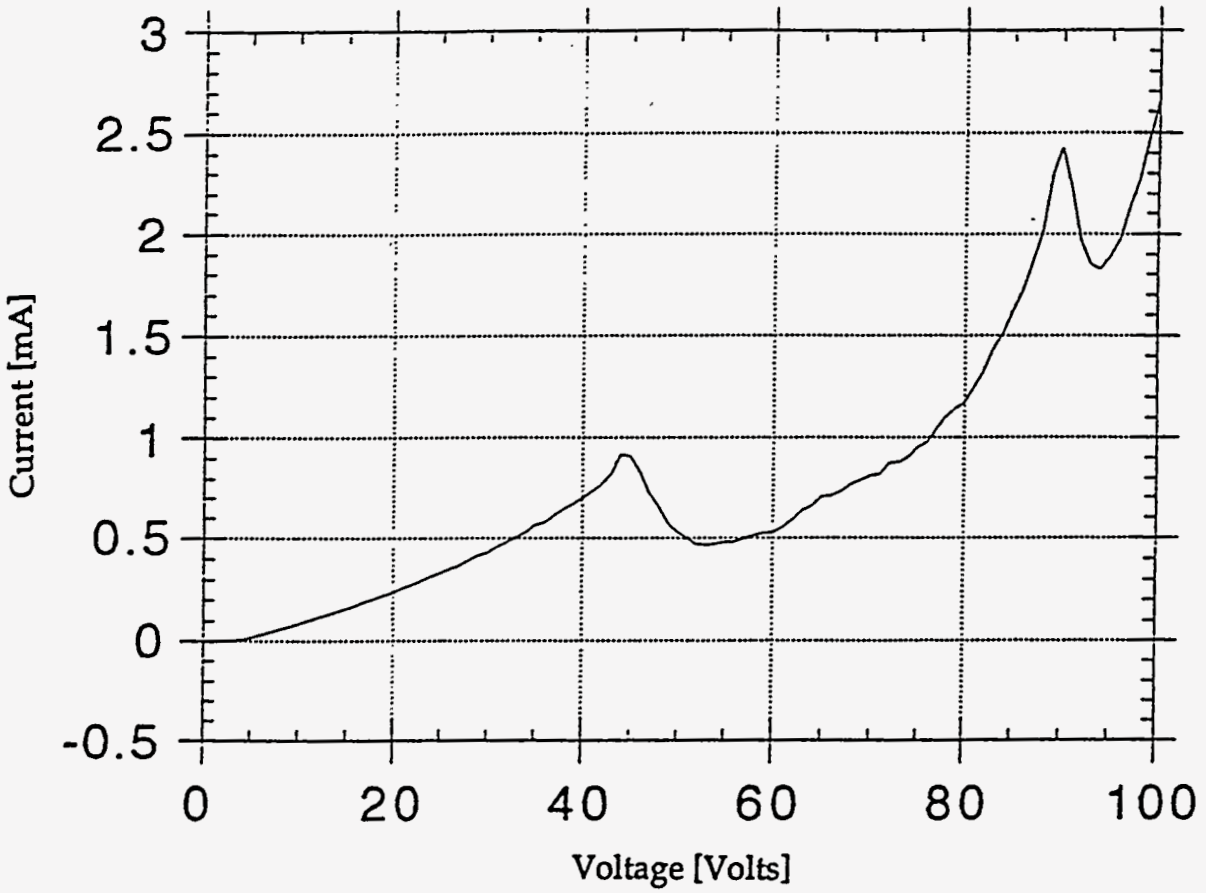

Fig. 2.3. Plot of current vs. voltage during the electropolishing process. The most uniform polishing was attained at voltages between 52 and 56 volts.

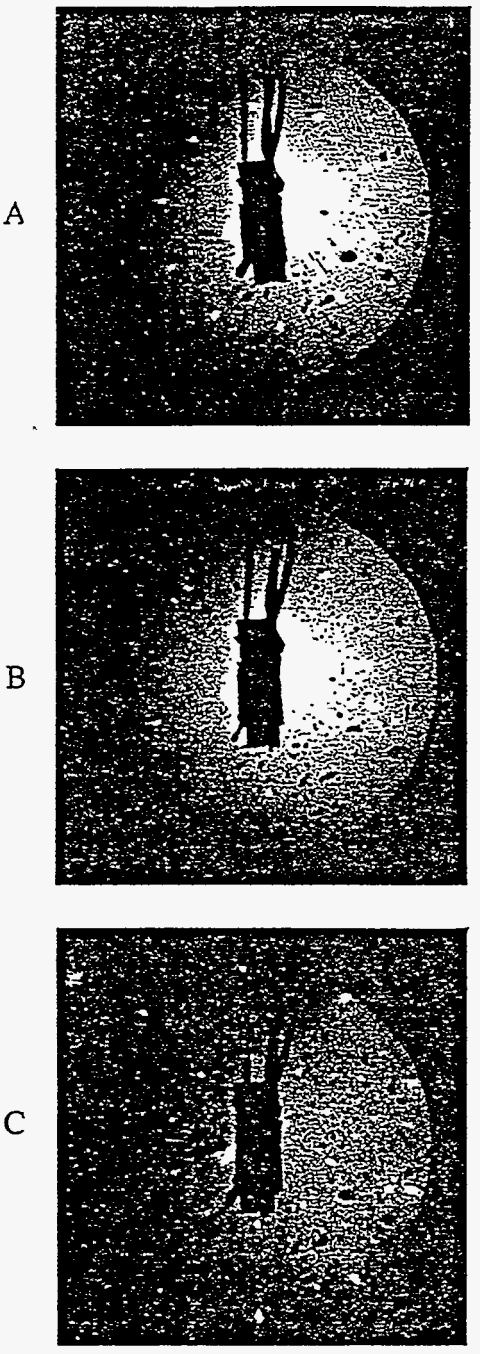

Fig. 2.4. Low energy electron diffraction patterns from Al-Pd-Mn at electron energies of a) 18 eV, b) 24 eV and c) 33 eV show fivefold diffraction patterns

Comments on Surface Quality

We have found that the non-electropolished surfaces did not produce LEED patterns even after much effort. This obseration implies that the electropolished surface with a fivefold axis parallel to the normal exhibits less strain than the equivalently oriented mechanically polished surface. It is interesting to note that for dynamical x-ray diffraction, the method of surface preparation is less significant. This can be seen by means of high resolution x-ray topography. Fig. 2.5 is a transmission topograph (see chapter 5) from a sample with a five fold axis along the surface normal. The central portion of the surface was electropolished (the border of the electropolished region can be seen as a circle where the electropolishing was imperfect and caused tarnishing of the surface). The diffracted intensity from the mechanically polished region and the electropolished region are essentially indistinguishable. Measurements of rocking curves by Roberto Colella from equivalently prepared samples also support this conclusion.[56]

Chemical Etching (Macro-Etch)

The problem of developing a macro-etch for Al-Pd-Mn has concerned many researchers in the field. The Al-Pd-Mn alloy seems to be insensitive to most etches, other than solutions of hydrofluoric acid and nitric acid. Yet the nitric-hydrofluoric solution does not effectively reveal any grain boundaries, but rather turns the surface black.

After many attempts, we found that a 40:60 HF-Nitric acid solution cooled in an ice water bath works very well as a macro-etch for Al-Pd-Mn. The lower temperature reduces the reaction rate. While the sample usually turns black at first

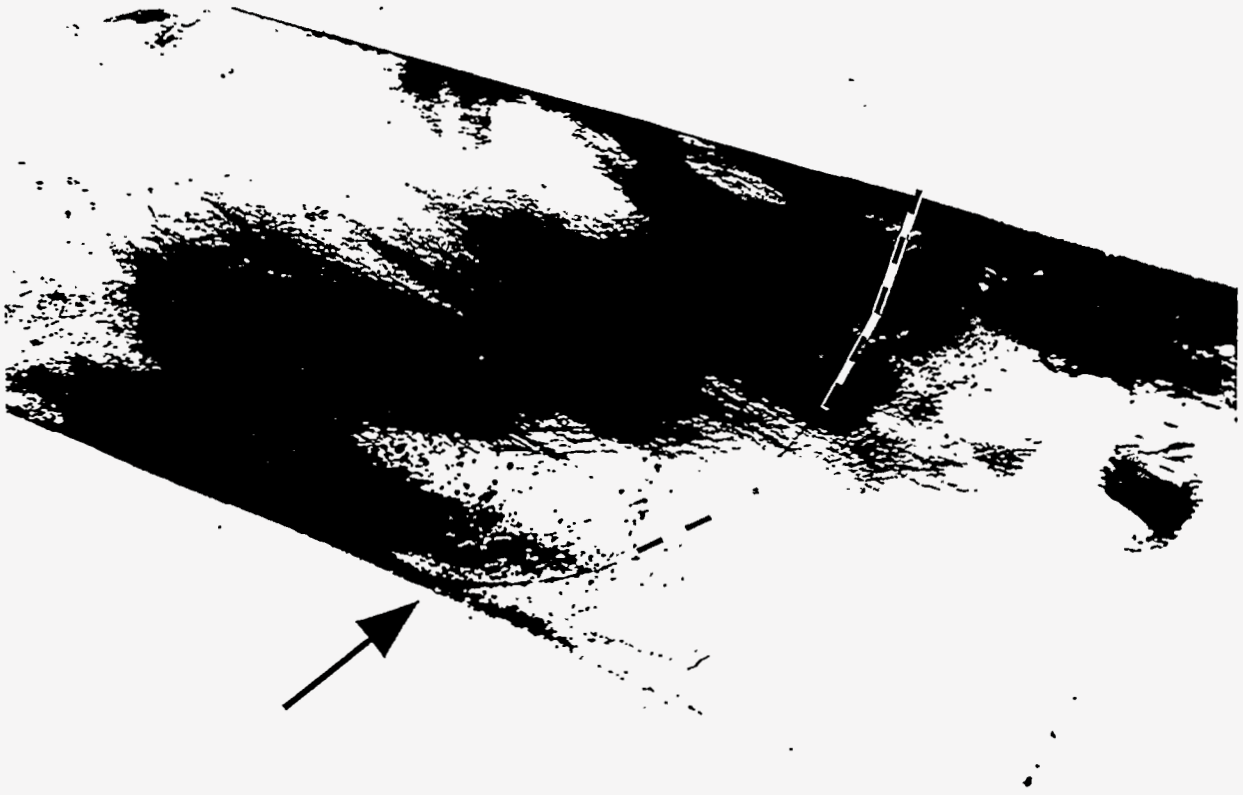

Fig. 2.5. High resolution transmission x-ray topograph of a parallel faced 0.4 mm thick sample. The diffraction of x-rays from the electropolished (left side of sample) and mechanically polished regions (right side of sample) is essentially the same. Arrows signify the boundary between mechanically polished and electropolished regions.

(this is because the sample is initially at room temperature), the corrosion flakes off and a metallic surface is again revealed. The sample is then washed in a cold bath of water or alcohol to prevent tarnishing.

It might be possible to modify this technique to obtain a slow etch for the preparation of strain free surfaces. Unfortunately, it is difficult to prevent some tarnishing of the sample. Nevertheless, it simplifies the procedure for identifying the grains in the sample. In addition, it is possible to quickly reveal details of the quality of the ingot. For example, it is easy to recognize regions in the ingot that contain dendritic growth (as shown in Fig. 2.6), which is to be avoided as a sample for dynamical x-ray diffraction experiments.

The preparation of high quality samples of icosahedral Al-Pd-Mn has enabled researchers to perform a range of experiments that were not believed to be possible for the study of quasicrystals. We have continued to increase our understanding of quasicrystals by participating in collaborative efforts on a range of experiments. For example, in collaboration with Pat Thiel's group, to better understand the surface structure and surface properties we have continued to study Al-Pd-Mn samples by means of low energy electron diffraction measurements and scanning tunneling microscopy.[57] We plan to perform x-ray surface scattering measurements at the National Synchrotron Light Source at Brookhaven National Laboratory. Angular-resolved photoemmision measurements were performed in collaboration with David Lynch's group and have produced information about the electronic density of states.[58] Collaborations with David Black at the National Institute of Standards and Technology has allowed us to use x-ray topography to resolve defects in the bulk sample and will allow the characterization of defects in quasicrystals. Diffuse scattering by means of elastic neutron scattering studies were conducted in

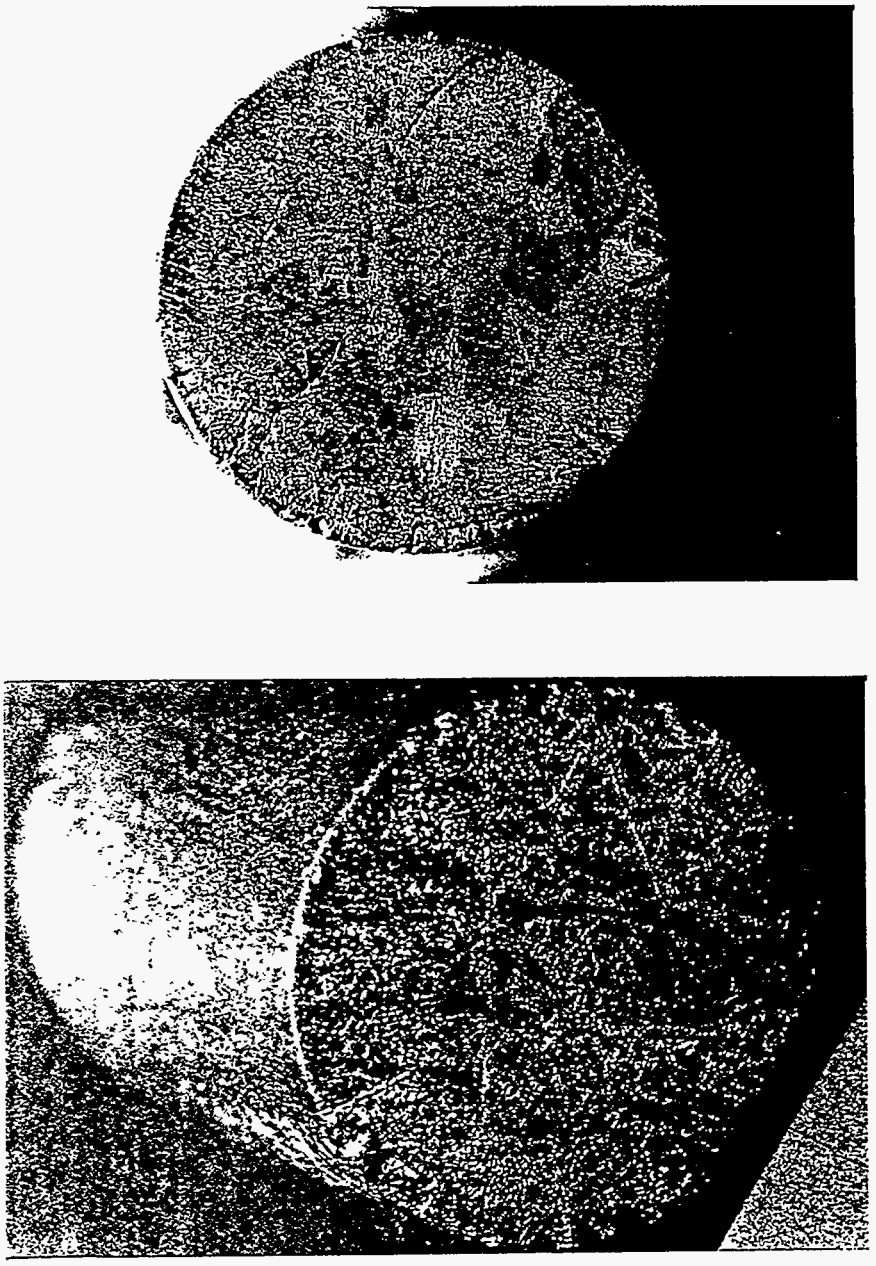

Fig. 2.6. Magnified photographs of a cross sectional cuts (diameter = 14 mm) from an ingot after being polished and then chemically etched. The chemical etching reveals grain boundaries in two different regions of an ingot. The top photo presents large grains while the bottom photo reveals a large number of small grains .

collaboration with Marc de Boissieu, Michel Boudard and others from Grenoble to study disorder in quasicrystals.[59] A collaboration with Fred Mueller and Evert Haanappel of Los Alamos National Laboratory and the National High Magnetic Field Laboratory has allowed us to observe the De Haas-van Alphen effect on appropriately prepared samples of Al-Pd-Mn which will eventually allow us to describe the Fermi surface of the Al-Pd-Mn quasicrystal.[60]

III. COHERENT X-RAY DIFFRACTION MEASUREMENTS

Introduction

One of the most interesting and fundamental issues concerning quasicrystals has been the degree of perfection possible in aperiodic structures. Quasicrystals, as was explained in the introductory chapter, exhibit an interesting form of disorder called phason strain. It has been found that quasicrystalline alloys present a varied degree of phason disorder which, in turn, indicates whether the crystal is best described by an icosahedral glass model or the ideal quasicrystalline model. The discovery that the FCI alloys reveal resolution limited x-ray diffraction peaks implies that if details of disorder in these highly perfect quasicrystals are to be resolved, a probe sensitive to larger length scales will need to be applied. Conventional high resolution x-ray diffraction methods are limited to length scales on the order of one micron. In this chapter, we focus on the applicability of coherent x-ray diffraction as a probe that is sensitive to order and disorder over length scales of about ten microns.

X-ray diffraction experiments are typically done with beam sizes of several hundred microns to one millimeter. In these measurements, the incident radiation is incoherent and defects such as dislocations, strain and domain structures produce longitudinal and/or transverse broadening of diffraction peaks. In the measurement technique described in this chapter, a beam size on the order of the natural transverse coherence length of the synchrotron radiation is employed, thus producing a coherent beam. As demonstrated by Sutton et al.,[61] the coherent incident beam may be used to study the x-ray speckle pattern produced by the presence of defects in the region illuminated by the beam, and so provides a

sensitive probe of the presence of strain and disorder in materials. For instance, it has already been pointed out by Garg and Levine[62] that the disorder inherent to random packing models for the icosahedral phase should produce observable speckle in diffraction patterns taken using a coherent incident beam. Indeed, this result should hold for quasicrystals with any significant degree of phason strain. This chapter contains an introduction to the basic requirements for the observation of speckle in the x-ray regime. In addition, several calculated speckle patterns from two model quasicrystal grains of varied phason disorder are presented. Finally, results from an x-ray speckle experiment that was performed on Al-Pd-Mn are described.

The Coherent Beam and Speckle

When light from a coherent source, such as a laser, is reflected from a rough surface, the reflection appears "grainy". The effect is due to the fact that different portions of the surface introduce random phase shifts to the reflected beam. The reflected light interferes coherently, thus allowing constructive and destructive interference producing a speckle pattern. Because this is an interference effect, it is not possible to observe speckle involving length scales less than about 200 nm, for visible light. If one is interested in observing speckle from disorder on atomic length scales, it is necessary to use an x-ray source.

The feasibility of producing a speckle pattern with presently existing x-ray sources was realized by Sutton et al.[61] The principle requirement for the observation of speckle is that the incident beam itself must have sufficient longitudinal and transverse coherence. With visible light this is typically achieved with a laser source, although it is possible to use an incoherent source, such as a

mercury arc lamp, provided that the beam is sufficiently well collimated. Carrying this idea over to the x-ray regime, Sutton et al. demonstrated that the speckle pattern of disordered, or partially ordered, alloys may be studied by the coherent scattering of x-rays. The high brilliance of the X25 wiggler beam line at the NSLS was used to produce a coherent x-ray beam of $\sim 3\times10^5$ photons$\cdot s^{-1}$ in a beam spot of size ~6 μm. Using this source, the speckle pattern from the (001) diffuse reflection of a partially disordered sample of Cu_3Au was resolved.

The Coherent X-Ray Beam

It is possible to describe the coherence of a beam by three parameters: the longitudinal coherence length, the temporal coherence length and the transverse coherence length.[63a]

The longitudinal coherence length is a measure of the distance, along the direction of propagation, over which the incident waves are coupled coherently. The longitudinal and temporal coherence of the beam, then, are related by $\Delta x = c\Delta t$, and therefore, as described below, the monochromaticity of the source.

The x-ray beam emitted from a source can be represented by a distribution of spherical wave pulses, or wave trains, of finite duration and varied wavelength, emitted from a large number of infinitesimal volumes that together make up the volume of the source. The distance from the source to the point of observation can most often be assumed to be much greater than the dimensions of the source thus allowing the spherical waves to be approximated by plane waves. A narrow distribution of frequencies is selected by a monochromator. We focus first on the radiation emitted by one infinitesimal source volume and assume it to be represented by a gaussian distribution of frequencies centered about ω_0. The full

width at half maximum of the gaussian is $\Delta\omega$ and is dependent upon the acceptance of the monochromator. The field amplitude distribution can then be written:

$$\bar{E}(\omega) = \bar{E}_o \exp\left[-4\ln 2\left(\frac{\omega-\omega_o}{\Delta\omega}\right)^2\right]. \tag{3-1}$$

The Fourier transform allows the field amplitude to be written in the time domain as

$$\bar{E}(t) = \int_{-\infty}^{\infty} \bar{E}_o \exp\left[-4\ln 2\left(\frac{\omega-\omega_o}{\Delta\omega}\right)^2\right]\exp(i\omega t)d\omega, \tag{3-2}$$

$$\bar{E}(t) = \bar{E}_o \exp\left[-4\ln 2\left(\frac{t-t_o}{\Delta t}\right)^2\right]\exp[i\omega_o t], \tag{3-3}$$

where $\Delta t = 2\pi/\Delta\omega$. This relates the bandwidth of a wave to the width of the monochromatic wave pulse in the time domain (Fig. 3.1). This width is called the

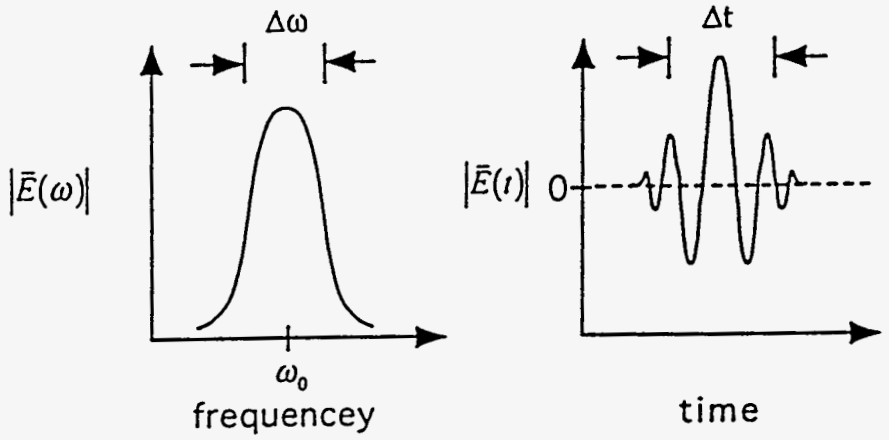

Fig. 3.1. Light possesing a guassian like distribution of frequencies in the frequency domain can be represented as a pulse of finite duration in the time domain.

temporal coherence length, $\Delta\tau$ and is an indication of the duration of time for which a wave pulse is continuously emitted from the source. It should be noted that if the distribution of frequencies is represented by a delta function (as for an ideally monochromatic source) then the wave pulses become infinitely long and the temporal coherence length goes to infinity. On the other hand, an x-ray beam from a quasi-monochromatic infinitesmal source volume is composed of a distribution of continuous plane waves of varied frequency and can equivalently be viewed as a sequence of coherent wave pulses of frequency $\Delta\omega_0$. The beam from a source of finite extent can be looked upon as a sum of such pulses, each pulse being emitted at a different time from the source volume. This summation of overlapping pulses creates a continuous x-ray beam.

We define the distance ξ_l, called the longitudinal coherence length, as $\xi_l = c\Delta\tau$. The longitudinal coherence length is a measure of the average length of a coherent pulse. There will be little interference between x-rays which have path differences exceeding ξ_l. It is possible to relate the longitudinal coherence length to the wavelength spread if we recall that

$$\lambda = 2\pi c / \omega \tag{3-4}$$

and

$$\Delta\omega = \frac{2\pi c}{\lambda^2}\Delta\lambda. \tag{3-5}$$

So that

$$\xi_l = \frac{\lambda^2}{\Delta\lambda}. \tag{3-6}$$

This implies that after being monochromated by a Si (111) double crystal monochromator, having $\Delta\lambda / \lambda \approx 1.4\times10^{-4}$ for 1.5 Å x-rays, $\xi_l \approx 1$ μm. It is of course possible to take advantage of a more selective monochromator but not without the drawback of reducing the intensity of the beam. For our purposes, it is essential that

the scattering volume be illuminated by coherently related x-rays. This means that the effective thickness of the sample must be smaller than the longitudinal coherence length. This limit can be acheived by limiting the actual thickness of the sample to less than 1 μm or by selecting the energy of the x-rays so that the photoelectric absorption limits the scattering to within 1 μm of the surface.

Transverse Coherence Length

The problem of determining the transverse coherence length of an extended quasi-monochromatic source is a question of calculating the degree of coherence of the emitted radiation at two arbitrary points of observation, P_1 and P_2 displaced from each other by a vector in the direction transverse to the propogation of the beam (Fig. 3.2). The dimensions of the source, as well as the distance between any two points P_1 and P_2 of observation, are assumed to be very small in comparison with the distance between the source and the points of observation. These assumptions allow us to ignore effects due to finite longitudinal coherence. It is then appropriate to define the correlation function as:

$$\mu(\vec{r}_1,\vec{r}_2)=\frac{1}{\sqrt{I(\vec{r}_1)}}\frac{1}{\sqrt{I(\vec{r}_2)}}\left|\int_s I(\vec{r}')\frac{\exp\left[i\vec{k}\cdot(\vec{r}_1-\vec{r}_2)\right]}{|\vec{r}_1-\vec{r}'||\vec{r}_2-\vec{r}'|}d\vec{r}'\right| \tag{3-7}$$

where

$$I(\vec{r}_1)=\int_s\frac{I(\vec{r}')}{|\vec{r}_1-\vec{r}'|^2}d\vec{r}' \text{ and } I(\vec{r}_2)=\int_s\frac{I(\vec{r}')}{|\vec{r}_2-\vec{r}'|^2}d\vec{r}' \tag{3-8}$$

The points P_1 and P_2 are represented by vectors $\vec{r}_1$ and $\vec{r}_2$ drawn from the center of the source. $I(\vec{r}_1)$and $I(\vec{r}_2)$ are the intensities at points P_1 and P_2 respectively while $I(\vec{r}')$ is the intensity distribution of the source as a function of position. $\vec{r}'$ is a

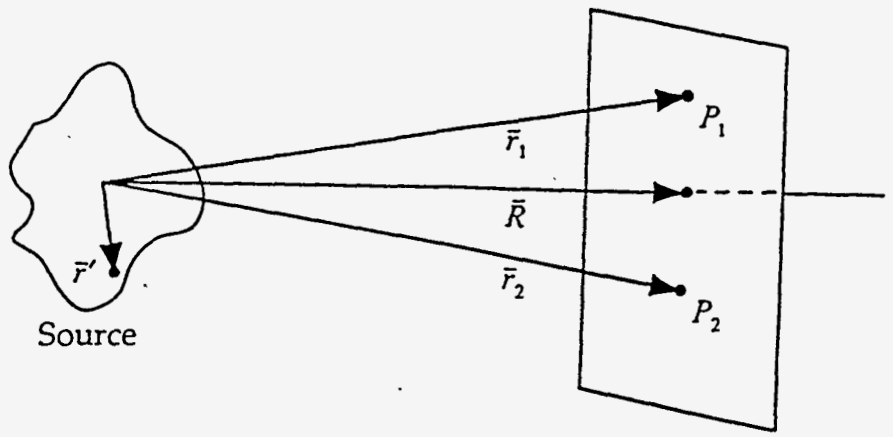

Fig. 3.2 The transverse coherence of the light a distance R from a quasi-monochromatic source of finite extent is a measure of the mutual coherence between the light at points of observation P_1 and P_2 in a plane perpendicular to the direction of propogation.

"dummy" variable of the integration which is over the volume of the source. The coherence function will take on a magnitude between 0 and 1, depending on the degree of coherence between the radiation at points P_1 and P_2

The *van Cittert-Zernike theorem* of optics states that the above integral is equivalent to one describing the complex field amplitude in the diffraction pattern on an opaque screen, arising from diffraction of a coherent spherical wave from an aperture. More specifically, this diffraction pattern will be produced if the source is replaced by an aperture of the same shape. Furthermore, the field amplitude distribution of the spherical wave is proportional to the intensity distribution of the

source. The pattern is centered at point P_1 with a normalized peak intensity of unity. The intensity at point P_2 is equal to $\mu(\vec{r}_1,\vec{r}_2)$ which will vary between 0 and 1 depending on the distance between the points P_1 and P_2

In order to determine an approximate value of the natural transverse coherence length of an x-ray source, the source can be approximated as a uniform disk of diameter d_s, a distance R from the point of observation. The correlation function will be simply that of diffraction from a circular aperture. This solution can be found in many optics texts and is

$$\mu(\vec{r}_1,\vec{r}_2)=\frac{2J_1\left(\frac{\pi d_s}{R\lambda}|\vec{r}_2-\vec{r}_1|\right)}{\frac{\pi d_s}{R\lambda}|\vec{r}_2-\vec{r}_1|} \tag{3-9}$$

or $\mu(z)=\frac{2J_1(z)}{z}$

where $z=\frac{\pi d_s}{R\lambda}|\vec{r}_2-\vec{r}_1|$ and J_1 is the Bessel function of the first kind and of first order. When z=0, the correlation function is unity, while as z increases towards the first root of the Bessel function, at z=3.83, $\mu(z)$ steadily decreases to zero. The correlation function will be at half maximum when z=2.22. The transverse correlation length is defined as the full width at half maximum of the correlation function, therefore

$$\xi_t=\frac{4.44\lambda R}{\pi d_s}\sim\frac{\lambda R}{d_s}. \tag{3-10}$$

It is possible to calculate the natural transverse coherence expected of a rotating-anode x-ray generator source (point focus). The source size is typically 1 mm, the point of observation is about 1 meter from the source and the wavelength for $CuK\alpha_1$ is approximately 1.54 Å. This yields a transverse coherence length of 0.15 μm. Therefore, in order to achieve a coherent beam, the beam would have to limited

by a 0.15 μm collimating aperture. Beyond the practical difficulties of producing an aperture of this dimension, the remaining beam intensity would only be on the order of 0.1 photons s^{-1}. It is evident that in order to produce a coherent x-ray beam of practical intensity, it is necessary to take advantage of the high brilliance of a wiggler or undulator source at a synchrotron. We can calculate the transverse coherence length expected using the parameters appropriate for a synchrotron beam line. At the X25 beam line at the National Synchrotron Light Source, the nominal source size is 0.3 mm, the observation point is approximately 30 meters from the source and the wavelength can be set to 1.55 Å, producing a transverse coherence length of ~15 μm. Thus a source with a brilliance of 10^{15} photons s^{-1} $mrad^{-2}$ mm^{-2} per 0.1% bandwidth, when collimated through a 10 μm pinhole, is expected to deliver a usable coherent beam of ~10^6 photons s^{-1}.

The longitudinal and transverse coherence lengths, together, represent the approximate dimensions of the coherent wave pulse. In other words, the maximum volume over which the scatterers can be considered to be illuminated by coherent x-rays. The entire beam is interpreted as a continuum of such coherent wave pulses, each creating a coherent interference pattern. Each pulse is incoherently coupled with the others thus the individual patterns sum incoherently. If the scattering volume is much larger than the coherent pulse volume then the speckle pattern produced by each coherent pulse is not necessarily equivalent, the incoherent sum will typically average to produce one broadened diffuse peak. On the other hand, if the scattering volume is limited to the dimensions of the coherent pulse volume, then each coherent pulse produces equivalent coherent interference patterns which add together to preserve the speckle pattern. In the latter case, the beam is said to be

a coherent x-ray beam and can produce speckle (provided the sample is appropriate for producing speckle).

In conventional diffuse x-ray scattering with incoherent light, the angular intensity distribution of a peak is related to the type and degree of disorder in the sample. Diffuse peaks are observed in a large variety of systems and can be attributed to stacking faults, phase boundaries, twinning, phason strain in quasicrystals etc. The scattering from each of these systems can be described by the structure factor

$$F(\vec{q}) = \sum_{n=1}^{N} f_n(\vec{q}) \exp(-2\pi \vec{q} \cdot \vec{r}_n) \qquad (3\text{-}11)$$

This is a summation over all the N atoms in the sample where $f_n(\vec{q})$ is the scattering amplitude of the nth atom and $\vec{r}_n$ is the position of the nth atom. Unfortunately, it is impossible to know the positions all the atoms in a partially-disordered system (this is not a problem when performing computer simulations).

X-Ray Speckle from Cu3Au

It is convenient to focus on the example of the observation of coherent x-ray speckle from the partially ordered Cu_3Au system, since it was the first example of the observation of x-ray speckle from a partially ordered three-dimensional solid.[61]

The copper and gold atoms in the Cu_3Au crystal, at temperatures above the critical temperature of about 390°C, are randomly positioned at the atomic sites of a face centered cubic lattice.[64-66] Because of the stochiometry, each site in the structure has a 1/4 probability of being occupied by a gold atom and a 3/4 probability of being occupied by a copper atom. The crystal can be considered as

being an FCC crystal with each site occupied by a statistically average copper-gold atom.

Below the critical temperature, the structure is simple cubic with a four atom basis. Because of the four different sites that the gold atom can occupy in the basis, there will be regions of a sample having the gold atom at the (0,0,0) position, while other regions having the gold atom occupying the (1/2,1/2,0), (0,1/2,1/2) or the (1/2,0,1/2) positions. Consequently, the sample will be composed of domains of perfectly ordered cubic Cu_3Au, yet the presence of domains will introduce phase shifts in the scattering with respect to the other domains. Close to the critical temperature, these domains are quite small and so the sample is considered to be partially ordered (Fig. 3.3). The high temperature phase is FCC, as a consequence, the (001) reflection is forbidden. In the partially ordered state, Cu_3Au is

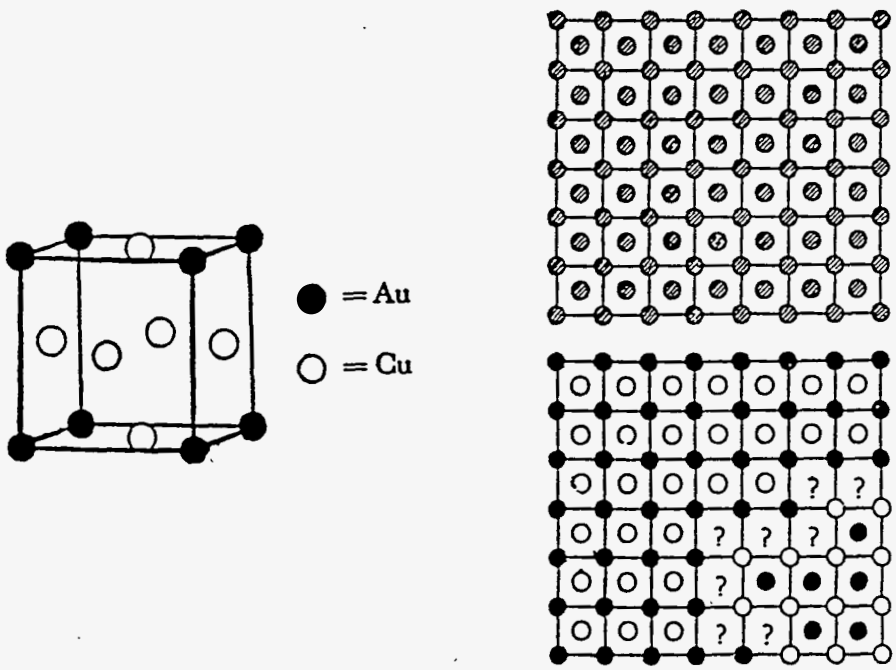

Fig. 3.3 Due to the four different ways in which the Cu_3Au atoms can be arranged in the underlying periodic crystal lattice, Cu_3Au is an excellent example of a partially ordered binary alloy exhibiting phase domains.

composed of a collection of cubic ordered domains, thus a diffuse (001) peak exists and can be viewed as arising from the superposition of contributions of scattered x-rays from a set of domains. Because of the finite domain size, each domain produces a broad diffraction peak of angular width $\sim \lambda / \xi$, where ξ is the average domain size. When incoherent x-rays are diffracted from the crystal, a diffuse peak results from the incoherent sum of the scattering from these domains. The width of the diffuse peak will be $\sim \lambda / \xi$.

The equivalent reflection, when taking advantage of a coherent x-ray beam, will be composed of the coherent sum of the scattering from the random array of domains resulting in a speckle pattern. The speckle pattern can be seen as a modulation of the conventional diffuse peak (Fig. 3.4 and Fig. 3.5). The angular

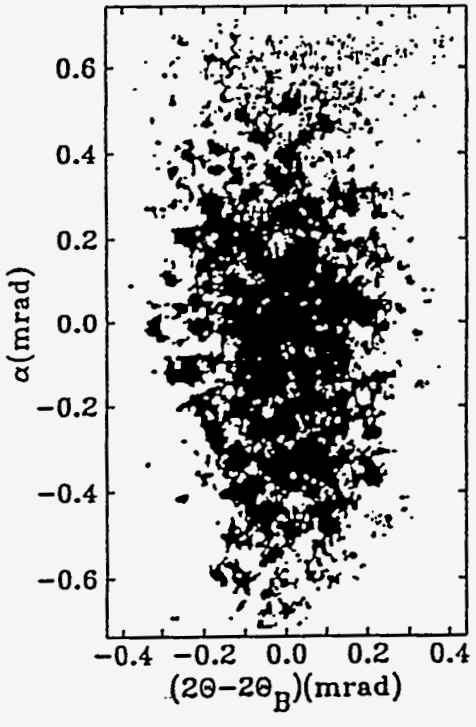

Fig. 3.4. A photograph of the speckle pattern in the diffuse (001) peak of Cu_3Au. A 2.5 μm collimating pinhole was used (therefore L=2.5 mm).[61]

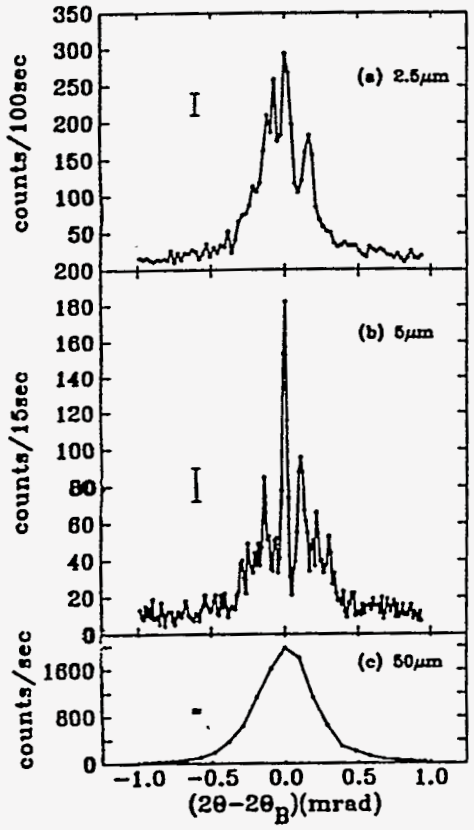

Fig. 3.5. (a) The cross-sectional intensity distribution of equivalent speckle patterns was measured by scanning a pinhole and detector transversely through the peak. The beam dimensions were limited by collimating pinholes of diameter: (a) 2.5 μm, (b) 5 μm, and (c) 50 μm. The detector pinholes were 50, 25, and 100 μm respectively. Due to the limited transverse coherence of the experimental configuration, (c) represents a conventional incoherent x-ray diffuse peak. A comparison of (a) and (b) with (c) supports the fact that the coherent speckle patterns can be viewed as modulations of the diffuse peak.[61]

extent of each "speckle" is comparable to the width of the central peak in the Fraunhofer diffraction pattern of the collimating pinhole, as this corresponds to a change of λ in the largest path-length difference. This width is $\sim \lambda / L$, where L is the beam diameter.

If we consider the Bragg diffraction of a coherent x-ray beam from a highly ordered sample ($\xi > L$) then the width of the peak will be resolution limited. In other words, the peak will be the size of a single speckle.

Calculated Speckle Patterns from Model Systems

To better understand the sensitivity of the coherent scattering technique for the study of disorder in quasicrystals, it is instructive to turn to computer simulations. I have grown two model structures. Although each model consists of a collection of 10,000 equivalently oriented icosahedrons, the packing rules and thus the degree of disorder is different (as can be seen in Fig. 3.6 and Fig. 3.7). The first model is an icosahedral glass following only three rules: that all the icosahedrons are oriented in the same way, that two clusters cannot overlap each other, and that the grain grows by randomly adding one cluster after another, each being placed so as to have its face match up with a face of one of the preexisting clusters. This produces a grain with a relatively large degree of phason strain. The second model grows by the same rules as the first modified by additional constraints introduced by Robertson et al[63b] that results in a relatively small degree of phason strain.

The speckle patterns are computed numerically by calculating the structure factor as a function of reciprocal space vector $\vec{Q}$ for an array of point scatterers

positioned at the centers of the clusters of the model $\bar{R}_n$. The expected intensity is equal to the magnitude of the squared structure factor,

$$I(\bar{Q}) = \left| \sum_n e^{i\bar{Q}\cdot\bar{R}_n} \right|^2 . \tag{3-12}$$

Speckle patterns from three reflections along the two fold axis {(0/2 0/0 0/0), (2/2 0/0 0/0) and the (2/4 0/0 0/0)} were calculated for each model and are shown in Fig. 3.8 to Fig. 3.13 respectively). It is apparent, after comparing equivalent reflections from the two contrasting models, that the icosahedral glass, presents broader, richer speckle patterns as compared to the more ordered model. In addition, the width of the patterns is related to the perpendicular components of the six dimensional reciprocal lattice vectors. In other words, the larger the $Q_\perp$ of a peak, the broader is the speckle pattern.

These calculations show that coherent x-ray speckle may be a sensitive probe for the study of disorder in quasicrystals. It should be interesting to resolve a speckle pattern from an actual quasicrystal and compare the results with computer models to better understand the details of phason strain in quasicrystals.

Experiment

The coherent x-ray diffraction line shape measurements were done on the X25 wiggler beam line at the National Synchrotron Light Source (NSLS) using a Si (111) monochromator set to diffract 7 keV (λ=1.77 Å) x-rays. The scattering geometry is shown in Fig. 3.14. The energy resolution was calculated to be $\delta\lambda / \lambda \approx 1.4\times10^{-4}$, yielding a longitudinal coherence length, $\lambda^2 / \delta\lambda$ on the order of 1 μm. The transverse coherence length of the incident beam is on the order of $\lambda R_s / d_s$, where R_s is the distance from the source and d_s is the source size. For the NSLS, the vertical

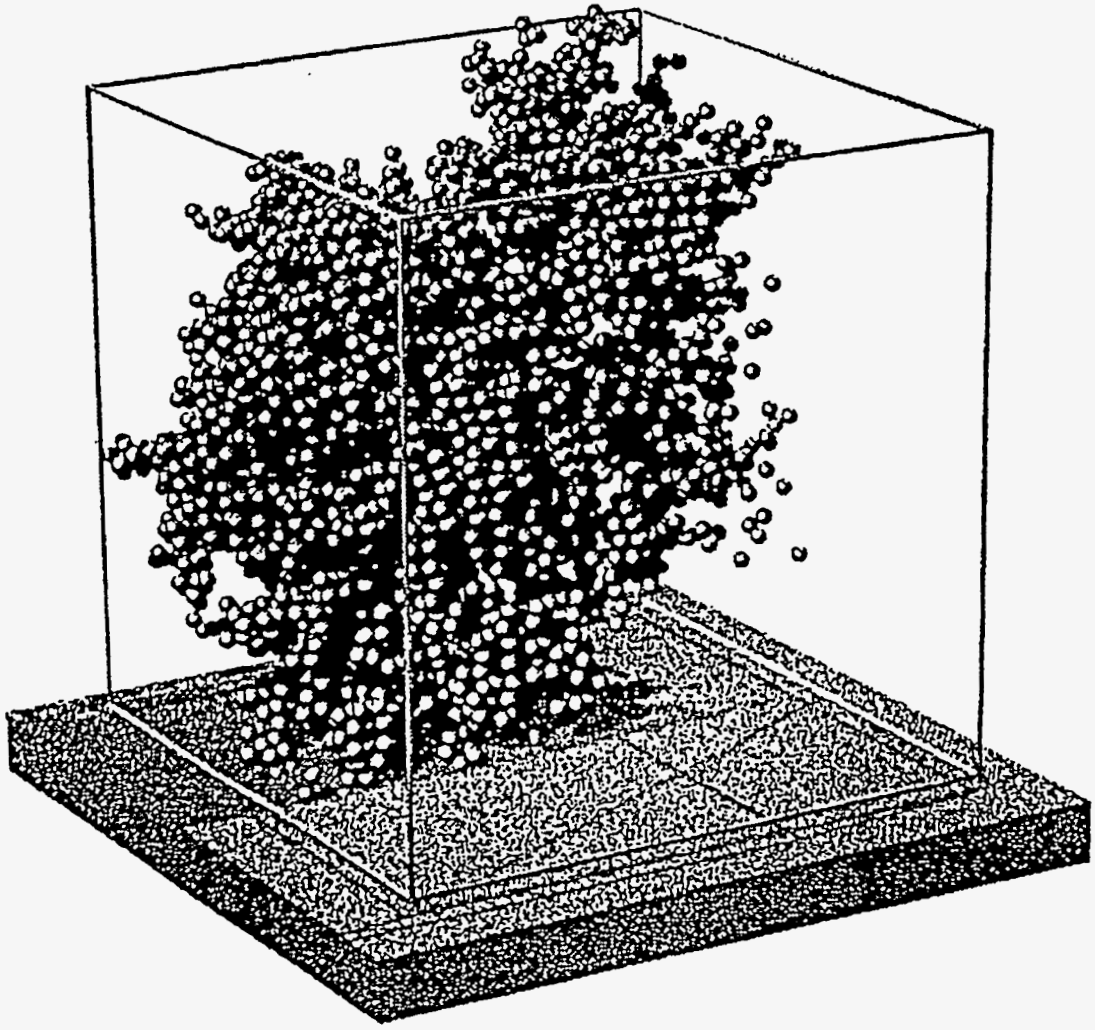

Fig. 3.6. One half of a computer constructed icosahedral glass consisting of ten thousand clusters. Due to the minimal amount of growth constraints, the structure exhibits a large degree of phason disorder.

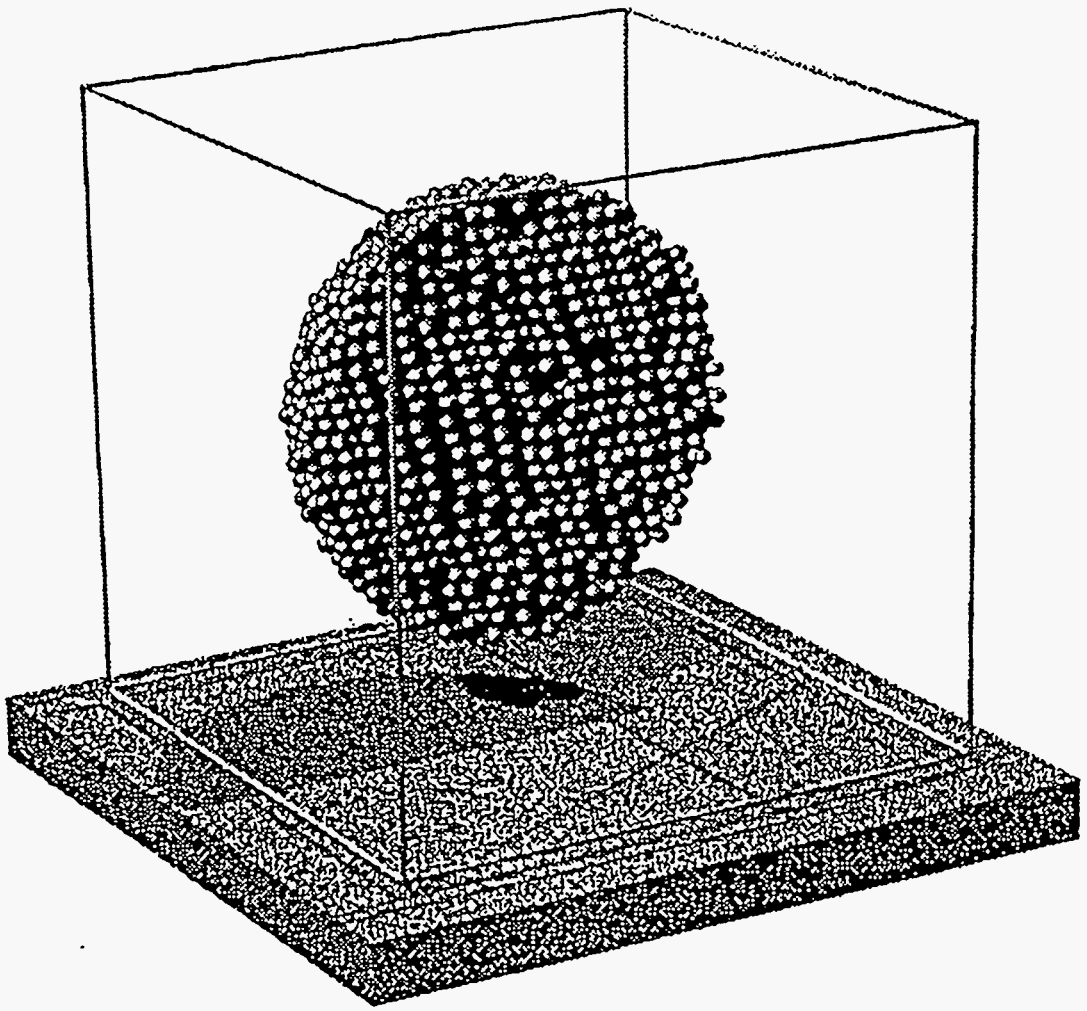

Fig. 3.7. One half of a computer constructed icosahedral glass consisting of ten thousand clusters. Due to the inclusion of growth constraints, consistent with the "Robertson model," the structure exhibits a relatively small degree of phason disorder.

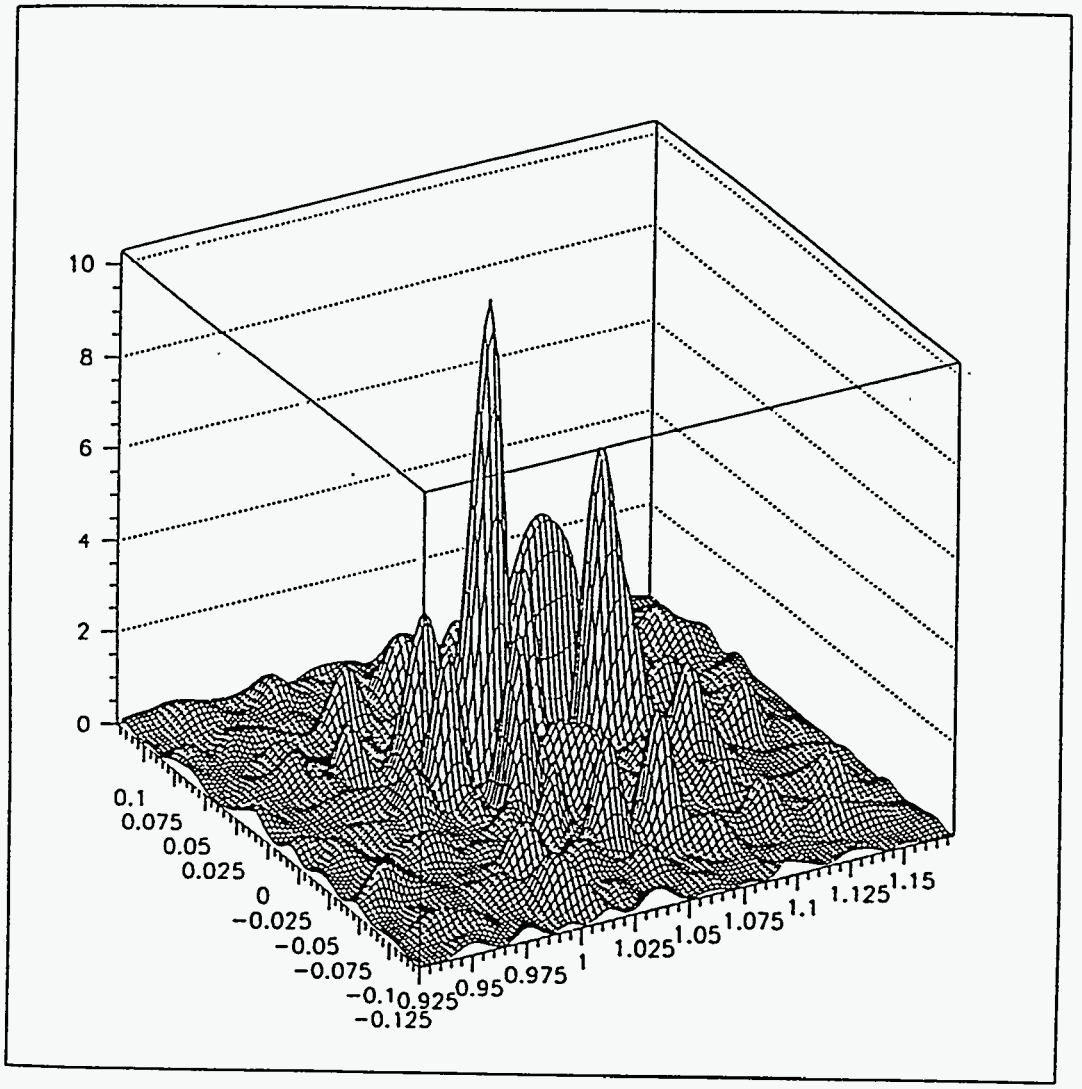

Fig. 3.8. The 4/4 speckle pattern from a computer constructed icosahedral glass consisting of ten thousand clusters. The pattern displays a large amount of speckle.

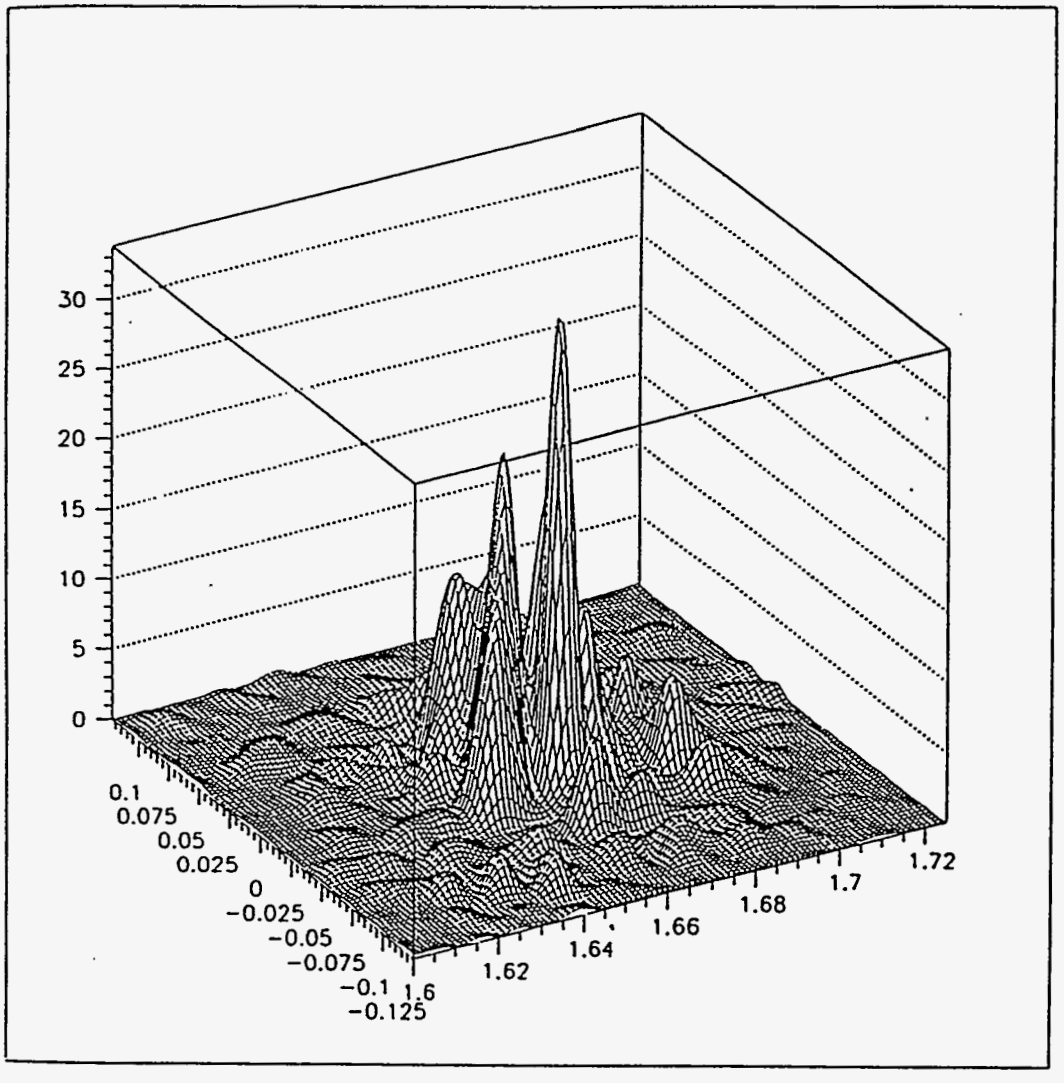

Fig. 3.9. The 8/12 speckle pattern from a computer constructed icosahedral glass consisting of ten thousand clusters.

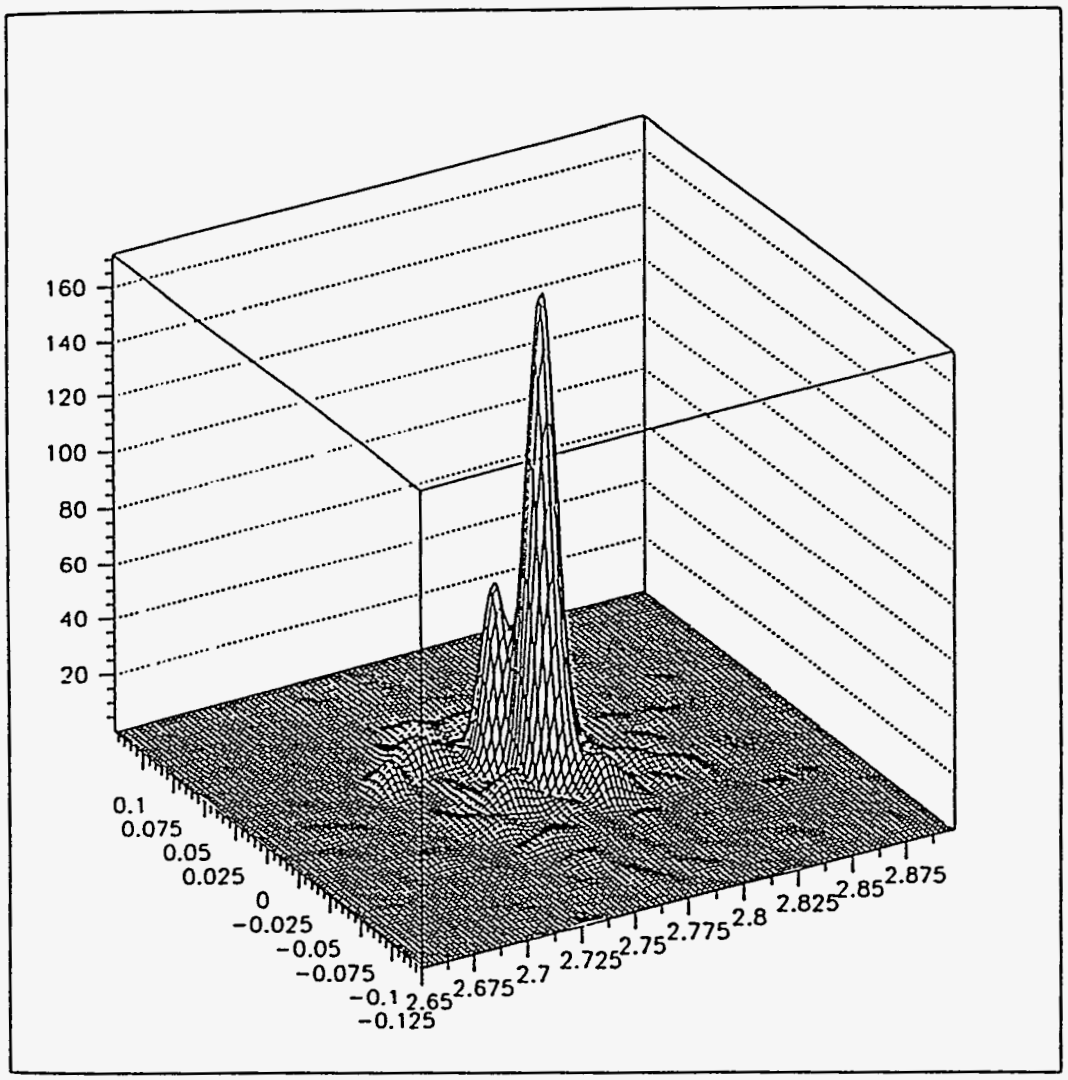

Fig. 3.10. The 20/32 speckle pattern from a computer constructed icosahedral glass consisting of ten thousand clusters.

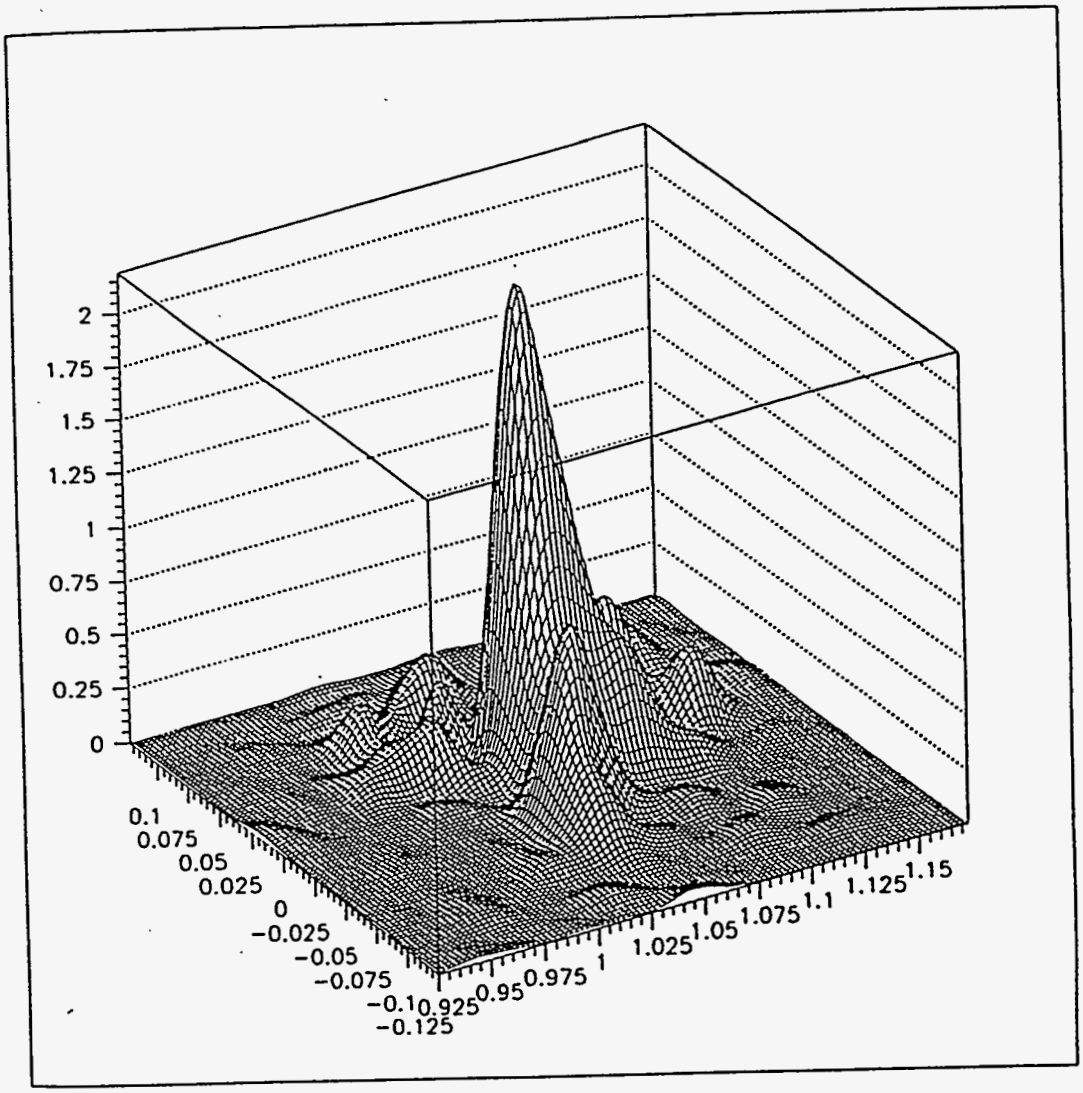

Fig. 3.11. The 4/4 speckle pattern from a computer constructed "Robertson"-icosahedral glass consisting of ten thousand clusters.

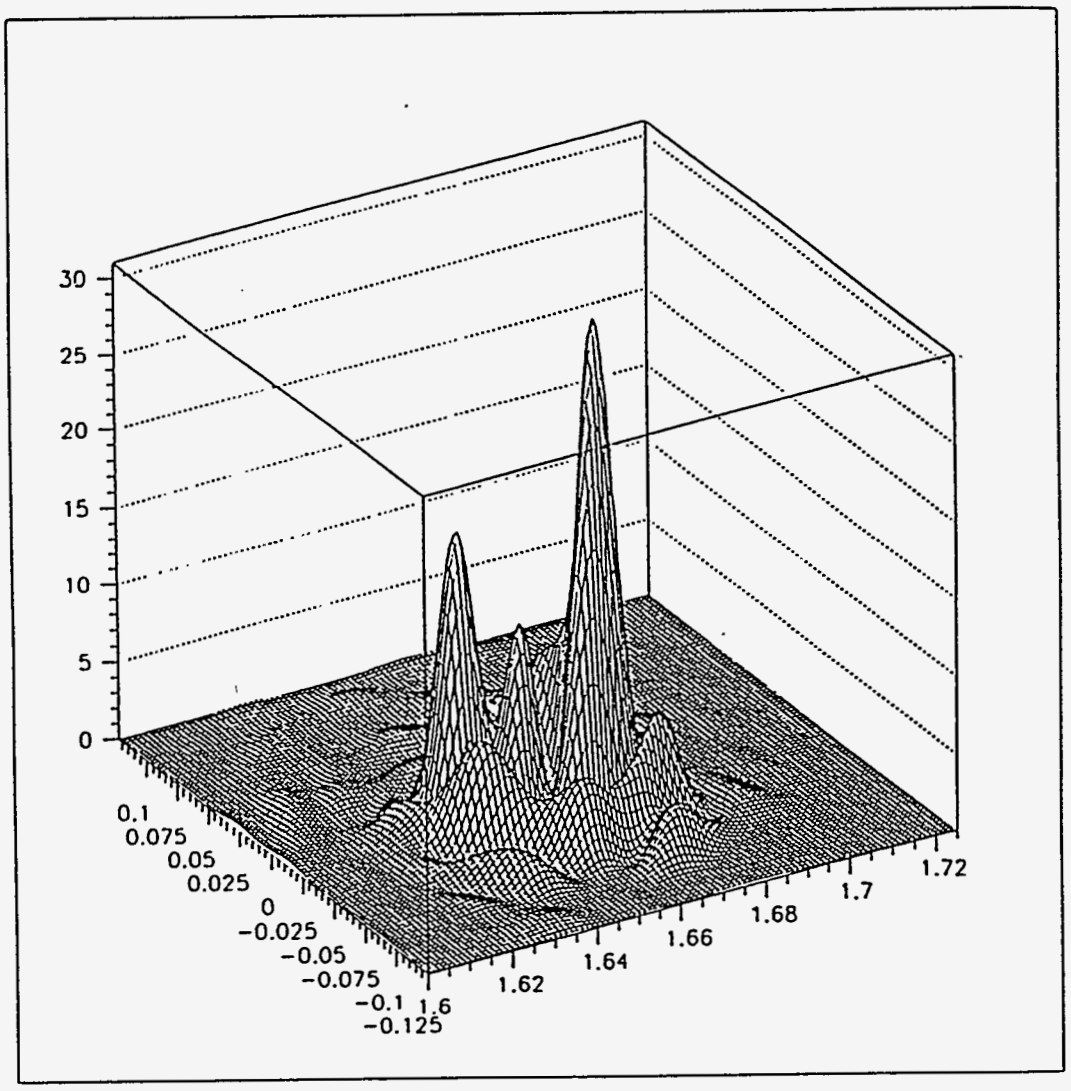

Fig. 3.12. The 8/12 speckle pattern from a computer constructed "Robertson"-icosahedral glass consisting of ten thousand clusters.

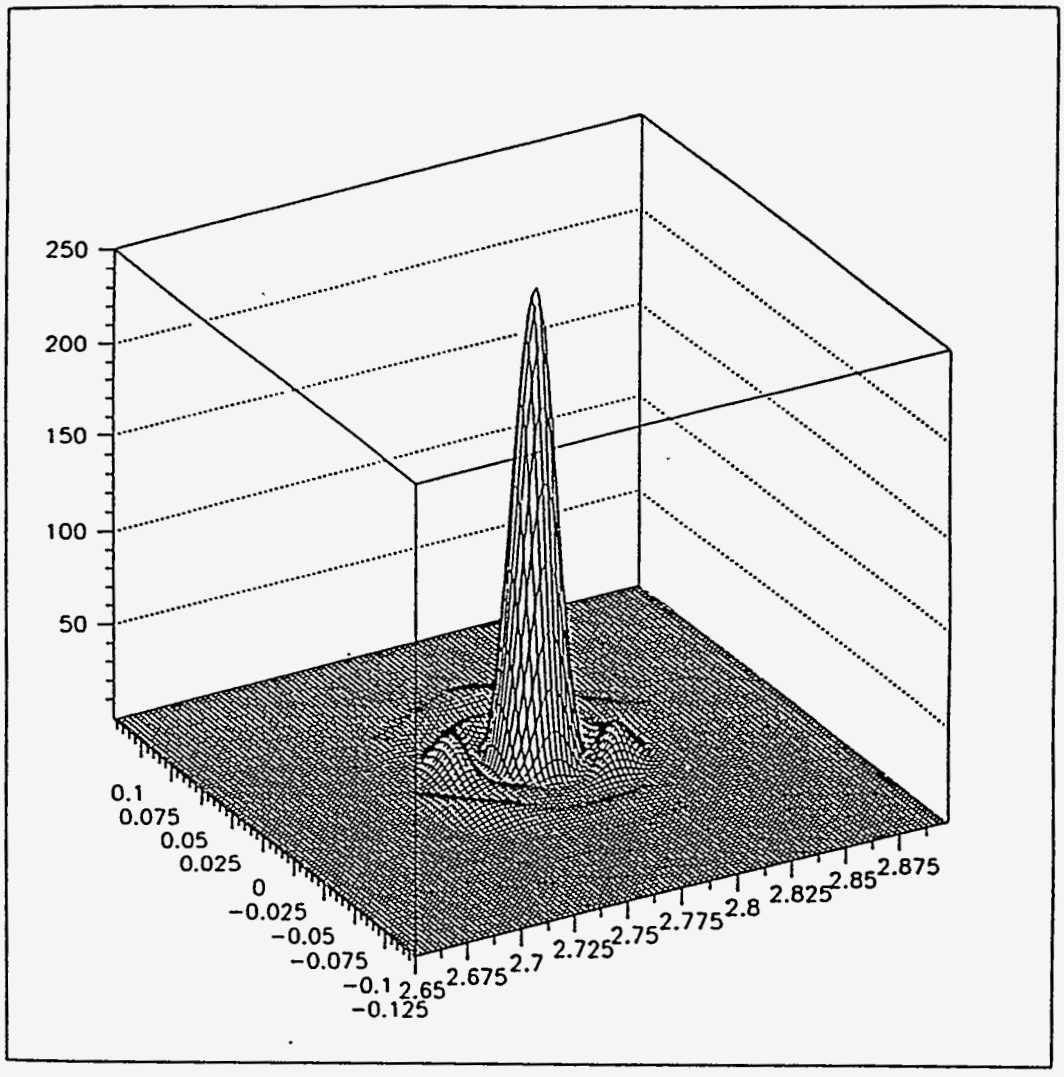

Fig. 3.13. The 20/32 speckle pattern from a computer constructed "Robertson"-icosahedral glass consisting of ten thousand clusters.

and horizontal dimensions of the source are 0.2 mm and 0.4 mm, respectively, and the sample was situated roughly 28 meters from the source, yielding a 25 μm transverse coherence length in the vertical plane, and 12 μm in the horizontal plane. The coherence of the incident beam is demonstrated in Fig. 3.15, which is the

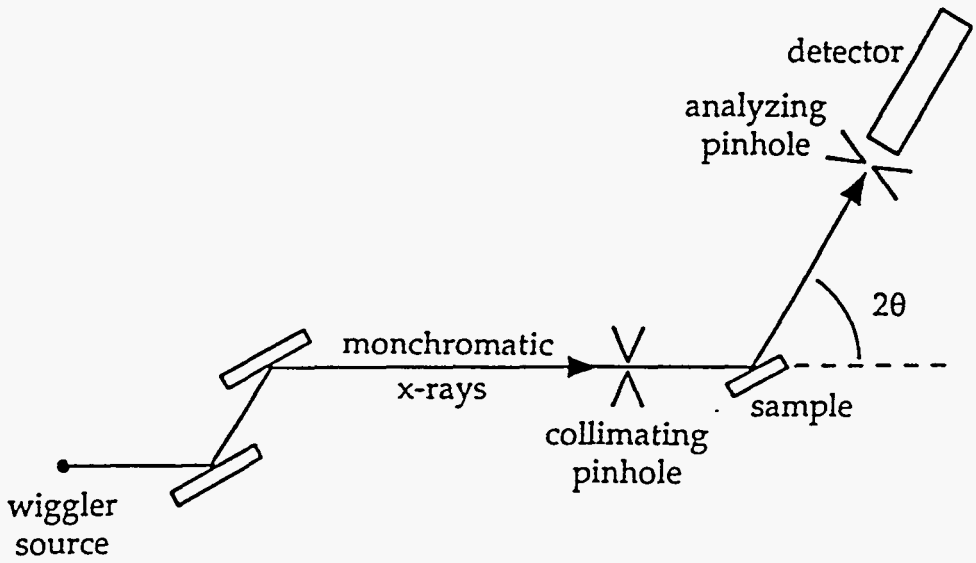

Fig. 3.14. Scattering geometry for coherent x-ray measurements.

Fraunhofer diffraction pattern from a 7 μm circular aperture placed just upstream of the sample position. The structure of the incident beam was measured by translating a 18 μm pinhole across the detector placed on the two-theta arm of the four-circle diffractometer. The solid line represents a fit to the experimental data obtained by convoluting the Fraunhofer pattern from the 7 μm aperture with the 18 μm analyzer pinhole aperture. The observed shape of the central peak and the position of the subsidiary minima and maxima of the measured diffraction pattern agree well with the theoretical calculation, thus showing that the transverse coherence length is at least 7 μm in the vertical and the horizontal directions.

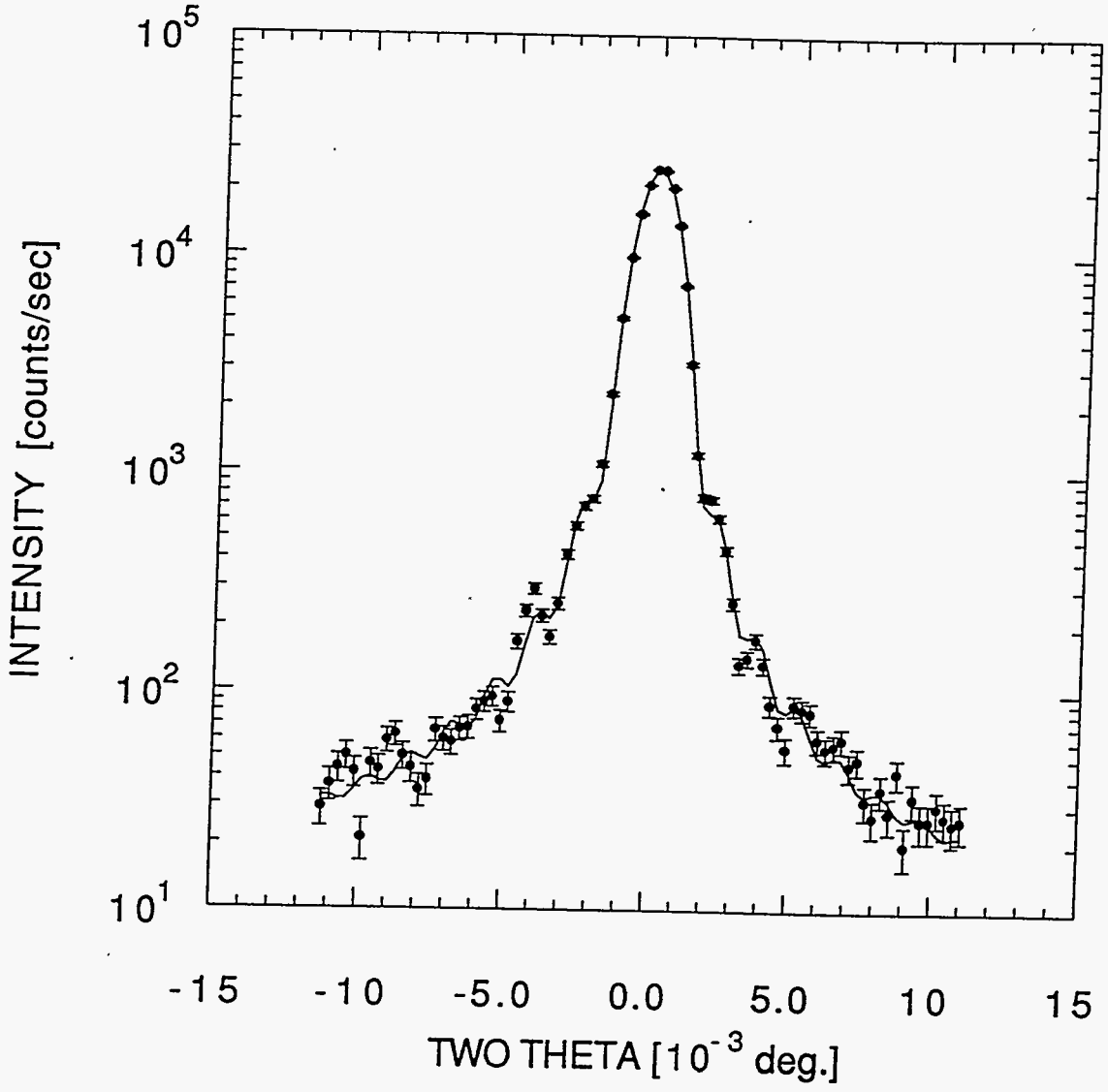

Fig. 3.15. Beam profile after a 7 μm circular pinhile displaying a Fraunhofer pattern.

The icosahedral Al-Pd-Mn sample was mounted at the sample position of the four-circle diffractometer using the 7 μm collimator pinhole before the sample and an 18mm pinhole before the detector. Longitudinal (Q-scans) were made for the (0/2 0/0 0/0), (2/2 0/0 0/0), (2/4 0/0 0/0), and the (4/6 0/0 0/0) peaks along a twofold axis. The observed diffraction peak positions were all within $\Delta q = \pm 0.001 \AA^{-1}$ of the expected values calculated for a FCI quasicrystals with a quasilattice constant of $a_R = 4.563 \AA$. The longitudinal peak widths were all resolution limited. Similarly, transverse scans (q-scan) across several peaks, such as the(2/3 0/0 1/2) shown in Fig. 3.16, yielded resolution limited transverse widths. We point out that the resolution limit of the peak width in the transverse direction is determined by the acceptance of the detector pinhole (approximately 0.001°). These measurements show that over a length scale of several microns, the Al-Pd-Mn quasicrystals is very highly ordered, albeit aperiodic. No evidence of phason strain could be discerned since peak broadening, or speckle using a coherent x-ray probe, was absent in the diffraction pattern.

We continued to study the perfection of the sample by measuring the rocking curve of the sample over a range of points on the sample. This was done by eliminating the detector slits and rocking the sample with respect to the beam. The beam was collimated by a 7 μm circular aperture. The horizontal position of the aperture was scanned over a range of 1 mm in 50 μm increments. After each increment, the rocking curve was measured (Fig. 3.17). The variation of the integrated intensity, the full width at half maximum, as well as position of each curve is small. The significance of these results is that the sample is not only scattering coherently over the 7 μm area, but, in fact, over approximately one millimeter of sample.

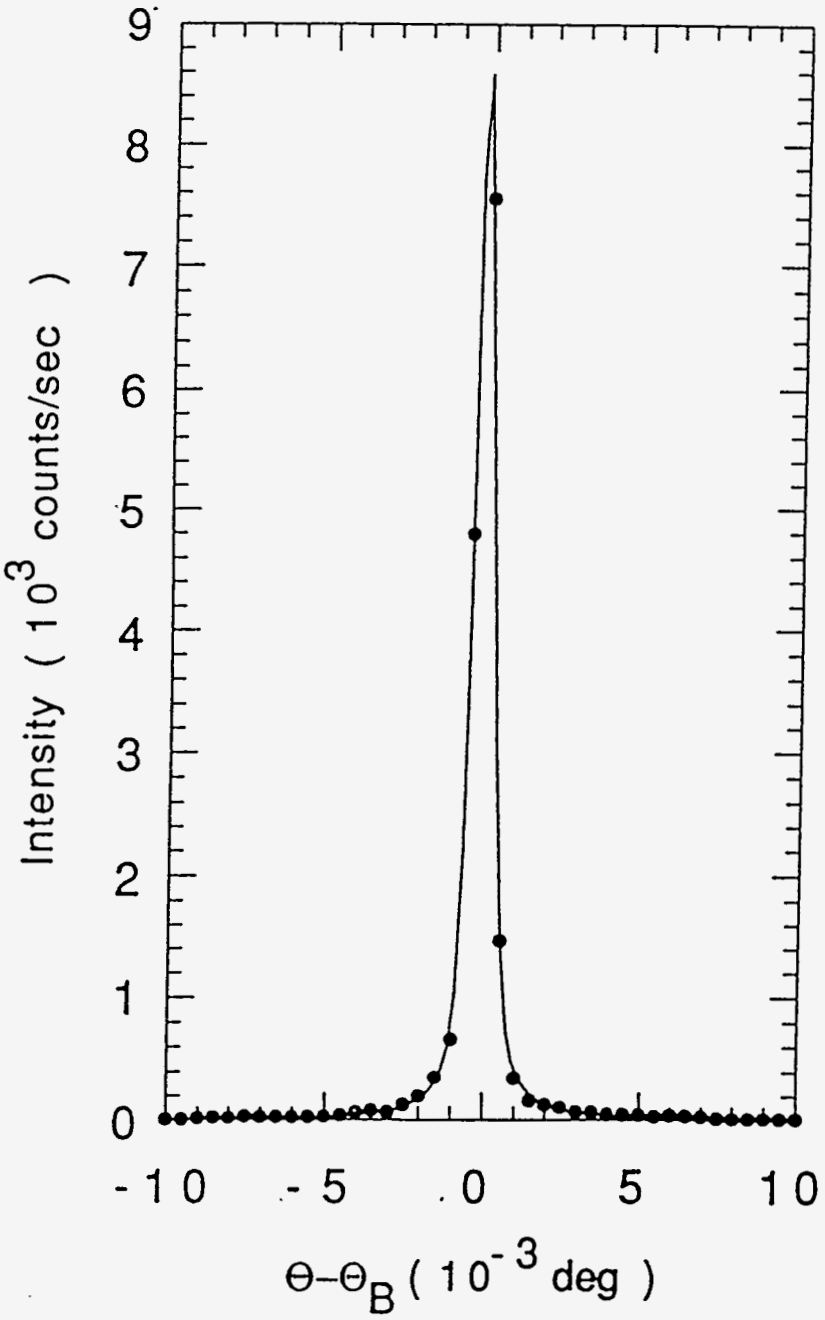

Fig. 3.16. Transverse scan (θ-scan) of the Al-Pd-Mn (2/2 0/0 0/0) peak. The solid line through the data is intended as a guide to the eye.

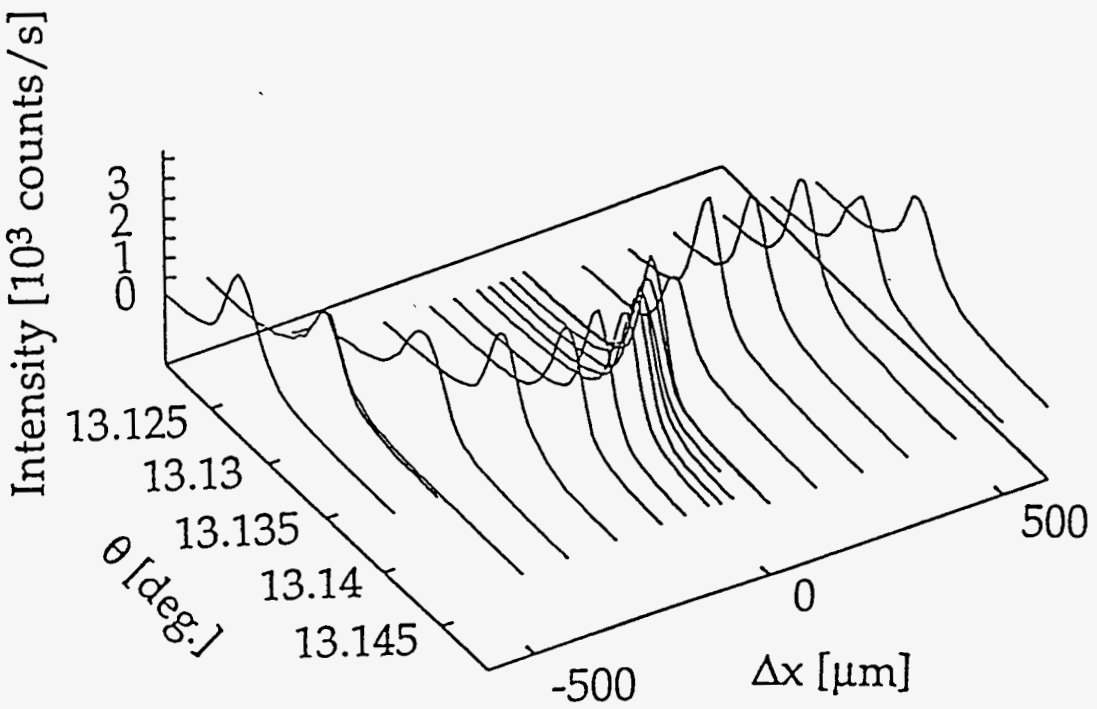

Fig. 3.17. A series of rocking curves of the (2/2 0/0 0/0) reflection as the position of the sample is varied reveal relatively uniform position and intensity of the rocking curves

Conclusion

With present third generation x-ray sources, it is possible to obtain coherent beams of reasonable intensity, thus making x-ray speckle experiments feasible. Although computer simulations demonstrate that x-ray speckle is a sensitive probe for the study of disorder in quasicrystals, results from an experiment on icosahedral Al-Pd-Mn show that the sample exhibited an extraordinarily high degree of order. It will be interesting to perform these measurements on other quasicrystals that are known to produce diffuse peaks. These speckle patterns could then be compared to those produced by the various existing structure models. It would then be interesting to study the intensity fluctuations of the speckle pattern as a function of time.

If the arrangement of the scatterers changes, then the coherent sum of reflected light also changes (the speckle pattern changes). The observation of the intensity fluctuation as a function of time for one point in a speckle pattern provides a direct measure of the time correlation function of the inhomogeneity.[67-68] This leads to a technique called intensity fluctuation spectroscopy, which is a mature field of study using lasers for investigations of temporal fluctuations in liquids, macromolecules in solution, etc. The investigation of the time-dependence of speckle patterns or x-ray intensity fluctuation spectroscopy, is actively being developed as a probe of dynamics in condensed matter systems.[69] Eventually the goal will be to study phason-strain and the time scale of phason fluctuations in condensed matter quasicrystalline systems.

IV. DYNAMICAL THEORY OF X-RAY DIFFRACTION

Introduction

The results of the coherent x-ray scattering measurements indicated that the structural coherence length of the icosahedral Al-Pd-Mn sample is greater than 6 μm. This, in turn, suggested that this alloy might be of sufficient quality to be considered a "perfect" icosahedral quasicrystal. In general, as the defect density decreases and, therefore, the size of the coherent scattering region increases, the kinematical scattering theory fails to be an appropriate description of diffraction from crystalline solids.[70,71] For an accurate description of the diffraction of x-rays from a perfect crystal it is necessary to apply the dynamical theory of x-ray scattering. The dynamical scattering theory, first introduced by P. P. Ewald in 1917 and reformulated by M. von Laue in 1931, has continued to develop through the years.[72] It has been successful in predicting the intensities and angular widths of diffraction peaks, as well as explaining the spectacular phenomenon of anomalous transmission (the Borrmann Effect) and many other phenomena that the kinematical theory of x-ray scattering neglects.

The derivation of the dynamical theory has been presented in many excellent texts and review articles.[73-78] In this chapter, a summary of the derivation of the theory based on these previous works will be discussed, focusing on the aspects that are relevant to the experimental measurements presented in the next chapter. The wave equation will be derived and the boundary conditions will be stated. The two beam approximation will be introduced and the promoted x-ray wavefield inside the crystal will be described. This allows us to explain some interesting phenomena such as the anomalous

transmission of x-rays through the sample at the Bragg angle (the Borrmann Effect). The spherical wave theory, the prediction of Pendellösung interference fringes and the Borrmann Fan will also be described. Finally a discussion of how the dynamical theory of x-ray diffraction applies to quasicrystals is included.

The Dynamical Theory of X-Ray Diffraction

When an x-ray enters a crystal, the electromagnetic wave associated with the photon displaces the electronic distribution with respect to the positively charged ions, inducing some polarization of charge in the crystal. The variation with time of this perturbed electron density leads to the existence of a "Schrödinger" current within the crystal. The propagation of an electromagnetic wavefield in the crystal leads to a dynamic equilibrium between the wavefield and the electrons of the crystal lattice. In order to describe the wavefield it is necessary to obtain the solution of Maxwell's equations in a medium with a periodic dielectric function satisfying the appropriate boundary conditions demanded by the surface of the crystal for the particular case of interest.

Electrodynamics of X-Rays in Condensed Matter Structure

Fundamentally, the problem at hand is one of electrodynamics and thus must be approached by solving Maxwell's equations.

$$(i)\quad \vec{\nabla}\cdot\vec{D}=4\pi\rho \qquad (ii)\quad \vec{\nabla}\cdot\vec{H}=0 \qquad (4\text{-}1)$$

$$(iii)\quad \vec{\nabla}\times\vec{E}=-\frac{1}{c}\frac{\partial\vec{H}}{\partial t} \qquad (iv)\quad \vec{\nabla}\times\vec{H}=\frac{1}{c}\frac{\partial\vec{D}}{\partial t}+\frac{4\pi\vec{J}}{c}$$

The goal is to eventually derive the wave equation for the electric field inside the crystal. Equation (*ii*) allows the magnetic field to be represented in

terms of a vector potential $\vec{A}$, so that $\vec{H} = \vec{\nabla} \cdot \vec{A}$. Equation (*iii*) can then be written as $\vec{\nabla} \times \vec{E} = -\frac{1}{c}\frac{\partial}{\partial t}\left(\vec{\nabla} \times \vec{A}\right)$ thus implying that $\vec{E} = -\frac{1}{c}\frac{\partial \vec{A}}{\partial t} - \vec{\nabla}\phi$, where $\nabla\phi$ is an additive term that can be set to zero (we are working in the Coulomb gauge)

$$\vec{H} = \vec{\nabla} \cdot \vec{A} \tag{4-2}$$

$$\vec{E} = -\frac{1}{c}\frac{\partial \vec{A}}{\partial t}. \tag{4-3}$$

The electromagnetic waves of interest are in the x-ray regime and have periodic time dependence so that the fields can be written

$$\vec{E}(\vec{x},t) = \vec{E}(\vec{x})\exp(-i\omega t) \tag{4-4}$$

$$\vec{H}(\vec{x},t) = \vec{H}(\vec{x})\exp(-i\omega t) \tag{4-5}$$

$$\vec{A}(\vec{x},t) = \vec{A}(\vec{x})\exp(-i\omega t). \tag{4-6}$$

The time derivative is thus equivalent to a multiplicative factor of $-i\omega t$. For example

$$\frac{d\vec{E}(\vec{x},t)}{dt} = -i\omega\vec{E}(\vec{x},t). \tag{4-7}$$

Electric Polarizability and the Dielectric Function

The displacement of the negative charge due to the electromagnetic wave is described by the polarization $\vec{P}$, which is a continuous function of the coordinates. This allows us to define the electromagnetic displacement $\vec{D}$ as

$$\vec{D} = \vec{E} + 4\pi\vec{P} \tag{4-8}$$

provided that the frequency of the external field is far from the natural absorption edge of the system. The lack of free charge in the system means that $\vec{\nabla}\cdot\vec{D}=0$ hence the electric displacement is a transverse field. The conductivity is zero at x-ray frequencies so we can write

$$\vec{D}=\varepsilon\vec{E} \tag{4-9}$$

where ε is the dielectric function. The net current density and the net charge density are equal to zero so the electric polarization can be expressed as

$$\vec{P}=\frac{\chi\vec{E}}{4\pi} \tag{4-10}$$

where χ is the electric polarizability and, from equations (4-8), (4-9) and (4-10), is equivalent to $\varepsilon-1$.

The polarization may be expressed in terms of the electric field since the equation of motion of a free electron in the field $\vec{E}$ is

$$m\frac{d^2\vec{x}}{dt^2}=-e\vec{E}. \tag{4-11}$$

Thus $\vec{x}=-\frac{e}{m\omega^2}\vec{E}$ describes the displacement of an electron due to the electric field. The negative charge displaced from the positive charged nucleus creates an electric dipole that can be represented as a polarization $\vec{P}=-e\vec{x}$. For x-ray energies far removed from absorption edges of the system's atoms, the effects of anomalous scattering and dispersion can be neglected.[73] A continuous negative charge distribution $\rho(\vec{r})$, is assumed to represent the electrons, thus the polarization can be written as

$$\vec{P}(\vec{r})=\rho(\vec{r})\vec{x} \tag{4-12}$$

or

$$\vec{P}(\vec{r}) = -\frac{e^2}{m\omega^2}\rho(\vec{r})\vec{E}(\vec{r}). \tag{4-13}$$

So that the electric polarizability of the crystal can be written

$$\chi(\vec{r}) = -\frac{e^2\lambda^2}{mc^2\pi}\rho(\vec{r}). \tag{4-14}$$

The Wave Equation

It is now possible to proceed to derive the wave equation for the transverse wave of the electric displacement in a medium with an electric polarizability defined as above. Maxwell's equation (*i*), becomes

$$\vec{\nabla}\times\left(\vec{D} - 4\pi\vec{P}\right) = -\frac{1}{c}\frac{\partial\vec{H}}{\partial t} \tag{4-15}$$

taking the curl of this and substituting Maxwell's fourth equation for $\vec{\nabla}\times\vec{H}$ gives

$$\vec{\nabla}\times\vec{\nabla}\times\vec{D} - \vec{\nabla}\times\vec{\nabla}\times 4\pi\vec{P} = -\frac{1}{c^2}\left(\frac{\partial^2\vec{D}}{\partial t^2}\right) \tag{4-16}$$

If we take advantage of the identity, $\vec{\nabla}\times\vec{\nabla}\times\vec{A} = \vec{\nabla}\left(\vec{\nabla}\cdot\vec{A}\right) - \vec{\nabla}^2\vec{A}$, as well as $\vec{\nabla}\cdot\vec{D} = 0$ and $4\pi\vec{P} \cong \chi(\vec{r})\vec{D}(\vec{r})$ the wave equation is obtained:

$$\vec{\nabla}^2\vec{D}(\vec{r}) - \frac{1}{c^2}\frac{\partial^2\vec{D}(\vec{r})}{\partial t^2} + \vec{\nabla}\times\vec{\nabla}\times\left(\chi(\vec{r})\vec{D}(\vec{r})\right) = 0. \tag{4-17}$$

The interaction of the atoms with the x-ray field lies solely in the electric polarizability, as can be seen in the wave equation. Until now we have not considered photoelectric absorption. This can be introduced into the problem by adding an imaginary term to the electric polarizability in the form of a complex

structure factor. Thus the charge distribution can be represented as a Fourier series

$$\rho(\vec{r}) = \frac{1}{V_c}\sum_m F_m \exp\left[-2\pi i\left(\vec{r}\cdot\vec{H}_m\right)\right] \tag{4-18}$$

and the electric polarizability can be written

$$\chi(\vec{r}) = -\frac{e^2\lambda^2}{V_c \pi m c^2}\sum_m F_m \exp\left[-2\pi i\left(\vec{r}\cdot\vec{H}_m\right)\right]. \tag{4-19}$$

Consequently, the complex electric polarizability can be represented as a Fourier series

$$\chi(\vec{r}) = \sum_m \chi_m \exp\left[-2\pi i\left(\vec{r}\cdot\vec{H}_m\right)\right] \tag{4-20}$$

with Fourier coefficient χ_m defined as

$$\chi_m = \int \chi(\vec{r}) \exp\left[2\pi i\left(\vec{r}\cdot\vec{H}_m\right)\right] d\vec{r}. \tag{4-21}$$

It is possible to represent the complex dielectric function as

$$\varepsilon(\vec{r}) = 1 - \frac{e^2\lambda^2}{\pi m c^2}\sum_m F_m \exp\left[-2\pi i\left(\vec{r}\cdot\vec{H}_m\right)\right] \tag{4-22}$$

or

$$\varepsilon(\vec{r}) = \sum_m \varepsilon_m \exp\left[-2\pi i\left(\vec{r}\cdot\vec{H}_m\right)\right]. \tag{4-23}$$

Finally, the wave equation for x-rays in an ordered structure can be written as

$$\vec{\nabla}^2\vec{D}(\vec{r}) - \frac{1}{c^2}\frac{\partial^2\vec{D}(\vec{r})}{\partial t^2} + \vec{\nabla}\times\vec{\nabla}\times\left(\vec{D}(\vec{r})\sum_m \chi_m \exp\left[-2\pi i\left(\vec{r}\cdot\vec{H}_m\right)\right]\right) = 0. \tag{4-24}$$

Lattice Functions and the Solution to the Wave Equation

A convenient term used by M. von Laue when describing dynamical effects in a periodic crystal is the lattice function. The term applies to any function that has the periodicity of the space lattice. Hence the function can be represented by a Fourier series. For example the charge distribution,

$$\rho(\bar{r}) = \frac{1}{V_c}\sum_m F_m \exp\left[-2\pi i\left(\bar{r}\cdot\bar{H}_m\right)\right] \tag{4-25}$$

can be written as a Fourier series with the structure factor as the coefficient of each term. Similarly, the electric polarizability $\chi(\bar{r})$, the dielectric function $\varepsilon(\bar{r})$, and the electric displacement $\bar{D}(\bar{r})$, are just a few of the other quantities that can be considered as lattice functions. Although the charge density can be determined directly through the measurement of the structure factors of the reflections F_m, the coefficients in the summation for the other lattice functions must be derived from $\rho(\bar{r})$.

In the case of the perfect icosahedral quasicrystal, the concept of lattice functions can still be applied. The charge density can be written:

$$\rho(\bar{r}) = \sum_m F_m \exp\left[-2\pi i\left(\bar{r}\cdot\bar{H}_m\right)\right] \tag{4-26}$$

where F_m is the structure factor per unit volume and the reciprocal lattice is defined in equation (1-2) as $\bar{Q} = C^*\left[(h+\tau h')\hat{x} + (k+\tau k')\hat{y} + (l+\tau l')\hat{z}\right]$ with $\bar{Q} = 2\pi\bar{H}$. Therefore, if the charge distribution is represented as a Fourier series, it is possible to derive all the other lattice functions and describe the wave field in the perfect icosahedral quasicrystal.

In general we assume the solution of the wave equation to be of the form:

$$\vec{D}(\vec{r}) = \exp\left[2\pi i\left(\omega t - \vec{k}_0 \cdot \vec{r}\right)\right]\sum_m \vec{D}_m \exp\left[-2\pi i\left(\vec{r} \cdot \vec{H}_m\right)\right] \tag{4-27}$$

so that we can substitute in the expressions for $\chi(\vec{r})$ and $\vec{D}(\vec{r})$ into the wave equation and, with a little work, obtain a solution and a relation for the coefficients $\vec{D}_m$.

$$\vec{D}(\vec{r}) = \exp(2\pi i v t)\sum_m \vec{D}_m \exp\left[-2\pi i\left(\vec{r} \cdot \vec{k}_m\right)\right] \tag{4-28}$$

where $\vec{k}_m = \vec{k}_0 + \vec{H}_m$.

$$\vec{D}_m = \frac{\left|\vec{k}_m\right|^2}{\left|\vec{k}_m\right|^2 - \left|\vec{k}_{ext}\right|^2}\sum_n \chi_{m-n}\vec{D}_{n[m]} \tag{4-29}$$

where, $\vec{D}_{n[m]}$ is the component of $\vec{D}_n$ perpendicular to $\vec{k}_m$. This is considered the fundamental relation of the dynamical theory. For an infinite crystal, the wavefield is described by equation (4-28) which is a Fourier series. Accordingly, the wavefield is composed of an infinite set of wavetrains (one for each reciprocal lattice point) each with a wave vector $\vec{k}_m$. Each term of the series has a coefficient $\vec{D}_m$, proportional to another series (4-29) that is associated with the reciprocal lattice. The coefficients of electric polarizability χ_{m-n}, which ultimately depend on the structure factor, F_{m-n}, couple all the wavetrains together. Consequently, even if the structure factor for a certain reciprocal lattice vector is zero, the amplitude of the corresponding wave train can be non zero. As it stands, determining the exact solution for the wavefield in the crystal is impossible, but if we introduce boundary conditions and make the appropriate assumptions, it is possible, to arrive at approximate solutions that prove to agree very well with experiments.[79-81]

The Reflection Sphere Construction

By way of introduction, it is instructive to review some of the results of the familiar kinematical theory approximation. In particular, the reflection sphere construction (or "Ewald sphere" construction) can be used as a geometric tool to describe kinematical scattering in reciprocal space. The kinematical approximation assumes that the magnitude of the wavevector $|\vec{k}_h|$ inside the crystal is identical to the wavevector in vacuum $|\vec{k}_{ext}| = 1/\lambda$. i.e. $|\vec{k}_o| = |\vec{k}_h| = |\vec{k}_{ext}| = 1/\lambda$, where $\vec{k}_o$ is the refracted wavevector, $\vec{k}_h$ is the reflected wavevector and $\vec{k}_{ext}$ is the external wavevector in vacuum. To first order, this is a reasonable approximation since the index of refraction for x-rays in solids differs little from unity. The construction of the reflection sphere in reciprocal space is presented in Fig. 4.1. One starts by drawing the incident wavevector pointing towards the origin O of reciprocal space. A sphere of reflection of radius $1/\lambda$ is then drawn with its center at the tail of the incident wavevector. If a second reciprocal lattice point labeled H_h in Fig. 4.1 lies exactly on the sphere then, and only then, is the Laue condition satisfied for the corresponding reflection with wavevector $\vec{k}_h = \vec{k}_o + \vec{H}_h$. The point, *La* from which the wavevectors are drawn is called the *Laue Point*. We note in passing that if more than two reciprocal lattice points lie on the sphere of reflection then the crystal is said to be in a multiple scattering condition. Although the reflection sphere construction of the kinematical theory is not appropriate for the dynamical theory it can be used as a guide in determining which approximations may be valid.

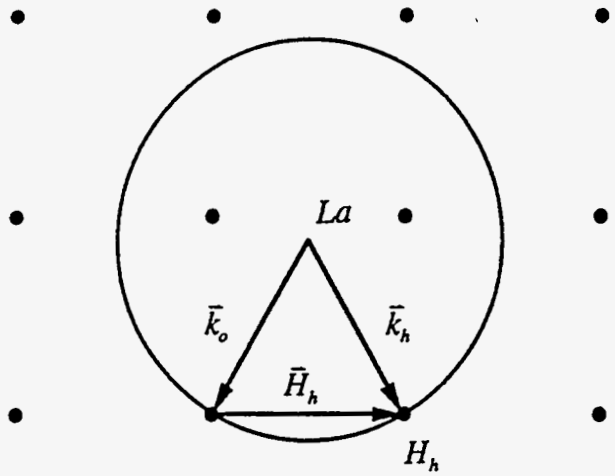

Fig. 4.1. The construction of the reflection sphere or "Ewald Sphere" in reciprocal space describing the scattering of x-rays from a crystal in the kinematical approximation. The incident wavevector $\vec{k}_o$ converges on the origin of reciprocal space. A sphere of radius $1/\lambda$, is drawn with its center at the tail of the incident wavevector. If a second reciprocal lattice point is intersected by the reflection sphere then the corresponding reflection is excited with wavevector $\vec{k}_h$.

Resonance Error

The dynamical theory differs from the kinematical theory in that it accounts for the small deviations of the wavevectors within the crystal resulting from the crystal's anisotropic dielectric function. It is convenient to introduce a parameter e_m, first introduced by Ewald who called it the "resonance error."[3,4] This parameter is a measure of the deviation of the magnitude of a

wavevector $|\vec{k}_m|$ of a constituent wavetrain from the magnitude of the wavevector in vacuum $|\vec{k}_{ext}|$ and is defined as

$$e_m = \frac{|\vec{k}_m| - |\vec{k}_{ext}|}{|\vec{k}_{ext}|}. \tag{4-30}$$

The wavefield is composed of terms describing an infinite number of reciprocal lattice points, but only those terms described by reciprocal vectors near the Ewald sphere contribute effectively to the scattering.

If $|\vec{k}_m| \approx |\vec{k}_{ext}|$ then $e_m << 1$.

For these reflections,

$$\frac{|\vec{k}_m|^2 - |\vec{k}_{ext}|^2}{|\vec{k}_m|^2} \approx 2e_m \tag{4-32}$$

and the fundamental equation (4-29) can be written as

$$\vec{D}_m = \frac{1}{2e_m} \sum_m \chi_{m-n} \vec{D}_{n[m]}. \tag{4-33}$$

Examples:

Silicon:

$$e_o = -\frac{e^2\lambda^2}{2\pi mc^2} \frac{1}{V} \sum_a n_a Z_a \tag{4-34}$$

for $CuK\alpha$ radiation:

λ=1.54Å

Z=14

n=8

$$\frac{e^2}{mc^2} = 2.817 \times 10^{-5}\,\text{Å}$$

$$V = (5.431\text{Å})^3$$

therefore $e_o = -7.4 \times 10^{-6}$.

$Al_{70}Pd_{20}Mn_{10}$ for $CuK\alpha$ radiation:

$$e_o = -\frac{e^2\lambda^2}{2\pi mc^2}\rho_{Al-Pd-Mn}\frac{\sum_a x_a Z_a}{\sum_a w_a} \qquad (4\text{-}35)$$

$$\rho_{Al-Pd-Mn} = 5.2 grams/cm^3$$

$$\rho_{Al-Pd-Mn}\frac{\sum_a x_a Z_a}{\sum_a w_a} = 1.4558\ electrons/\text{Å}^3$$

therefore $e_o = -1.539 \times 10^{-5}$.

We see that while the kinematical theory predicts that reflections occur only for those reciprocal lattice points on the reflection sphere, the dynamical theory relaxes the condition, requiring that the reciprocal lattice point be within the resonance error of the reflection sphere. The resonance error associated with the origin of reciprocal space e_o, can be intuitively viewed as introducing a thickness to the sphere of reflection of the kinematical approximation.

The Single Wave Approximation

In the dynamical theory, the case of only one reciprocal lattice point (the origin) near the sphere of reflection is called the single wave approximation. Consequently, the summation in the definition of the wavefield (4-28) has only one significant term so that

$$\frac{\left|\vec{k}_o\right|^2 - \left|\vec{k}_{ext}\right|^2}{\left|\vec{k}_{ext}\right|^2}\vec{E}_o = \chi_o \vec{E}_o. \tag{4-36}$$

This has the solution

$$\left|\vec{k}_o\right| = \left|\vec{k}_{ext}\right|\sqrt{1+\chi_o}. \tag{4-37}$$

Since $\chi_o << 1$ we can write

$$\left|\vec{k}_o\right| \approx \left|\vec{k}_{ext}\right|\left(1+\frac{\chi_o}{2}\right). \tag{4-38}$$

If we imagine, in reciprocal space, the set of wavevectors $\vec{k}_o$ that satisfy this condition, positioned so as to converge at the origin, and then draw the set of points that correspond to the set of allowed starting points for these vectors, we obtain a sphere S_o about the origin. This sphere is called the *dispersion surface* and is shown in Fig. 4.2. The dispersion surface represents the set of allowed wavevectors which satisfy Maxwell's equations within the crystal. The difference in radius between the spheres of radius $\left|\vec{k}_{ext}\right|$ and $\left|\vec{k}_o\right|$ is exaggerated for, in reality, the difference in radius is on the order of one part in 10^5. One should also note that the electric polarizability is a complex value, but since absorption is relatively small when $\left|\vec{k}_{ext}\right|$ is far from an absorption edge

of the crystal, it is common to draw the dispersion surface in a real reciprocal space. The real part of $(1+\chi_o/2)$ corresponds to the isotropic index of refraction and the imaginary part corresponds to the isotropic absorption coefficient.

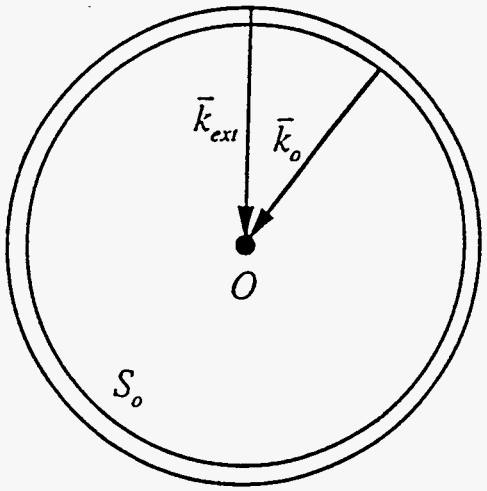

Fig. 4.2. The dispersion surface for the single wave approximation consists of a sphere S_o drawn about the origin of reciprocal space.

The Two Wave Approximation

If the crystal is rotated with respect to the incident x-ray so that a second reciprocal lattice point H_h approaches the sphere of reflection, the resonance error e_h becomes comparable to e_o and, accordingly, the contributions of both reciprocal lattice points become significant. Taking into account the

contributions of both reciprocal lattice points in (4-29) leads to the two-beam or two-wave approximation. The fundamental relation simplifies to two vector equations

$$\vec{D}_o = \frac{\left|\vec{k}_o\right|^2}{\left|\vec{k}_o\right|^2 - \left|\vec{k}_{ext}\right|^2}\left(\chi_o \vec{D}_{o[o]} + \chi_{\bar{h}} \vec{D}_{h[o]}\right) \tag{4-39}$$

$$\vec{D}_o = \frac{\left|\vec{k}_o\right|^2}{\left|\vec{k}_o\right|^2 - \left|\vec{k}_{ext}\right|^2}\left(\chi_o \vec{D}_{o[o]} + \chi_{\bar{h}} \vec{D}_{h[o]}\right) \tag{4-40}$$

Each vector can be decomposed into two components:

$$\vec{D}_o = \vec{D}_o^{\sigma} + \vec{D}_o^{\pi},\ \vec{D}_h = \vec{D}_h^{\sigma} + \vec{D}_h^{\pi} \tag{4-41}$$

where $\vec{D}_o^{\sigma}$ and $\vec{D}_h^{\sigma}$ are defined as the components normal to the plane passing through the wavevectors $\vec{k}_o$ and $\vec{k}_h$ of the two plane waves. This plane is commonly called the *plane of reflection* shown in Fig. 4.3. The components $\vec{D}_o^{\pi}$ and $\vec{D}_h^{\pi}$ are directed along $\hat{D}_o^{\pi} = \hat{k} \times \hat{D}_o^{\sigma}$ and $\hat{D}_h^{\pi} = \hat{k} \times \hat{D}_h^{\sigma}$ respectively. Thus $\vec{D}_o^{\sigma}$ and $\vec{D}_h^{\sigma}$ are parallel, while $\vec{D}_o^{\pi}$ and $\vec{D}_h^{\pi}$ are rotated by an angle 2θ with respect to each other.

The σ component equations are

$$(\chi_o - 2e_o)D_o^{\sigma} + \chi_{\bar{h}} D_h^{\sigma} = 0 \tag{4-42}$$

$$\chi_o D_o^{\sigma} - (\chi_o - 2e_h)D_h^{\sigma} = 0 \tag{4-43}$$

and the π component equations are

$$(\chi_o - 2e_o)D_o^{\pi} + \cos(2\theta)\chi_{\bar{h}} D_h^{\pi} \tag{4-44}$$

$$\cos(2\theta)\chi_o D_o^{\pi} - (\chi_o - 2e_h)D_h^{\pi} = 0. \tag{4-45}$$

The condition implied by these equations can be written

$$(\chi_o - 2e_o)(\chi_o - 2e_h) = C^2\chi_h\chi_{\bar{h}} = C^2|\chi_h|^2, \tag{4-46}$$

where $C = 0$ for the σ component and $C = \cos 2\theta$ for the π component. The significance of this equation is that it defines a direct relationship between the

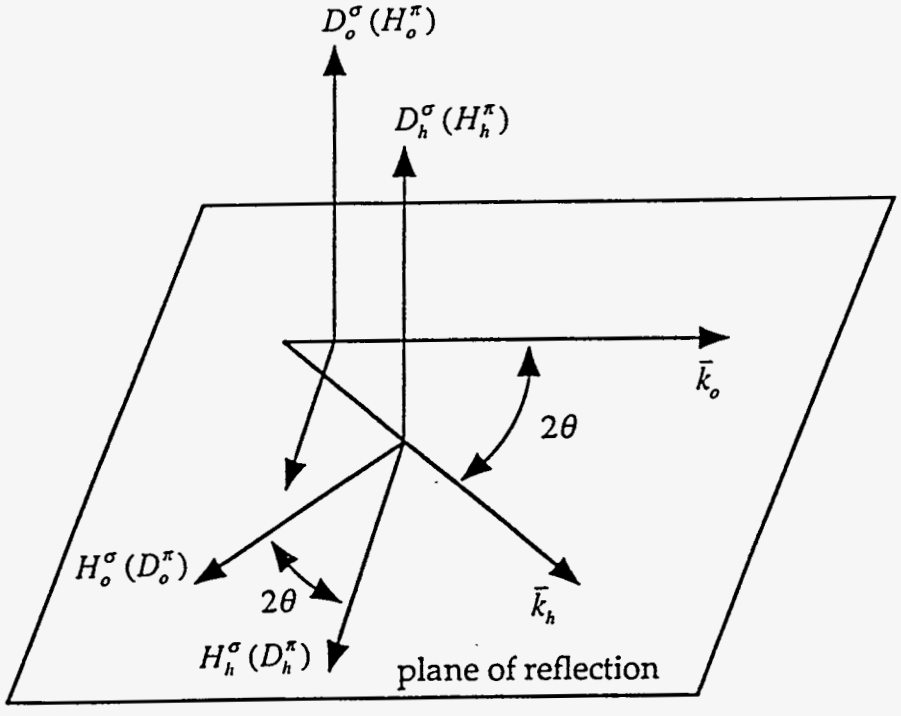

Fig. 4.3. The plane of reflection and the components of the field vectors of the $\sigma(\pi)$ state of polarization. The σ components of the electric displacement $\bar{D}_o^{\sigma}$ and $\bar{D}_h^{\sigma}$ are normal to the plane of reflection and are mutually parallel. The π components of the electric displacement $\bar{D}_o^{\pi}$ and $\bar{D}_h^{\pi}$ lie in the plane of reflection but are misaligned by an angle of 2θ with respect to each other.

resonance errors e_o and e_h. The wavevectors of the plane wave constituents of the wave field are define by $|\vec{k}_o| = |\vec{k}_{ext}|(1+e_o)$ and $|\vec{k}_h| = |\vec{k}_{ext}|(1+e_h)$. Consequently, equation (4-46) represents a relationship between the two wavevectors. The relationship can be illustrated by the construction of the dispersion surface which is the locus of allowed pairs of wavevectors $\vec{k}_o$ and $\vec{k}_h$. Shown in Fig. 4.4 is a region of reciprocal space near the Laue Point *La* displaying a portion of the dispersion surface. Due to the scale of the drawing, the circles S_{ext} and S'_{ext} of radius $|\vec{k}_{ext}|$ centered around the *O* and H_h appear as straight (dashed) lines. In addition the circle S_o of radius $|\vec{k}_o|$ centered about *O* and the circle S_h of radius $|\vec{k}_h|$ centered about H_h will also appear as straight lines. Although S_o and S_h are dispersion surfaces in the case of the single wave approximation, the dispersion surface for the two-wave approximation is slightly shifted from these spheres. The largest shifts are in the region nearest the Lorentz Point *Lo* as shown in Fig. 4.4. A pair of wavevectors $\vec{k}_o$ and $\vec{k}_h$ satisfying equation (4-46) is drawn from a point *P* on the dispersion surface to the reciprocal lattice points O and H_h respectively. The point *P* is called a tie point (or excitation point). The significance of the dispersion surface is now apparant. It is the locus of solutions of equation (4-46) which is the result of applying a two-beam approximation to the fundamental equation (4-29). A better understanding of the shape of the dispersion surface can be attained by introducing two parameters ξ_o and ξ_h (Fig. 4.5) which are defined as the perpendicular distances from *P* to S_o and *P* to S_h respectively, so that

$$\xi_o = |\vec{k}_{ext}|(1+e_o) - |\vec{k}_{ext}|(1+\tfrac{1}{2}\chi_o) \tag{4-47}$$

$$\xi_h = |\vec{k}_{ext}|(1+e_h) - |\vec{k}_{ext}|(1+\tfrac{1}{2}\chi_o). \tag{4-48}$$

This allows equation (4-46) to be written

$$\xi_o \xi_h = \frac{|\vec{k}_{ext}|^2}{4} C^2 |\chi_h|^2. \tag{4-49}$$

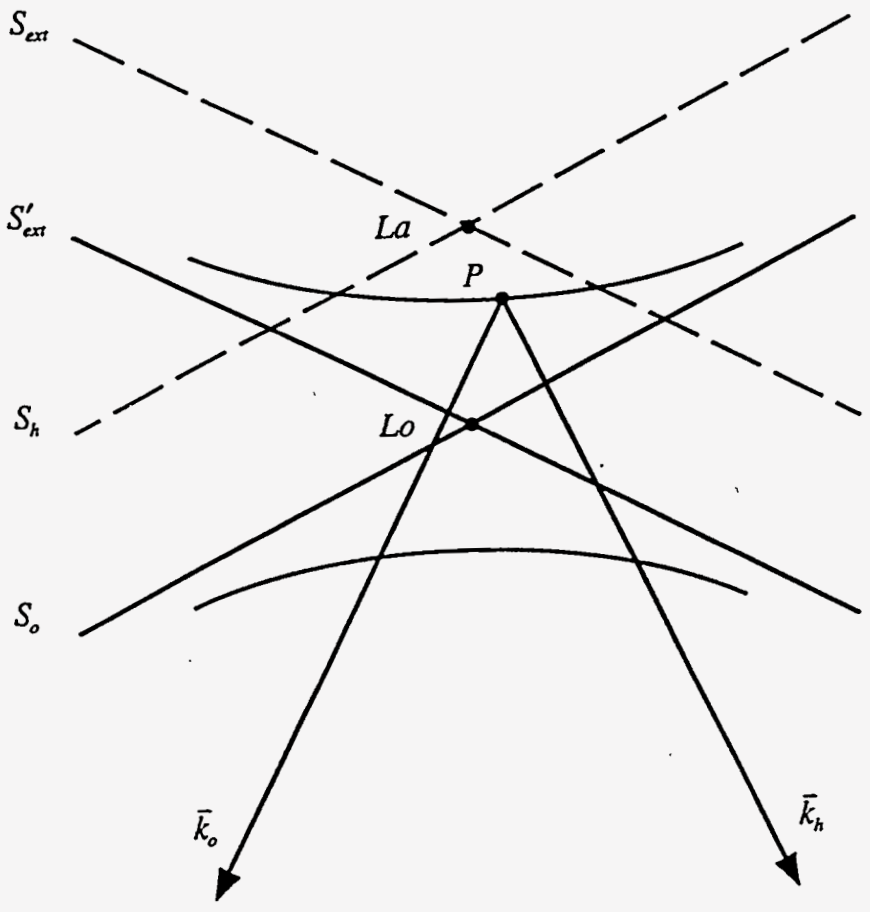

Fig. 4.4. A portion of the dispersion surface in the visinity of the Laue Point *La*. Because of the scale of the drawing, the spheres S_o, S_h, S_{ext} and S'_{ext} appear as straight lines. The point of intersection of S_{ext} and S'_{ext} is the Laue Point *La* and the point of intersection of S_o and S_h is called the Lorentz point *Lo*. A pair of wavevectors $\vec{k}_o$ and $\vec{k}_h$ satisfying the fundamental equation of the dynamical theory are drawn from a point on the dispersion surface *P* (called a tie point) and converge on the reciprocal lattice points *O* and H_h respectively.

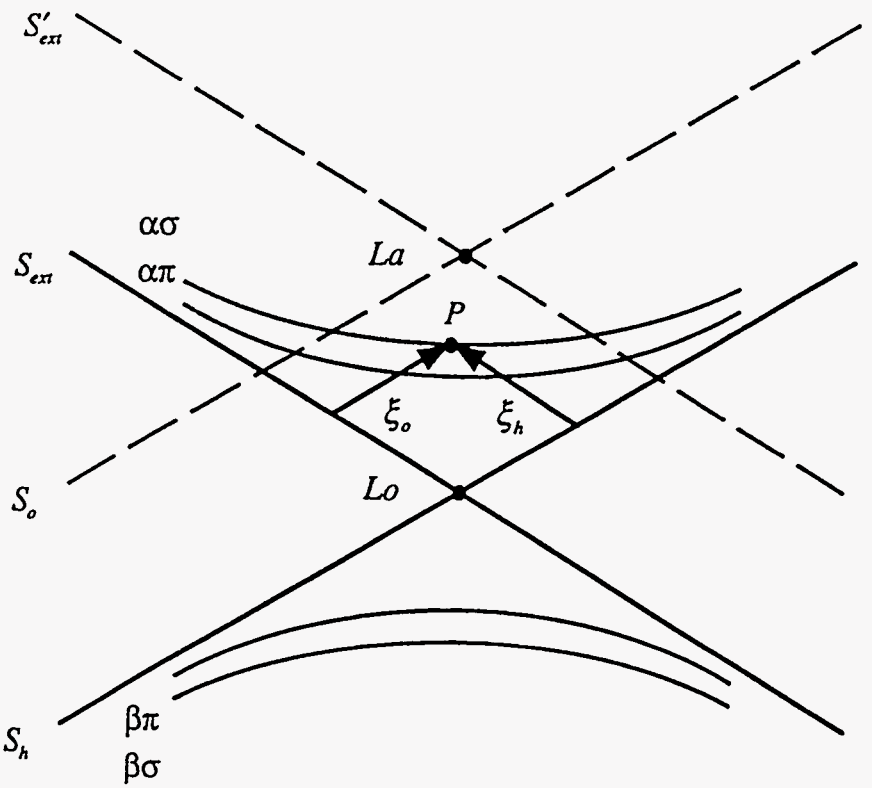

Fig. 4.5. The dispersion surface in the case of the two-beam approximation consists of four branches as shown in the figure. Far from the Lorentz point, the dispersion surface asymptotically approaches the spheres of the single wave case.

Equation (4-49) defines the dispersion surface for the two-wave case. In the plane of the drawing, the dispersion surface appears as a pair of hyperbola with the lines S_o and S_h as asymptotes. Due to polarization of the electric displacement $\bar{D}$, C will either be equal to 1 or $\cos 2\theta$. Because $\cos 2\theta$ is always less than one, this implies that the hyperbola of the π dispersion surface (called the π-branch) is always closer to the Lorentz point Lo than the σ-branch. In order to obtain the surface in three dimensions it is necessary to rotate this hyperbola about the axis defined by the vector $\bar{H}_h$. This forms a hyperbolic cylinder with axis parallel to

the vector $\vec{H}_h$, centered about the origin with its narrowest diameter on the plane perpendicularly bisecting the line segment OH_h.

The dispersion surface consists of four branches $\{\sigma\alpha,\ \sigma\beta,\ \pi\alpha,\ \pi\beta\}$ as shown in Fig. 4.5. Any wave propogating in the crystal must be composed of terms with wavevectors drawn from points on the dispersion surface and converging on either O or H_h.

The equation of the wave field can be written

$$\vec{D}(\vec{r},t) = \exp(2\pi i \upsilon t)\left[\vec{D}_o \exp\left(-2\pi i \vec{k}_o \cdot \vec{r}\right) + \vec{D}_h \exp\left(-2\pi i \vec{k}_h \cdot \vec{r}\right)\right] \tag{4-50}$$

and a relationship between the amplitudes $\vec{D}_o$ and $\vec{D}_h$ can be determined from equations (4-42 to 4-45, 4-50) and the amplitude ratio R can be written

$$R = \frac{|\vec{D}_h|}{|\vec{D}_o|} = \frac{C|\vec{k}_{ext}|\chi_h}{2\xi_h}. \tag{4-51}$$

Hence the dispersion surface not only allows the determination of the wavevectors from the position of the tie point, but also the amplitudes.

Boundary Conditions

Relation (4-28) defines the allowed wavevectors for the propagating wavefield inside the crystal and allows the description of the dispersion surface. But what has not yet been explained is the relationship between the external incident beam and the wavefield inside the crystal. In other words, how does one determine which tie points are excited. In order to describe the wavefield it is necessary to invoke the familiar boundary conditions that are imposed on electromagnetic waves. This applies constraints on the frequency, amplitude and wavevector. The continuity of the frequency simply implies that the boundary

has no effect on the frequency of the wave as it passes through the boundary. The continuity of the wavevector at the surface of the crystal implies that the tangential component of the wavevector must be equal on either side of the boundary since the wave fields on either side of the boundary must have equal phase velocities tangent to the surface.

The boundary condition on the amplitude requires that the amplitude of the electric displacement be continuous at the surface. Thus

$$\vec{D}_{ext} = \vec{D}_{o\alpha} + \vec{D}_{o\beta} \tag{4-52}$$

$$0 = \vec{D}_{h\alpha} + \vec{D}_{h\beta} \text{ , for all } h. \tag{4-53}$$

The Single Wave Approximation

In the case of the single wave approximation, we draw the dispersion surface inside the crystal S_o as the sphere of radius $|\vec{k}_o|$. Outside the crystal the dispersion surface is the sphere of radius $|\vec{k}_{ext}|$. In addition the surface normal $\hat{n}$ is drawn in the direction facing into the crystal as shown in Fig. 4.6. The incident beam wavevector in vacuum $\vec{k}_{ext}$ is drawn from a tie point on the sphere S_{ext}. To determine which tie point is excited on the internal dispersion surface it is necessary to draw a line parallel to the surface normal and through the point Q. The line intersecting the dispersion surface at P. This is the tie point (or excitation point) that corresponds to the excited wave field in the crystal that satisfies the boundary conditions. This graphic description is analogous to *Snell's Law* of optics and defines the refraction of x-rays due to the crystal surface.

The Double Wave Approximation

In the case of the two wave approximation, the dispersion surface near the Laue Point is composed of two cylindrical hyperboloids. The construction of the boundary conditions is done as for the single wave case. If we assume a transmission (Laue) geometry the surface normal is drawn into the crystal and the dispersion surface is drawn as in Fig. 4.7. The wavevector $\vec{k}_{ext}$ is drawn from

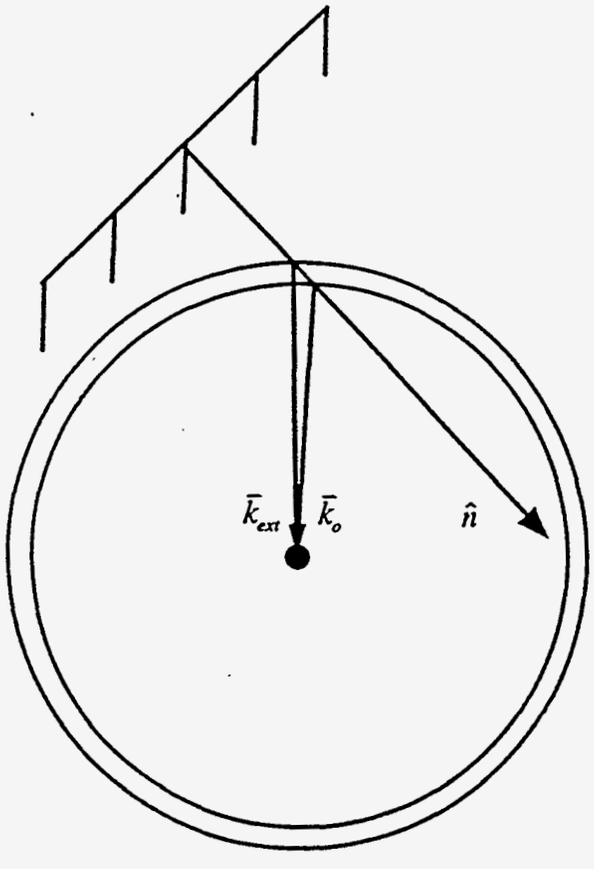

Fig. 4.6. The boundary conditions in the case of a single wave case can be graphically displayed. Shown is the surface normal $\hat{n}$, the incident wavevector $\vec{k}_{ext}$, the resulting exitation point P and the corresponding internal wave vector $\vec{k}_o$.

a tie point on the external dispersion surface S_{ext}. If the crystal is set at the Bragg angle then this tie point corresponds to the Laue Point *La*. A line parallel to the surface normal is drawn through *La* and intersects the dispersion surface at four tie points P_1, P_2, P_3, and P_4 (Fig. 4.7) thus exciting four waves in the crystal.

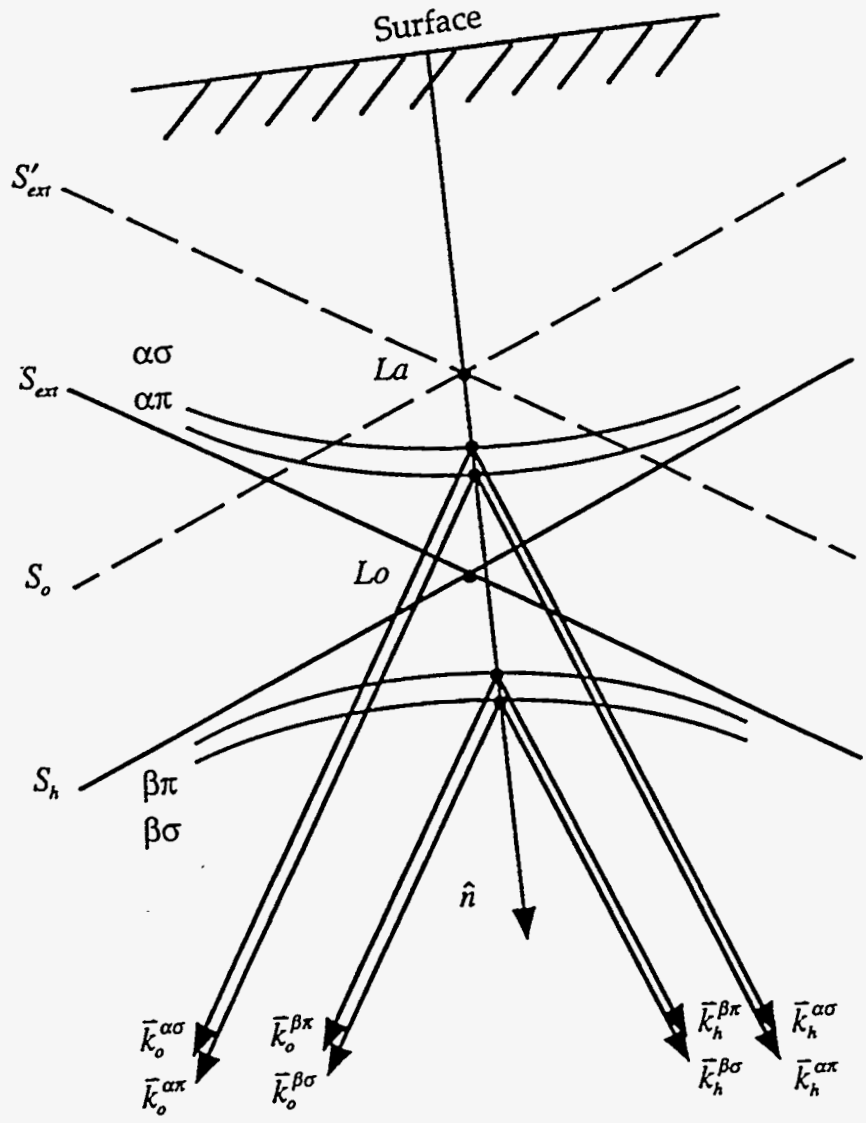

Fig. 4.7. The boundary condition in the case of a Laue transmission geometry selects four tie points on the dispersion surface.

Energy Flow

Assume a crystal to be set in the symmetric Laue geometry as shown in (Fig. 4.8). The Pointing vector gives the direction of energy flow in the crystal and is defined as

$$\vec{S} = \frac{c}{4\pi}\left(\vec{E} \times \vec{H}\right) \tag{4-54}$$

But

$$\vec{H} = \frac{i\omega}{c}\left(\vec{k} \times \vec{E}\right) \tag{4-55}$$

so that for the two beam approximation

$$\vec{S} \propto \left(I_o \hat{k}_o + I_h \hat{k}_h\right) \tag{4-56}$$

where I_o and I_h are the intensities of the refracted and diffracted waves respectively. The Pointing vector can be decomposed into two components S_x and S_z where $\hat{x}$ and $\hat{z}$ are defined in Fig. 4.8. We introduce a new parameter Δ, which is the angle between the propagation direction of the wavefield and the Bragg planes. The components of the Pointing vector can then be written

$$\vec{S} \cdot \hat{x} = \left|\vec{S}\right| \sin\Delta \propto I_o \hat{k}_o \cdot \hat{x} + I_h \hat{k}_h \cdot \hat{x} = \left(I_h - I_o\right) \sin\theta_B \tag{4-57}$$

$$\vec{S} \cdot \hat{z} = \left|\vec{S}\right| \cos\Delta \propto I_o \hat{k}_o \cdot \hat{z} + I_h \hat{k}_h \cdot \hat{z} = \left(I_h + I_o\right) \cos\theta_B. \tag{4-58}$$

Forming the ratio of the two equations leads to

$$\tan\Delta = \left(\frac{I_h - I_o}{I_h + I_o}\right) \tan\theta_B = \left(\frac{R^2 - 1}{R^2 + 1}\right) \tan\theta_B. \tag{4-59}$$

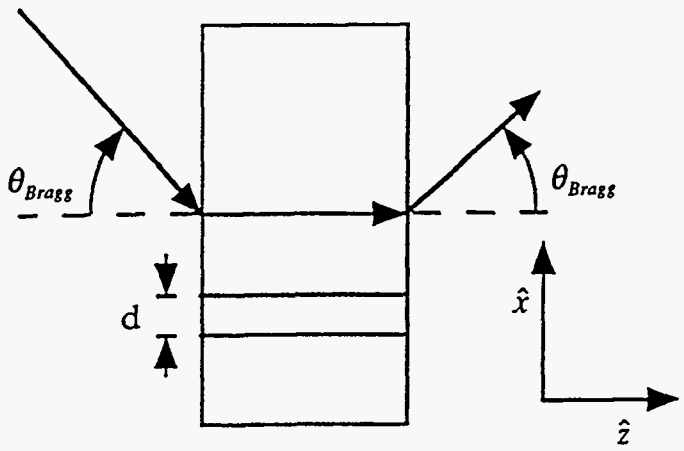

Fig. 4.8. Depiction of the Laue scattering geometry and the defined coordinate system.

This is a relation between the direction of propagation and the amplitude ratio R. Further calculations lead to a relation between the tie point on the dispersion surface and the direction of propagation $\vec{S}$ in the crystal. The result is that the Pointing vector for a wavefield is perpendicular to the dispersion surface at the associated tie point. This leads to an important effect called the "Borrmann Fan". In the case where the tie point is at the diameter point of the dispersion surface, then $R=1$ and $\tan\Delta=0$ so that the Pointing vector is directed along the Bragg planes as shown in Fig. 4.9a. If the incident beam angle is slightly misaligned from the Bragg angle, for example Fig. 4.9b, it is seen that two waves are promoted that propagate in different directions (in other words the beam splits into an α-beam and a β-beam). If the crystal is misaligned by the same amount in opposite directions, then the beam, again, splits in two but as

can be seen in Fig. 4.9c, now the β branch and the α branch are switched from the second case.

Therefore as a crystal is rocked through the Bragg angle with respect to an incident x-ray plane wave which is monochromatic and spacially well defined, the excitation point can be imagined to move along the dispersion surface. The resultant wavefield will vary in intensity as defined by the rocking curve for the reflection and will vary in direction as determined by the propagation angle which varies in the range $-\theta_B$ and θ_B. This means that a triangle can be drawn that encompasses any possible wavefield in the crystal (Fig. 4.10).

The Borrmann Effect

We consider the case of a x-ray beam represented by a monochromatic plane wave incident on a sample that is oriented in the symmetric Laue reflection geometry (Fig. 4.8). For convenience let us assume that the incident beam is polarized so as only to contain the D_σ component. The π dispersion surfaces can then be ignored and only two tie points on two dispersion surfaces are excited. We have shown that, in general, the x-rays in the crystal must be consistent with the dispersion surface defined by equation (4-29). But if only one reciprocal lattice point (other than the origin of reciprocal space) is near the sphere of reflection then it may be appropriate to make the two beam approximation. The dispersion surface, as defined by equation (4-49), was a pair of hyperboloids (with points of narrowest diameter on the plane perpendicularly bisecting the line segment OH_h) that asymptotically approach the spheres S_o and S_h away from the Laue point.

The boundary conditions for the case of a sample in the shape of a parallel

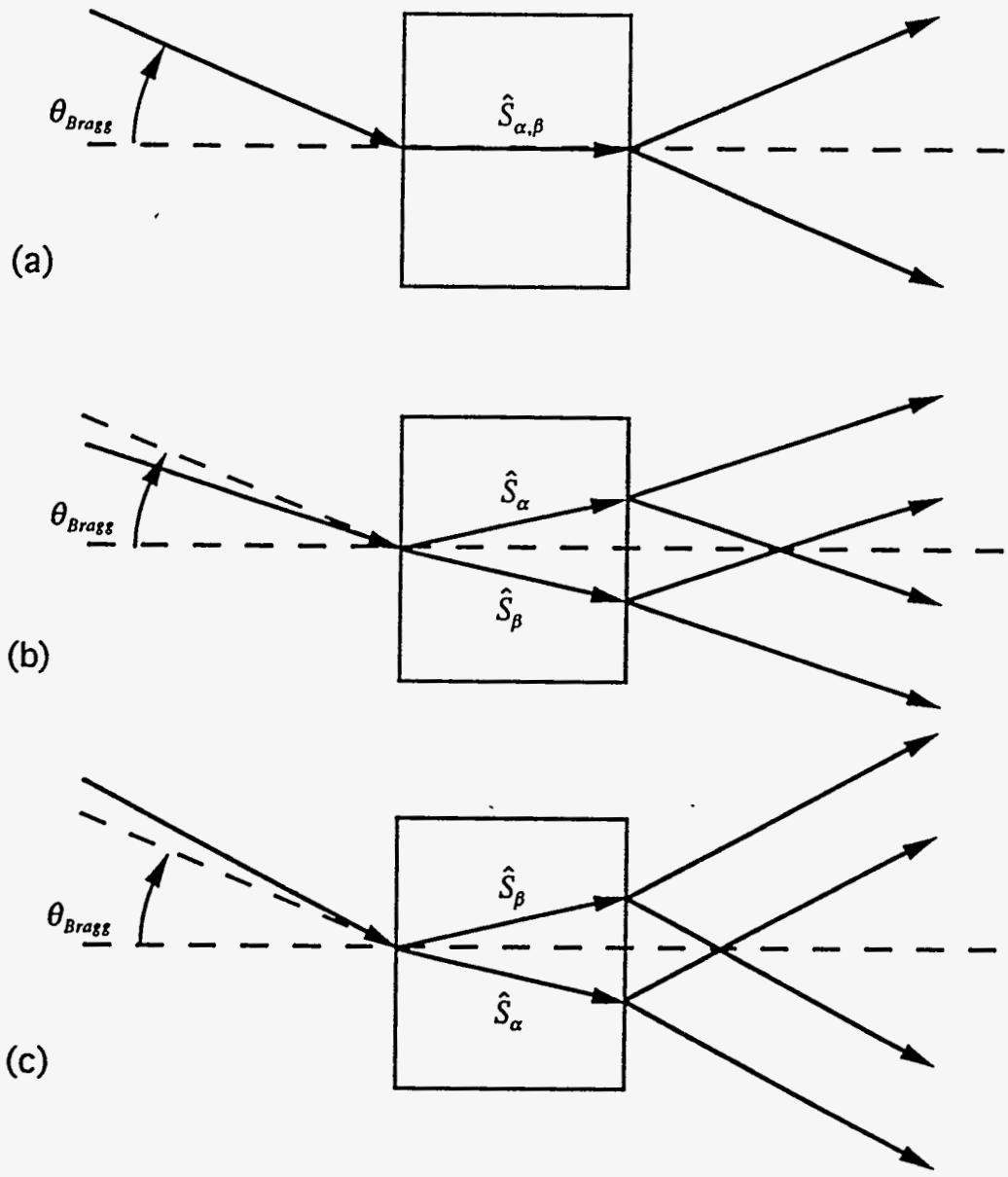

Fig. 4.9. (a) The Pointing vector in the case of a symetric Laue transmission lies along of the Bragg planes. (b) If the angle of incidence is slightly offset from the Bragg angle then the Pointing vectors of the α and β branch diverge thus causing an α and a β beam as shown. (c) An offset of the angle of incidence in the opposite direction causes an exchange of the α and β branch beams.

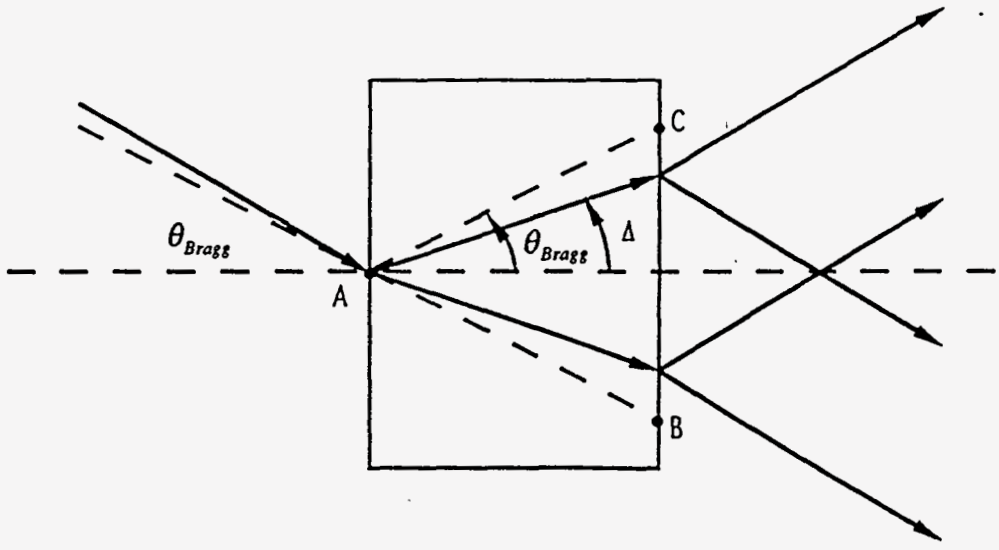

Fig. 4.10. The propagation angle Δ is limited to the range $\pm\theta_B$. This defines a triangle drawn through points A, B and C and is called the *Borrmann Triangle.*

faced wafer with primary diffraction planes perpendicular to the surface will result in the excitation of only two points on the dispersion surface. These two points will be at the diameter point of the dispersion of the $\alpha\sigma$ and the $\beta\sigma$ branches. The wavefield in the crystal will be defined by equation (4-50) where the amplitude ratio R of equation 4-51 will be either 1 or -1 for the α and the β mode respectively. The time averaged intensity of the α and the β constituents of the wave field can be written

$$I(\vec{r}) = \left|\vec{D}_o\right|^2 \left[2 \pm 2\cos\left(-2\pi\vec{H}_h \cdot \vec{r}\right)\right] \tag{4-60}$$

where the -(+) is for the $\alpha(\beta)$ mode. In the case of a strong reflection where all the atoms scatter in phase (such as the Si (220) reflection) the photoelectric

wavefield that has its maximum intensity at the atomic plane positions, will suffer a greater degree of photoelectric absorption (Fig. 4.11). In the case of a strong reflection where all the atoms scatter in phase (such as the Si (220) reflection) the β-branch waves will be strongly absorbed, while the waves of the α-branch will travel through the crystal suffering little absorption. If we consider a crystal thickness of ten absorption lengths (assuming the isotropic absorption coefficient for the sample) when rotated away from the Bragg condition, the kinematical theory and the single wave approximation predict an attenuation of the transmitted beam of exp(–10). Consequently one would not observe any transmitted intensity in the forward direction or the Laue reflected direction. When the crystal is brought into the Bragg condition, then the waves of the β-branch are eliminated but the waves of the α-branch pass through the crystal allowing the Laue reflected and the forward transmitted beam to be detected. This effect is called *anomalous transmission* or the *Borrmann Effect* (Fig. 4.12).

As was previously explained, the direction of propogation $\bar{S}$ of the waves inside the crystal is perpendicular to the dispersion surface at the tie point. In the case of the symmetric Laue reflection, this implies the wave propogates along the atomic diffraction planes. If one is carefull, it is possible to observe the offset of the transmitted beam (which is actually forward scattered). If the primary reflection does not have a large structure factor, this corresponds to having atoms between the scattering planes. Consequently absorption of the α-branch reduces the amount of anomolous transmission. If the sample is not of sufficient perfection so as to promote a standing wave, then the anomolous transmission is eliminated.

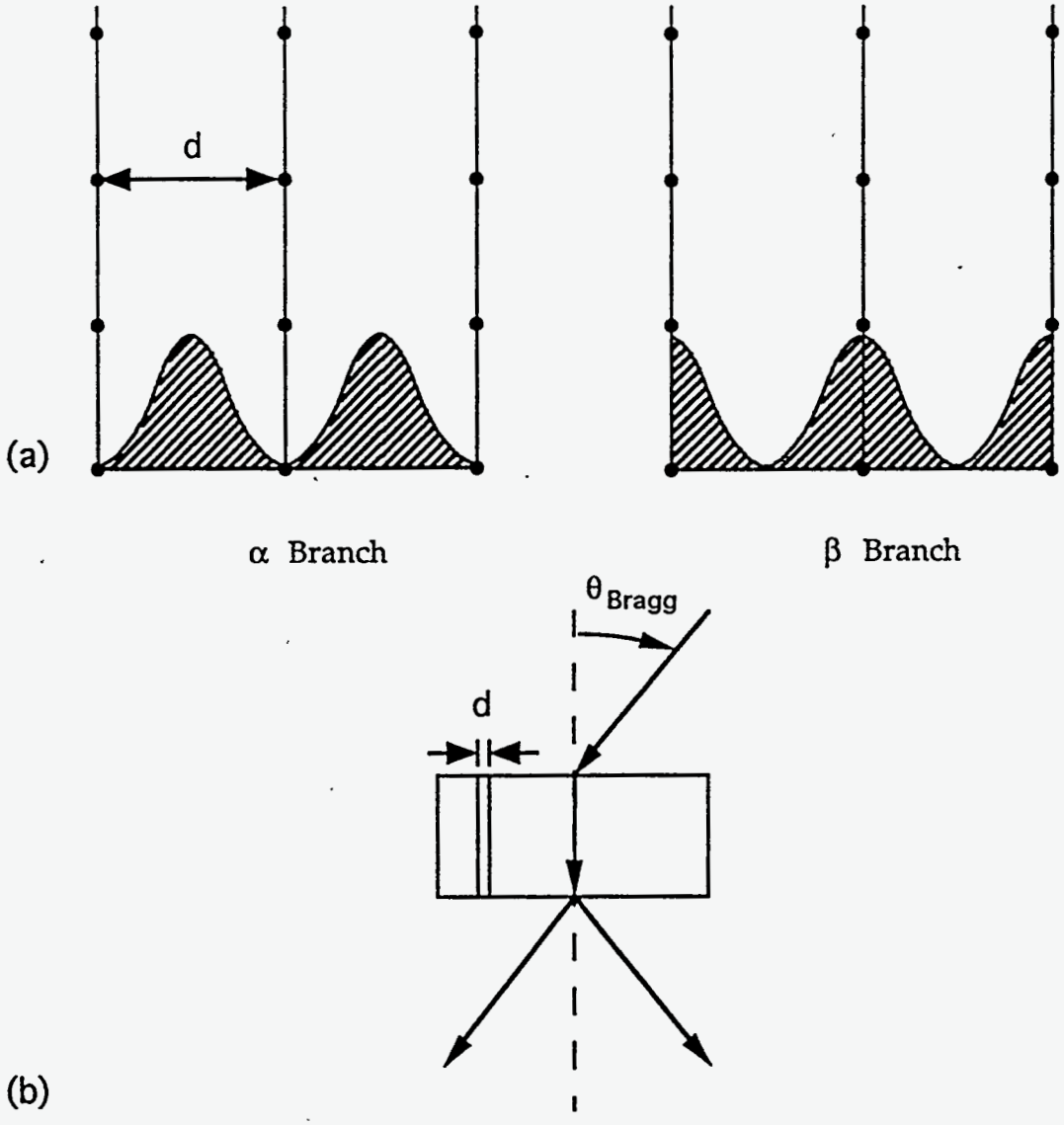

Fig. 4.11. The α and β components of the wavefield consist of waves with periods equivalent to the period of the Bragg planes that cause the reflection. The α and β modes are different by a 90° phase shift. In the case of Si (220), the wave of the α-branch has a minimum intensity at the atomic positions and suffers a relatively small amount of absorption while the β-branch is strongly absorbed. a) The a and the β wavefield. b) The corresponding scattering geometry.

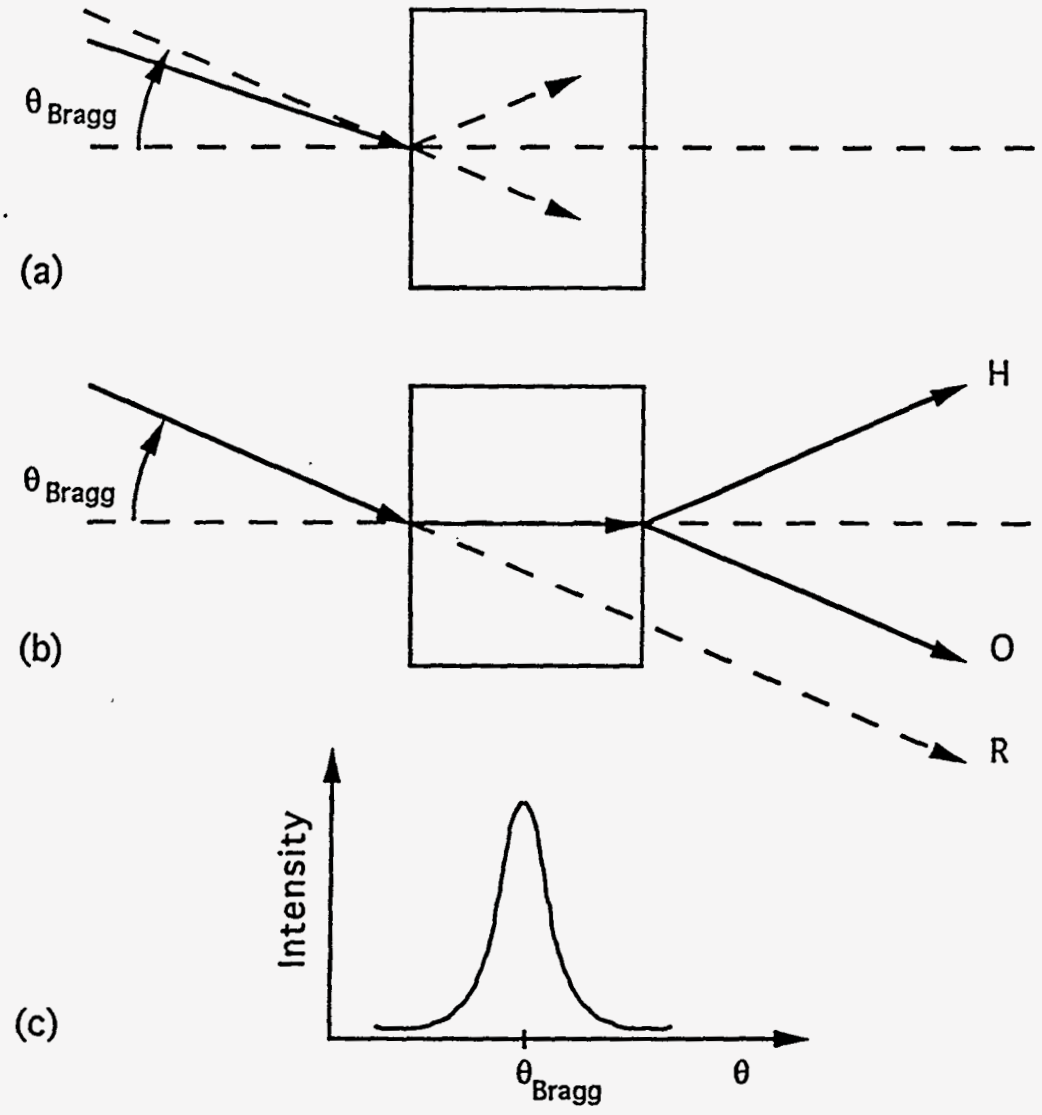

Fig. 4.12 a) In the thick crystal limit, when slightly misaligned from the Bragg condition, the transmitted beam is eliminated due to absorption. b) At the Bragg condition, a wavefield is promoted that allows a portion of the x-rays to pass through the sample suffering a smaller amount of absorption. The wavefield exits the sample at the back face and splits into the two components $\vec{D}_o$ and $\vec{D}_h$ propagating in the directions $\vec{k}_o$ and $\vec{k}_h$ respectively. These exiting beams are commonly labeled the *O* and the *H* beam. An undeflected beam is called a *Radiographic beam R* c) The intensity of the *O* beam as the crystal is rocked through the Bragg angle.

Spherical Waves, the Borrmann Fan, and Pendellösung Fringes

If the incident monochromatic x-ray beam exhibits a divergence that is larger than the rocking curve width of the reflection, then the beam is best represented by a spherical wave.[82-85] This results in the simultaneous excitation of the entire dispersion surface in the vicinity of the Laue Point, so that all the propagation angles Δ defined by the Borrmann Triangle will be produced. In other words, if the intensity of the x-rays at the back face of the crystal is measured, it will be found to be distributed over the distance B to C in Fig. 4.13a.

To describe the intensity distribution over the back face, one might first assume that the intensity will be maximum when $\Delta=0$ because this corresponds to x-rays that are incident at the exact Bragg angle. This is not the case, because of a subtle effect due to the variation of the divergence of the x-ray beam inside the crystal as opposed to the divergence of the incident beam. A relation between the incident divergence δ_{ext}, and the internal divergence δ_{int} can be written in terms of the Bragg angle θ_B, the wavevector $|\vec{k}_{ext}|$, the angle of incidence and the radius of curvature of the dispersion surface.

$$\frac{\delta_{ext}}{\delta_{int}} = \frac{|\vec{k}_{ext}|\cos\theta_B}{R\cos\theta} = A \qquad (4\text{-}61)$$

where A is defined as the angular amplification. It is evident that at the diameter point, the radius of curvature is smallest ($R<<|\vec{k}_o|$) therefore A is largest and the x-rays are spread out over a larger range of angles, Δ, while further from the diameter point, the dispersion surface asymptotically approaches the sphere of radius $|\vec{k}_o|$, so that the angular amplification approaches unity. For periodic crystals, values of the angular amplification on the order of 10^4 have been found

at the diameter point.[76] This effect causes the intensity to be distributed mostly toward the edges of the Borrmann Fan as shown in the Fig. 4.13. Since the intensity of the wavefield in the Borrmann triangle is composed of both α and β-modes that have different magnitudes, there will be constructive and distructive interference that modulates the Borrmann Fan intensity patterns (Fig. 4.13) These fringes are called Pendellösung fringes.

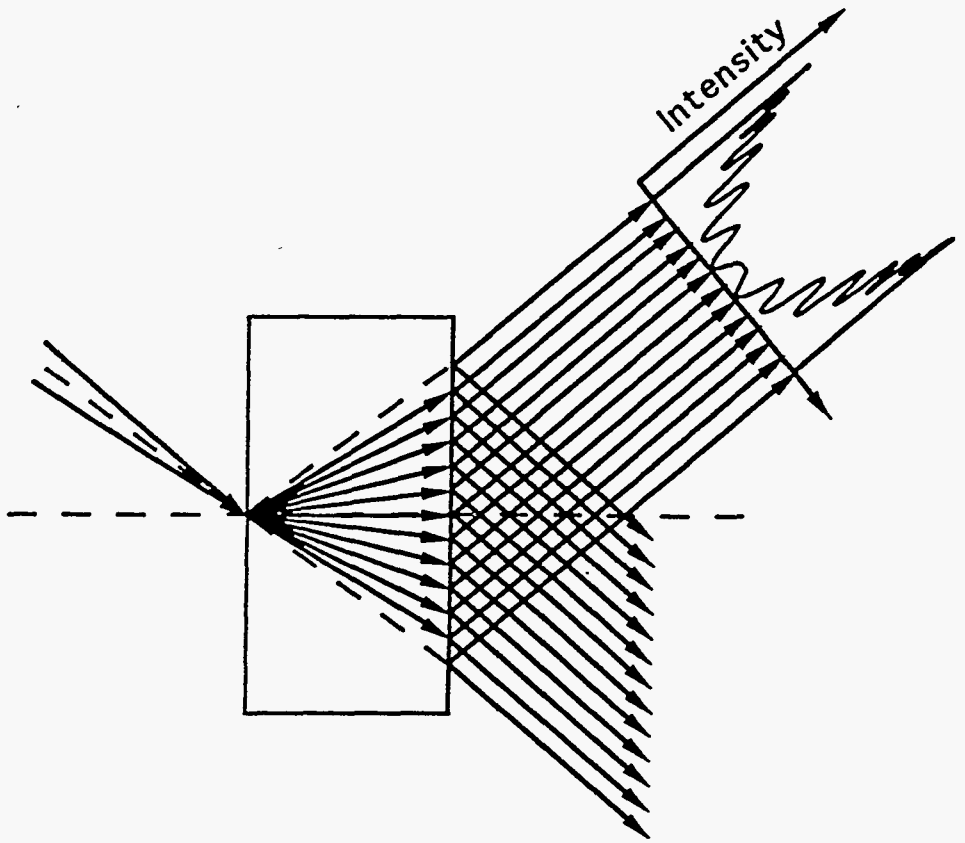

Fig. 4.13. The simultaneous excitation of the entire dispersion surface in the vicinity of the Laue Point results in a wave field composed of a range of propagation angles, Δ, defined by the Borrmann triangle. $\left(\theta_{Bragg} \geq \Delta \geq -\theta_{Bragg}\right)$. In the case of little absorption, the intensity is concentrated at the edges of the Borrmann Fan.

The Three Wave Case

The decription of the Borrmann Effect and Pendellosung pattern in the Borrmann Fan were described for the case of a two beam approximation. This resulted in the discription of the dispersion surface and the wavefield by equations (4-49) and (4-50).

It is instructive to consider the three wave case for a moment. Rather than dealing with a general three wave case, I will assume that the three waves lie on the same plane of reflection. This simplifies the problem while still allowing us to appreciate the additional complications that arise when attempting to describe the wave field in an n>2 approximation. In the case of three waves (4-29) can be written as:[73]

$$2e_o\vec{D}_o = \chi_o\vec{D}_{o[o]} + \chi_{\bar{h}}\vec{D}_{h[o]} + \chi_{\bar{p}}\vec{D}_{p[o]} \tag{4-62}$$

$$2e_h\vec{D}_h = \chi_h\vec{D}_{o[h]} + \chi_o\vec{D}_{h[h]} + \chi_{h-p}\vec{D}_{p[h]} \tag{4-63}$$

$$2e_p\vec{D}_p = \chi_p\vec{D}_{o[p]} + \chi_{p-h}\vec{D}_{h[p]} + \chi_o\vec{D}_{p[p]} \tag{4-64}$$

where O, H_h and H_p are three reciprocal lattice points lying simultaneously on the Ewald sphere. If we only concern ourselves with the σ-polarized electric field components, the vector equations simplify to three scalar equations.

$$(\chi_o - 2e_o)D_o + \chi_{\bar{h}}D_h + \chi_{\bar{p}}D_p = 0 \tag{4-65}$$

$$\chi_h D_o + (\chi_o - 2e_h)D_h + \chi_{h-p}D_p = 0 \tag{4-66}$$

$$\chi_p D_o + \chi_{p-h}D_h + (\chi_o - 2e_p)D_p = 0 \tag{4-67}$$

This produces the solutions:

$$D_h = D_o\left(\frac{\chi_p\chi_{h-p} - \chi_h(\chi_o - 2e_p)}{(\chi_o - 2e_h)(\chi_o - 2e_p) - |\chi_{h-p}|^2}\right) \tag{4-68}$$

$$D_p = D_o\left(\frac{\chi_h\chi_{p-h} - \chi_p(\chi_o - 2e_h)}{(\chi_o - 2e_h)(\chi_o - 2e_p) - |\chi_{h-p}|^2}\right) \tag{4-69}$$

This solution reveals an interesting result. One can immediately see that even if a certain term of the polarizability, let's say χ_p, is zero (i.e.. the structure factor F_p is zero) but the reciprocal lattice vector $\vec{R}_p$, is near the Ewald sphere, it is incorrect to simply assume a two wave approximation. The amplitude D_p, is non zero if neither χ_p nor χ_{p-h} is zero.

Dynamical Diffraction and Quasicrystals

The presence of multiple scattering of the x-rays is the significant factorin determining whether a crystal scatters kinematically or dynamically. This condition is described and discussed in B. E. Warren's text "X-Ray Diffraction"[86] and basically requires that the effective mean free path of the x-ray be smaller than the absorption length ($1/\mu$). In addition, the coherent volume of the structure must be large enough as well (the mean free path of the x-ray must be smaller than the correlation length of the crystal). This implies that for strong reflections, the quasicrystal, (or any crystal) may scatter dynamically while for weak reflections we are in the kinematical limit. The question can be raised, "how does the dynamical theory need to be modified to describe dynamical diffraction in a quasiperiodic structure?" and "is it possible to observe the Borrmann effect and Pendellosung fringe patterns in a non-periodic structure?" The answer is that the theory does not have to be modified (other than the use of

a structure factor per unit volume rather than structure factor per unit cell) if the two beam approximation holds. In the case of the Borrmann Effect, the promotion of the standing wave with period equal to the d-spacing of the primary diffraction planes only requires a reciprocal lattice point H_p. The existence of anomalous transmission of x-rays requires that a majority of the absorbing atoms be distributed approximately at the atomic planes of spacing (2π/H). This is another way of requiring the structure factor for the primary reflection to be large, the same condition imposed on periodic crystals.

The question, then, is whether the two beam approximation is valid for a quasicrystal, which is an incommensurate structure, with an infinite number of diffraction peaks near the Ewald sphere. Although most of the reflections are of infinitesimal structure factor, the question can be raised, can an infinite number of infinitesimal peaks near the sphere of reflection invalidate the two beam approximation for quasicrystals? It can be argued that the effect of a weak reflection near the Ewald sphere cannot be ignored by the example of the previous section discussing the three beam case. But if one takes into account the condition for dynamical diffraction, the weak reflections are not strong enough to scatter dynamically. If the coupling reflections H_{h-p} is also not strong enough to scatter dynamically, then the weak reflections can be ignored in the dynamical equation and the wavefield. This implies that when describing the dynamical diffraction from quasicrystals, there will be no dynamical effects from weak reflections H_p if there is only a very weak coupling reflection H_{h-p}.

The final constraint is ultimately, whether it is possible to grow a quasicrystal that has strong enough structure factors and is perfect enough to require the dynamical theory.

Besides proving some indication that the two beam approximation is valid, the Borrmann Effect and Pendellosung fringe pattern have proved to be sensitive probes for measuring the temperature effects on the structure factor (in the form of the Debye-Waller factor)[83] and the structure factor in absolute units. Dynamical x-ray diffraction offers a range of scattering techniques as probes of crystalline structures, for example standing wave experiments, allows us to develop x-ray polarizers and understand beam optics required for practically any high resolution experiment.

The observation of the Borrmann Fan and Pendellosung fringe patterns is directly related to the shape of the dispersion surface and is dependent on the existence of both the α and the β waves propagating simultaneously. Therefore the Pendellosung pattern is direct evidence of the dynamical theory.

V. DYNAMICAL X-RAY DIFFRACTION EXPERIMENTS

Introduction

The coherent x-ray scatttering measurements, presented in chapter 3, show that icosahedral Al-Pd-Mn is characterized by true long-range positional order over a length scale of at least 6 μm. These results suggest that this alloy might be of sufficient perfection for the observation of dynamical x-ray diffraction. As pointed out in the previous chapter, the absence of periodicity itself should not preclude or obscure dynamical diffraction effects, although the effects of multiple scattering from an "infinite" set of Bragg points may have some impact upon quantitative measurements. Indeed, the anomalous transmission of x-rays through an incommensurate or aperiodic crystal has been treated theoretically in some detail by Berenson and Birman for the special case of a one-dimensional Fibonacci lattice.[85] They concluded that while the effect is weaker in aperiodic systems, since full reflections are not found, it should still be observable. However, until the present measurements there existed no direct experimental evidence of dynamical x-ray scattering in quasicrystals or, indeed, other incommensurate systems. In the previous chapter, the origin of the Borrmann effect and Pendellösung fringe patterns were described. The observation of either phenomena is undisputable evidence of dynamical x-ray diffraction. In this chapter, results from two sets of experiments carried out on carefully prepared samples of icosahedral Al-Pd-Mn will be described.

Measurement of the Borrmann Effect

The Borrmann Effect (as described in the previous chapter) is best observed in the case of a symmetric transmitted Laue reflection of monochromatic x-rays. The sample is prepared in the form of a parallel faced wafer with the scattering planes perpendicular to the surface of the sample. The measurement consists of detecting x-rays transmitted through the sample as the sample is rocked through the Bragg angle for the strong reflection. One of the beautiful aspects of the measurement is that data analysis is quite simple (at least for the qualitative aspects of the experiment). The observation of a forward diffracted O-beam at the Bragg angle provides direct evidence of anomalous transmission and consequently dynamical diffraction.

The experiment was performed on a 0.4 mm thick parallel faced wafer of a single grain of the icosahedral Al-Pd-Mn alloy cut with twofold axes parallel and perpendicular to the smallest dimension (Fig. 5.1). The experiment was performed on beamline X23A3 at the National Synchrotron Light Source using 12 keV x-rays from a silicon double-crystal asymetric-cut monochromator set at the (111) reflection. At this energy, the 0.4 mm thick sample presents approximately 10 absorption lengths to the incident beam so that its transmission through the sample is essentially eliminated. In the terminology of dynamical diffraction, we are in the "thick crystal limit." The asymmetric monochromator was chosen in order to magnify the vertical dimension of the beam and, at the same time, reduce the angular divergence of the x-rays to produce a collimated monochromatic beam with a uniform intensity over a large cross sectional area. Although these beam

characteristics were not required for the Borrmann effect measurement itself, they were necessaary for x-ray topographic measurements performed at the same time. For the anomolous transmission measurements, the dimensions of the beam were reduced to 3 mm in the horizonatal and 1 mm in the vertical direction in order to reduce spill over of x-rays around the sample.

The experiment is shown schematically in Fig. 5.1. The x-ray beam is incident from the left and strikes the sample at the correct Bragg angle for diffraction from the (h/h' k/k' l/l')=(2/4 0/0 0/0) reflection along the twofold axis (using the indexing scheme discribed in Chapter 1). This reflection is one of the strongest found in Al-Pd-Mn, and therefore is the most likely candidate reflection for the observation of dynamical effects. At the Bragg condition, two emerging beams were recorded on Polariod film placed 3.5 cm behind the sample (right side of Fig. 5.1). The H beam is the diffracted Laue beam found at an angle of $2\theta_{Bragg}$ from the incident beam direction. The O beam is the anomalously transmitted (forward diffracted) beam parallel to, but displaced laterally from, the incident beam direction. As the sample was rotated by 0.04° away from the correct Bragg angle, no intensity at these positions was observed. Nevertheless, the observation of the O beam, at the Bragg angle, is clear evidence of dynamical diffraction from the sample.

The intensity profile of the O beam was recorded by replacing the film with a NaI scintillation detector and aperture to isolate the O beam from the H beam and other background radiation. Fig. 5.2 shows the intensity in the forward scattering direction as the crystal angle is scanned through the diffraction condition, again clearly showing the phenomenon of anomalous transmission. The measured angular width of the forward diffracted beam, 0.006° FWHM, results from the convolution of the incident beam profile and the rocking curve width of the

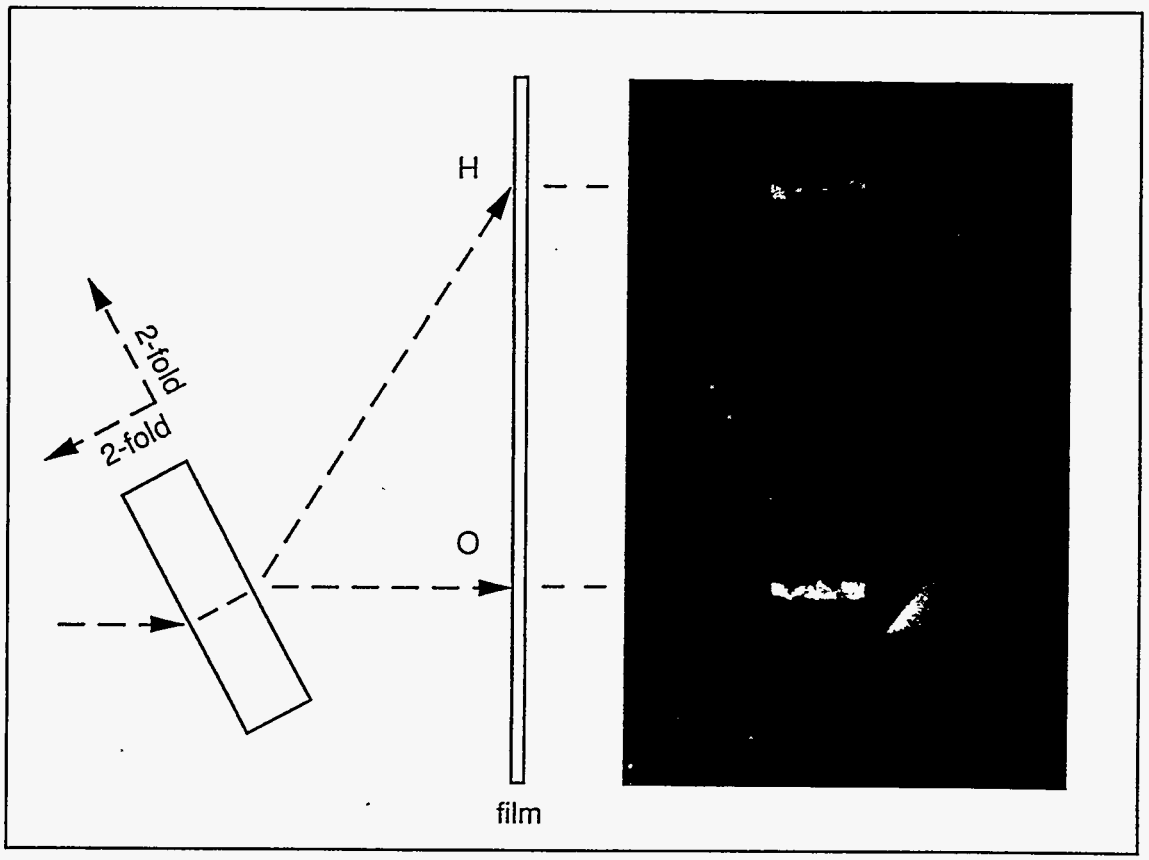

Fig. 5.1. Schematic (left) and results (right) of the Borrmann effect measurement. The sample surfaces are represented by the rectangle and the crystallographic orientation is illustrated directly above the sample. The dashed arrows passing through the sample depict the paths traced by the incident beam as well as the three exiting beams. The right side of the figure is an enlargement of a photograph taken down-stream of the sample in the Bragg condition. The H, O, and the R beams of the schematic have been drawn to correspond to the analogous images. When the sample is rotated about an axis perpendicular to the scattering plane, the H- and the O-beam disappear and the R-beam is left as a single stripe of weak intensity.

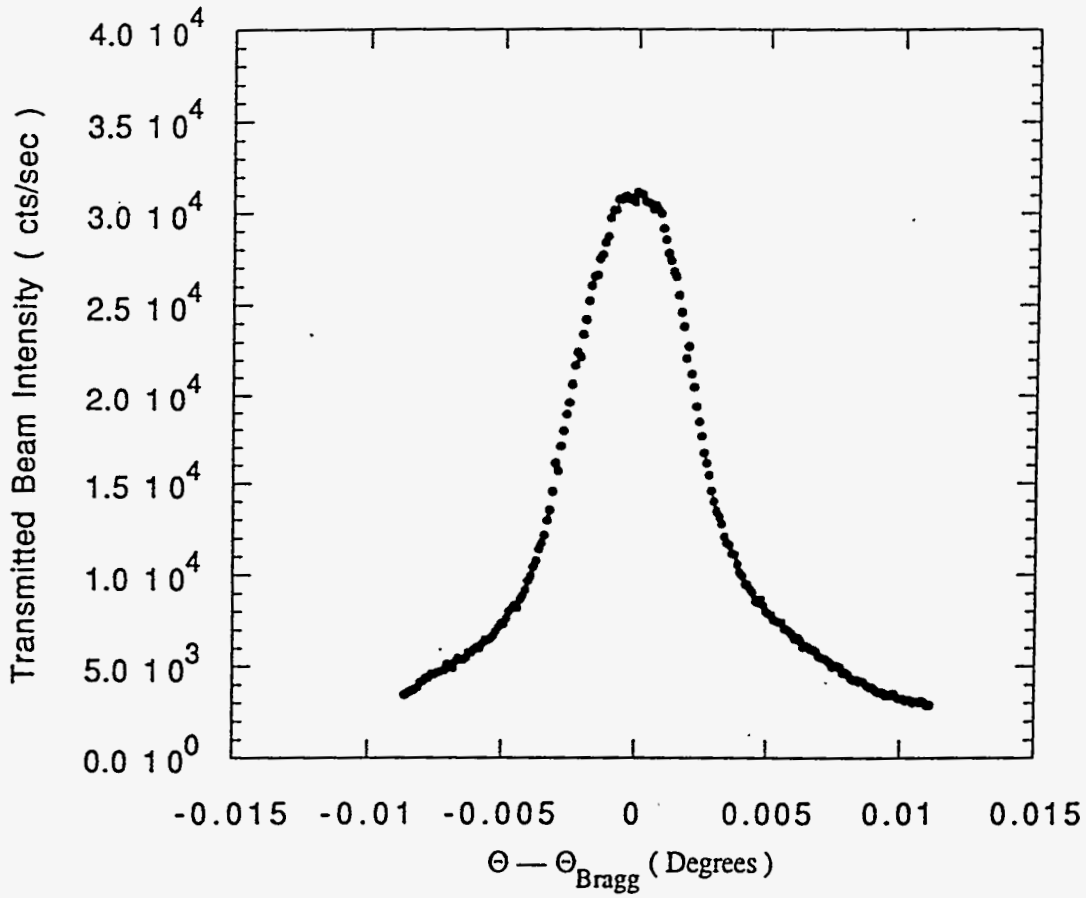

Fig. 5.2. Intensity of the forward diffracted beam (O beam) as the sample is rotated through the diffraction condition. The nominal zero of the horizontal scale was chosen at the center of the angular range of the reflection.

quasicrystal. The divergence of the incident monochromatic beam was limited to 0.004° by a 1.0 mm vertical slit before the sample. Therefore, from this measurement a reasonable upper limit on the intrinsic rocking curve of the (2/4 0/0 0/0) reflection is 0.004°, comparable to the rocking curve width of the (111) reflection of silicon of approximately 0.002°.

The sample, as might be expected, is not perfect across the entire 3 mm by 1 mm extent of the beam. There is structure in both the O and H beams related to the existence of defects in the quasicrystal. Figure 5.3 shows a magnified view of the O and H beams, revealing the presence of macroscopic voids (black spots) and scratches on the surfaces (both front and back) of the sample. The contrast in these images arises from the strain field surrounding the defect that distorts the lattice over a region, generally, much larger than the defect itself.

The study of defects in crystals through this technique, x-ray topography, is a mature field of study[76]. In the present study, we have used this technique to evaluate the size and location of regions of the sample that were relatively free of defects. For x-ray topographic measurements at synchrotron sources, exposures must be taken with relatively short exposures to observe fine details. To accomplish this, the incident x-ray energy was increased to 20 keV, decreasing the effective absorption length of the sample. The diffraction geometry remained the same as for the Borrmann effect measurements, but the slits upstream of the sample were opened to make full use of the large spatial extent of the beam. Typical exposure times were on the order of five minutes.

Figure 5.4 shows a transmission Laue topograph (the H beam) taken when the sample was rotated into the "correct position" for the (2/4 0/0 0/0) reflection. Here, the dark regions correspond to the portions of the sample which diffract, while the light regions correspond to portions out of the Bragg condition. If the sample is rotated by a small angle (on the order of the rocking curve width), away from this position, the contrast changes (see, for example, Fig. 2.5). These large scale variations in contrast are not unusual in metallic crystals (even so-called perfect ones) and can arise from the presence of elastic strain or compositional variations in

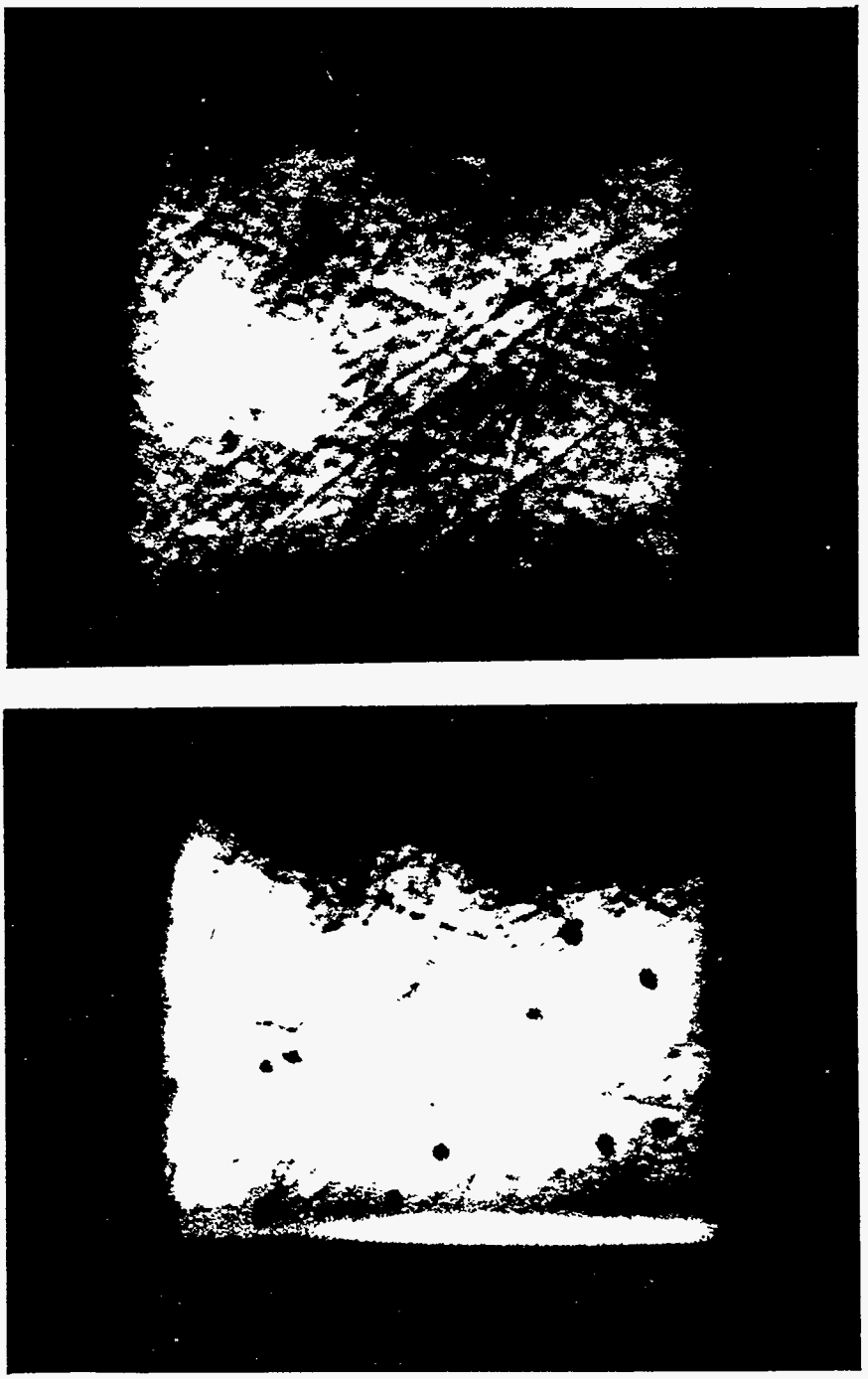

Fig. 5.3. A magnified view of the O and H beams of Fig. 5.2, revealing the presence of macroscopic voids (black spots) and scratches on the surfaces (both front and back) of the sample.

the sample. Figure 5.4 also exhibits some very fine-scaled variations in contrast which arise, most likely, from dislocations in the structure.

The Borrmann Fan - Pedellösung Fringe Experiment

The observation of anomalous transmission, descibed above, implies the existence of dynamical scattering and the promotion of a wavefield inside the sample. However, In order to obtain even more direct evidence of the existence of a dispersion surface, it is necessary to resolve the Borrmann Fan (as described in the previous chapter) from the transmission of x-rays through a thin parallel faced sample. The Borrmann fan is modulated by Pendellösung fringes which are due to the interference of the two modes (α and β) propagating through the structure.

The Borrmann Fan experiment is similar to the anomalous transmission experiment in that the sample is prepared in the form of a parallel faced wafer and oriented with respect to the x-ray beam so as to satisfy the condition for a symmetric transmission Laue reflection. The Borrmann Fan experiment differs from the anomalous transmission experiment in the use of a thin crystal and a divergent beam to illuminate entire dispersion surface simultaneously as described in Chapter 4.

These experiments were done at the Cornell High Energy Synchrotron Source (CHESS) beam line B2 using a double crystal, asymmetric cut Ge(220) monochromator. The asymmetric cut crystals were now used to demagnify the beam in an attempt to increase the angular divergence of the incident beam so that it was larger than the rocking curve width of the quasicrystal. Again, the crystal was set in the symmetric Laue geometry, diffracting from the (2/4 0/0 0/0) reflection. In order to observe the interference of the α and β modes of the wavefield, it is

Fig. 5.4. A transmission topograph of the (2/4 0/0 0/0) twofold reflection (two fold planes perpendicular to the surface) from a parallel faced sample (0.4mm thick) with fivefold planes parallel to the surface.

necessary that absorption does not eliminate the β mode. For this reason x-rays in the energy range above 20 keV were used, for a 0.4 mm thick (μt~2) sample.

The expected Pendellosung pattern can be calculated from the known thickness of the sample, the Bragg angle of the reflection, the absorption coefficient, and an estimate of the structure factor of the reflection.[85,86] In Fig. 5.5 I show calculated Pendellösung patterns for the (2/4 0/0 0/0) reflection at a series of three energies using a structure factor determined in measurements by deBoissieu et al.[87] The Bragg angle of the reflection at 20.5 keV incident energy is θ_{Bragg}=8.483°. The width of the pattern, for an incident beam of infinitessimal width, should then be $L=2t\sin(\theta_{Bragg})$=118 μm. Under these conditions, about 14 fringes from one edge of the fan to the other should be observed, with an average fringe width of approximately 8.5 μm.

The experimental geometry used in this measurement is shown in Fig. 5.6. The incident beam was first passed through an aperture in order to create a spacially defined beam and the sample was oriented in order to satisfy the Bragg condition for the (2/4 0/0 0/0) transmission Laue reflection. The key to a succesful measurement of the Borrmann Fan and the Pendellösung pattern is to limit the size of the incident beam to avoid smearing the Pendellösung pattern and obscuring the fringes. In order to obtain a beam size at the sample of 5 μm (smaller than the average fringe spacing), we constructed apertures by aligning two polished tungsten cylindrical rods with a 0.003" gap between them. Although the gap was too large for the required resolution, the gap between the rods could be centered on the beam. The rods were then rotated to reduce the effective width of the aperture. The slits were mounted on translation and rotation stages that allowed alignment and adjustment of the apertures. The spacial distribution of intensity at the back face of the sample

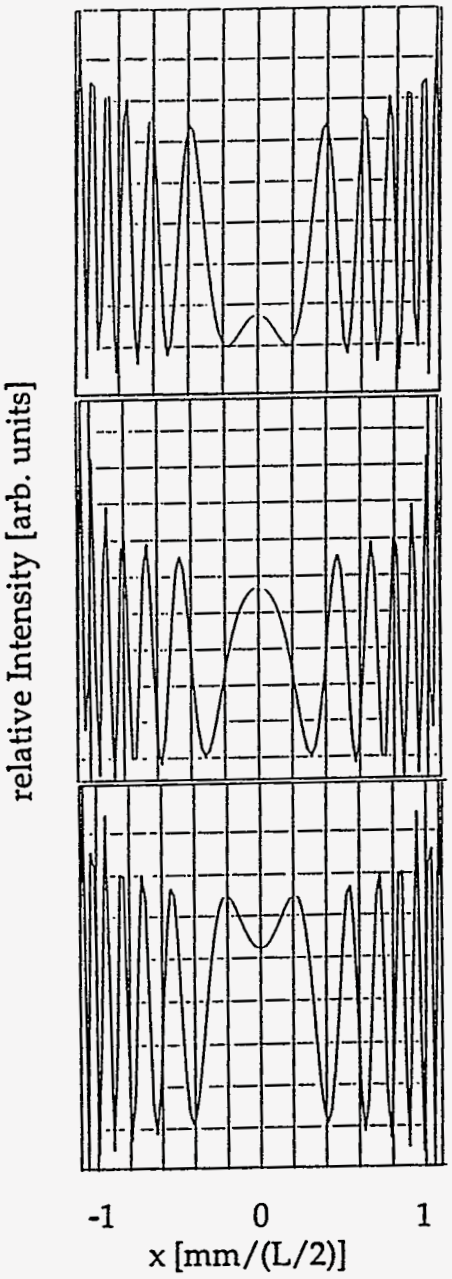

Fig. 5.5. Calculated Pendellösung patterns for the (2/4 0/0 0/0) reflection at energies of a) 21.5 keV, b) 21 keV, and c) 20.5 keV. The horizontal axis represents the transverse position, X, across the reflected beam in units normalized to the half width of the reflected beam (L/2).

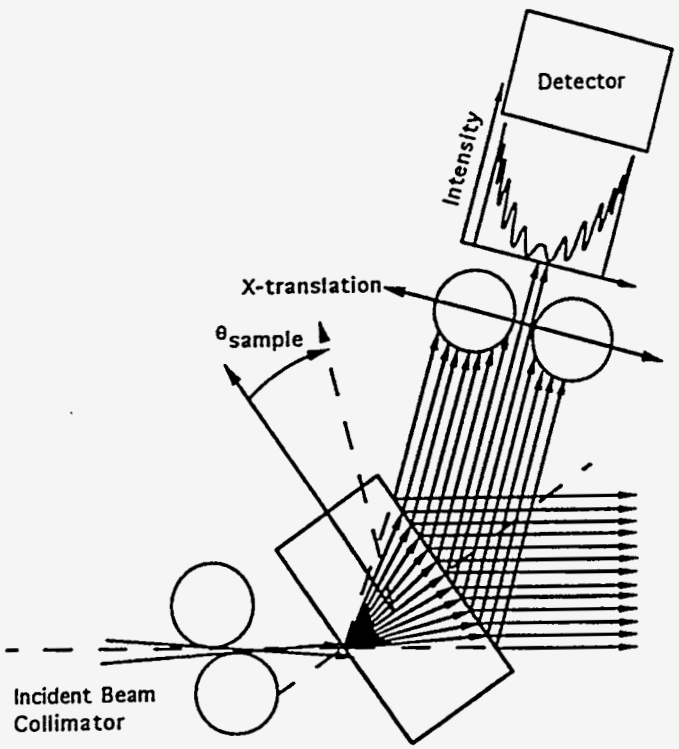

Fig. 5.6. The experimental geometry used for the Pendellösung measurements.

was measured by scanning a second aperture across the diffracted beam in steps of 2.5 μm, over a range of approximately 240 μm.

Data were taken at several energies around 20 keV, and as a function of angle measured relative to the center of the rocking curve of the sample. The data taken at 20.5 keV incident energy, shown in Fig. 5.7, clearly show the existence of the Borrmann Fan of the expected width and approximate shape. In particular, the distinctive peaks in intensity at the edges of the fan are found. This observation again confirms that the Al-Pd-Mn quasicrystals is scattering dynamically. There is also evidence of the Pendellösung interference pattern in these scans, although it appears distorted and smeared. While unfortunate, this is not surprising since the

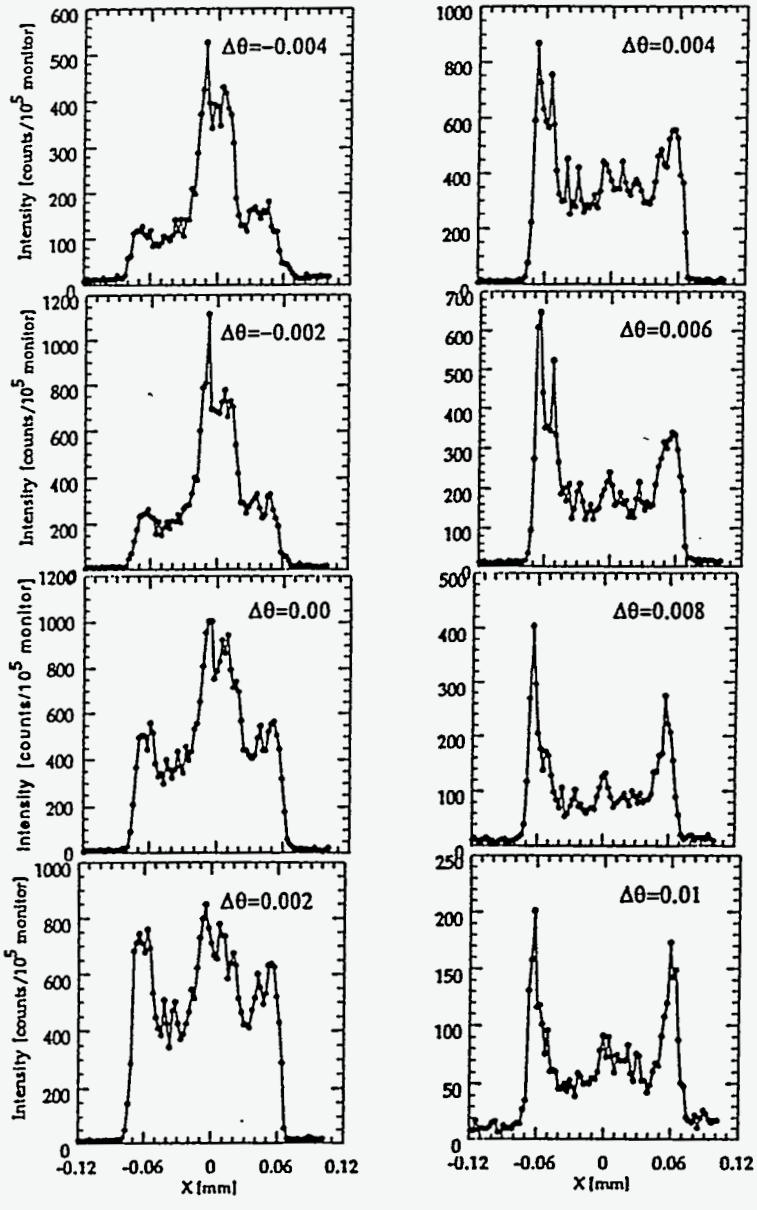

Fig. 5.7. The intensity distribution of the reflected 20.5 keV x-rays from the (2/4 0/0 0/0) reflection of Al-Pd-Mn at varied values $\Delta\theta$ (the deviation of the incident beam direction away from the Bragg condition). The patterns clearly show the existence of the Borrmann Fan of the expected width. Furthermore, the shape of the pattern (particularly the intensity at the center) is very sensitive to $\Delta\theta$.

Pendellösung pattern is extremely sensitive to strain and the quality of the sample surface.[76]

Two features of Figure 5.7 warrant further discussion. In the ideal experiment, where the incident beam divergence is *much* greater than the rocking curve of the reflection, the entire dispersion surface is excited. The Pendellösung pattern should then be symmetric and relatively insensitive to small deviations from the exact Bragg angle. In Figure 5.7, however, we see a pronounced asymmetry in the intensity at the margins of the pattern that changes from one side of the Bragg angle to the other. Furthermore, we see that the shape of the pattern (particularly the intensity at the center) is very sensitive to the deviation of the incident beam direction away from the Bragg condition. One possible explanation for the presence of this central peak is that a portion of the sample is scattering kinematically rather than dynamically. Scattering from these portions of the sample would contribute to the central region of the pattern, but not the wings. Alternatively, both the asymmetry of the pattern and the presence of the central peak indicate that the incident beam divergence was not large enough to excite the entire dispersion surface simultaneously.

In the following discussion it will be useful to refer back to Fig. 4.9 and Fig. 4.13. If the incident beam does not excite all points on the dispersion surface, then at $\Delta\theta=0$ (in Fig. 5.7), the intensity at the center of the Borrmann Fan will be a maximum with lower intensity in the wings, while as $\Delta\theta$ increases, the intensity in the wings will grow at the expense of the central peak. Furthermore, the asymmetry in the intensity at the edges of the pattern can be attributed to the difference in absorption of the α and β modes of the wavefield. For uniform illumination of the dispersion surface, the α and β modes contribute equally to the intensity at both edges of the

pattern. If the incident beam divergence is only marginally larger than the rocking curve of the reflection, the β (α) mode will contribute more to the left(right) wing of the patterns in Fig. 5.7 for incident angles slightly lower than the nominal Bragg angle. Conversely, for incident angles slightly larger than the nominal Bragg angle, the situation is reversed. Since the absorption for the β mode is greater than that for the α mode, the asymmetry observed in Fig. 5.7 results.

Conclusion

The observation of dynamical diffraction from quasicrystals holds some important implications for structural investigations of these phases. First, we point out that primary extinction effects associated with diffraction from single grains of Al-Pd-Mn, and presumably many of the other FCI alloys, may be very significant and should be carefully corrected for prior to the use of diffraction data as input to structural determinations. Preliminary comparisons between diffracted beam intensities from roughly ground spheres of Al-Pd-Mn and the sample used in this present study confirm this point.[87] Second, we note that several probes based upon dynamical diffraction effects, such as x-ray standing wave fluorescence techniques, multiple beam interference effects and x-ray transmission topographs, may now be employed to study the bulk and surface structure of some quasicrystals. Indeed, efforts are already underway by some groups to use multiple diffraction interference effects to determine whether quasicrystalline systems are centrosymmetric[88]. More generally, the observation of dynamical diffraction from icosahedral Al-Pd-Mn is a striking confirmation of the fact that quasicrystals can present a degree of structural perfection comparable to that found in the best periodic intermetallic crystals.

REFERENCES

1 D. Shechtman, I. Blech, D. Gratias and J.W. Cahn, *Phys. Rev. Lett.*. **53,** 1951 (1984).

2 A. I. Goldman and K. F. Kelton, *Reviews of Modern Phys.* **65,** 213 (1993).

3 Kittel, C. Introduction to Solid State Physics, Ch. 1 (Wiley, New York, 1986).

4 H. S. Chen and A. Inoue, *Scr. Metall.* **22,** 727 (1987).

5 K. F. Kelton, P. C. Gibbons, and P. N. Sabes, *Phys. Rev.* **B 37,** 3940 (1988).

6 P. A. Bancel, P. A. Heiney, P. W. Stephens, A. I. Goldman, and P. M. Horn, *Phys. Rev. Lett.* **54,** 242 (1985).

7 P. M. DeWolf, *Acta Cryst.* **A28,** S111 (1972); *ibid.* **A30,** 777 (1974).

8 A. Janner and T. Janssen, *Phys. Rev.* **B15,** 643 (1977); *Physica* 99, 47 (1979);

9 J. F. Sadoc and R. Mosseri, *Phil. Mag.* **B45,** 467, (1982).

10 D. R. Nelson, *Phys. Rev. Lett.* **53,** 982, (1983).

11 N. G. de Bruijn, *Proc. K. Ned. Akad. Wet. A* **84,** 39 (1981).

12 P. Kramer and R. Neri, *Acta Crystallogr. A* **40,** 580 (1984).

13 P. Bak, *Phys. Rev. Lett.* **54,** 1517 (1985).

14 P. Bak, *Phys. Rev. B* **32,** 5764 (1985).

15 M. Duneau and A. Katz, *Phys. Rev. Lett.* **54,** 2688 (1985).

16 P. A. Kalugin A. Y. Kitaev, and L. S. Levitov, *JETP Lett.* **21,** 145 (1985).

17 V. Elser, *Phys. Rev. B* **32,** 4892 (1986).

18 R. Collela, *Acta Cryst.* **A30,** 413 (1974).

19 M.D. Ball and D.J. Lloyd, *Scr. Met.* **19,** 1065 (1985).

20 P. Sainford, B. DuBost, and A. Dubois, *C. R. Acad. Sci. Paris* **301,** 689 (1985).

21 A. P. Tsai, A. Inoue, and T. Masumoto, *Jpn. J. Appl. Phys.* **27,** L1587 (1988).

22 A. P. Tsai, A. Inoue, Y. Yokoyama and T. Masumoto, *Phil. Mag. Lett.* **61,** 9 (1990).

23 He, L. X, Li, X.Z., Zhang, Z., Kuo, K. H., *Phys. Rev. Lett.* **61,** 1116 (1988).

24 S. Amelinckx, C. Van Heurck, G. Van Tendeloo, Quasicrystals and Incommensurate Structures on Condensed Matter, edited by M. J. Yacaman, D. Romeu, V. Castano, and A. Gomez (World Scientific, Singapore), p. 300 (1990).

25 S. Hendricks and E. Teller, *J. Chem. Phys.* **10,** 147 (1942).

26 M. E. Huster, P. A. Heiney, V. B. Cajipe, and J. E. Fischer, *Phys. Rev. B* **35,** 3311 (1987).

27 D. C. Johnson and S. P. Frysinger, *Phys. Rev. B* **30,** 980 (1984).

28 L. Pauling, *Nature* **317,** 512 (1985).

29 L. Pauling, Phys. Rev. Lett. **58,** 265 (1987).

30 L. Pauling, Extended Icosahedral Structures, Ch. 4, Edited by M. V. Jaric and D. Gratias, (Academic Press Inc., New York, 1989).

31 A. L. Mackay, *Acta. Cryst.* **15,** 916 (1962).

32 V. Elser and C. L. Henley, *Phys. Rev. Lett.* **55,** 2883 (1985).

33 P. Guyot and M. Audier, *Phil. Mag. B* **52,** L15 (1985).

34 M. A. Marcus and V. Elser, *Phil. Mag. B* **54,** L101 (1986).

35 D. C. Koskenmaki, H. S. Chen, and K. V. Rao, *Phys. Rev. B* **33,** 5328 (1986).

36 K. K. Fung and Y. Q. Zhou, *Phil. Mag. B* **54,** L27 (1986).

37 M. Audier and P. Guyot, Extended Icosahedral Structures, Ch. 1, Edited by M. V. Jaric and D. Gratias, (Academic Press Inc., New York, 1989).

38 R. Penrose, *Bull. Inst. Math. Appl.* **10,** 266 (1974).

39 R. Penrose, *Mathematical Intelligencer* **2,** 32 (1979).

40 A. L. Makay, *Physica* **A114,** 609 (1982).

41 R. Ammann, (unpublished).

42 D. Levine and P. J. Steinhardt, *Phys. Rev. Lett.* **53,** 2477 (1984).

43 P. W. Stephens, and A. I. Goldman, Phys. Rev. Lett. **56,** 1168 (1986).; *Erratum ibid* **57,** 2331 (1986).

44 P. W. Stephens, Extended Icosahedral Structures, Ch. 2, Edited by M. V. Jaric and D. Gratias, (Academic Press Inc., New York, 1989).

45 C. A. Guryan, A. I. Goldman, P. W. Stephens, K. Hiraga, A. P. Tsai, A. Inoue, and T. Masumoto, *Phys. Rev. Lett.* **62,** 2409 (1989).

46 P. A. Bancel, *Phys. Rev. Lett.* **63,** 2741 (1989).

47 M. de Boissieu, et al., *Phil. Mag. Lett.* **65,** 147 (1992).

48 J. Devaud-Rzepski, A. Quivy, Y. Calvayrac, M. Cornier Quiquandon, D. Gratias, *Philos. Mag.* B **60,** 855 1989.

49 S. Ebalard, F. Spaepan, *J. Mater. Res.* **5,** 62 1990.

50 A. P. Tsai, A. Inoue, Y. Yokoyama and T. Masumoto, *Mat. Trans. JIM* **31,** 98 (1990).

51 Y. Yokoyama, A. P. Tsai, A. Inoue and T. Masumoto, *Mat. Trans. JIM* **32,** 1089 (1991).

52 Y. Yokoyama, T. Miura, A. P. Tsai, A. Inoue and T. Masumoto, *Mat. Trans., JIM* **33,** 97 (1992).

53 C. Beeli, H. U. Nissen and J. Robadey, *Phil. Mag. Lett.* **63,** 87 (1991).

54 M. de Boissieu, M. Durand-Charre, P. Bastie, A. Carabelli, M. Boudard, M. Bessière, S. Lefebvre, C. Janot and M. Audier, *Phil. Mag. Lett.* **65,** 147 (1992).

55 T. W. Ellis, T. A. Lograsso, S. Hilsenbeck and H. E. Sailsbury, *Metals and Materials Waste Reduction, Recovery and Remediation*, Edited by K. C. Liddell, R.G. Orth, (1994).

56 private communication with Roberto Collela.

57 S.-L. Chang, J. W. Anderegg and P. A. Thiel, (submitted to *J. Non-Crystalline Solids*).

58 {X. Wu, S. W. Kycia, C. G. Olson, P. J. Benning, A. I. Goldman, and D. W. Lynch }

59 M. de Boissieu, M. Boudard, B. Hennion, R. Bellissent, S. Kycia, A. Goldman, C. Janot, and M. Audier, submitted to (*Phys. Rev. Lett.)* (1995).

60 E. Haanappel, S. Kycia, F. Mueller, P. Canfield, and A. Goldman (to be submitted).

61 M. Sutton, S. G. J. Mochrie, T. Greytak, S. E. Nagler, L.E. Berman, G. A. Held, and G. B. Stephenson, *Nature* **352**, 608 (1991).

62a A. Garg and D. Levine, *Phys. Rev. Lett.* **60**, 2160 (1988).

62b L. Robertson and S. C. Moss, *Phys. Rev. Lett.* **66**, 353 (1991).

63 M. Born, E. Wolf, *Principles of Optics* 396; 508-511 (Pergamon, Oxford, 1975).

64 P.P. Ewald, *Fifty years of x-ray diffraction* 204-206 edited by P.P. Ewald, (N. V. A. Oosthoek's Uitgeversmaatschappij Utrecht, The Netherlands 1962).

65 B. D. Cullity, *Elements of x-ray diffraction 2nd ed.* 383-385 (Addison-Wesley Publishing Compony, inc., Massachusetts 1978).

66 B. E. Warren, X-Ray Diffraction 216 (Dover Publications, Inc., New York 1990).

67 P. N. Pusey, *In Photon Correlation Spectroscopy and Velocimetry* (eds H. Z. Cummins & E. R. Pike) 45-141 (Plenum, New York, 1977).

68 E. Jakeman, P. N. Pusey, and J. M. Vaughan, *Opt. Commun.* **17,** 305-308 (1976).

70 M. Renninger, *Zs. f. Krist.* **A 99,** 368 (1934).

71 R. Bubakova, J. Drahokoupil, A. Fingerland, *Czech. J. Phys.* **B 12,** 764 (1962).

72 R. W. James, *The Optical Principle of the Diffraction of X-Rays* (Bell, London 1950).

73 P. P. Ewald editor, *Fifty Years of X-Ray Diffraction,* (N. V. A. Oosthock's Nitgevers Mij, Utrecht 1962).

74 Z. G. Pinsker, *Dynamical Scattering of X-Rays in Crystals,* (Springer-Verlag, Berlin 1978).

75 S-L Chang, *Multiple Diffraction of X-Rays in Crystals,* (Springer-Verlag, Berlin 1984).

76 B. K. Tanner, *X-Ray Diffraction Topography,* (Pergamon Press, Oxford, 1976).

77 W. H. Zachariasen, *Theory of X-Ray Diffraction in Crystals,* (J. Wiley and Sons, Inc., New York 1945).

78 B. W. Batterman, and H. Cole, *Rev. Mod. Phys.* **36,** 681 (1964).

79 M. von Laue, *Acta Crystal.* **2,** 106 (1949).

80 G. Brogren and O. Adell, *Arkiv Fys.* **8,** 97 (1954).

81 A. Authier, *Bull. Soc. Fran. de Minér. et Cristal.* **84,** 51 (1961).

82 N. Kato, *Acta Cryst.* **14,** 526, (1961).

83 N. Kato, *Acta Cryst.* **14,** 627 (1961).

84 N. Kato, *J. Phys. Soc. Japan* **21,** 1160 (1966).

85 N. Kato, *Acta Cryst.* **A25,** 115, (1969).

82 B. E. Warren, *X-Ray Diffraction,* 331 (Dove Publishing, Inc., Oxford 1990).

83 A. Merlini and S. Pace, *Il Nuovo Cimento* **25,** 377 (1965).

84 R. Berenson and J. L. Birman, *Phys. Rev. B* **34,** 8926 (1986).

85 N. Kato, *J. Appl. Phys.* **39**, 2225 (1968).

86 N. Kato, *J. Appl. Phys.* **39**, 2231 (1968).

87 M. de Boissieu, M. Durand-Charre, P. Bastie, A. Carabelli, M. Boudard, M. Bessière, S. Lefebvre, C. Janot and M. Audier, *Phil. Mag. Lett.* **65**, 147 (1992).

88 H. Lee, R. Colella, and L. D. Chapman (unpublished)